

**NUMERICAL ANALYSIS AND EXPERIMENTAL
INVESTIGATION OF ULTRA-HIGH-PERFORMANCE
CONCRETE HYBRID BRIDGE DECK CONNECTIONS**

A Dissertation

Presented in Partial Fulfillment of the Requirements for the
Degree of Doctor of Philosophy

with a

Major in Civil Engineering

in the

College of Engineering

University of Idaho

by

Sabreena Nasrin

Major Professor: Ahmed Ibrahim, Ph.D. PE

Committee Members: Richard J. Nielsen, Ph.D., PE; S. J. Jung, Ph.D., PE,

Gabriel Potirniche, Ph.D., PE

Department Chair: Patricia J. S. Colberg, Ph.D., PE

December 2019

Authorization to Submit Dissertation

This dissertation of Sabreena Nasrin, submitted for the degree of Doctor of Philosophy with a Major in Civil Engineering and titled "NUMERICAL ANALYSIS AND EXPERIMENTAL INVESTIGATION OF ULTRA-HIGH-PERFORMANCE CONCRETE HYBRID BRIDGE DECK CONNECTIONS" has been reviewed in final form. Permission, as indicated by the signatures and dates below, is now granted to submit final copies to the College of Graduate Studies for approval.

Major Professor: _____ Date: _____
Ahmed Ibrahim, Ph.D., PE

Committee Members: _____ Date: _____
Richard J. Nielsen, Ph.D., PE

S. J. Jung, Ph.D., PE Date: _____

Gabriel Potirniche, Ph.D., PE Date: _____

Department
Chair: _____ Date: _____
Patricia J. S. Colberg, Ph.D., PE

Abstract

In recent years, the use of modular bridge deck components has gained popularity for facilitating more durable components in bridge decks, but these components require field-applied connections for constructing the entire bridge. Ultra-High-Performance Concrete (UHPC) is being extensively used for highway bridges in the field connections between girders and deck panels for its superior quality than conventional concrete.

Thus far, very limited data is available on the modeling of hybrid-bridge deck connections. In this study, finite element models have been developed to identify the primary properties affecting the response of hybrid deck panel system under monotonic and reverse cyclic loads. The commercial software ABAQUS was used to validate the models and to generate the data presented herein. The concrete damage plasticity (CDP) model was used to simulate both the conventional concrete and UHPC. In addition, numerical results were validated against experimental data available in the literature. The key parameters studied were the mesh size, the dilation angle, reinforcement type, concrete constitutive models, steel properties, and the contact type between the UHPC and the conventional concrete. The models were found to capture the load – deformation response, failure modes, crack patterns and ductility indices satisfactorily. The damage in concrete under monotonic loading is found higher in normal concrete than UHPC with no signs of de-bonding between the two materials. It is observed that increasing the dilation angle leads to an increase in the initial stiffness of the model. Changing the dilation angle from 20° to 40° results in an increase of 7.81% in ultimate load for the panel with straight reinforcing bars, whereas for the panel with headed bars, the increase in ultimate load was found 8.56 %.

Furthermore, four different types of bridge deck panels were simulated under reversed cyclic loading to observe overall behavior and the damage pattern associated with the reversed cyclic load. The key parameters investigated were the configurations of steel connections between the precast concrete deck elements, the loading position, ductility index, and the failure phenomena. The headed bar connections were found to experience higher ductility than the ones with straight bars in the range of 10.12% to 30.70% in all loading conditions, which is crucial for ensuring safe structural performance. This numerical investigation

provides recommendations for predicting the location of the local damage in UHPC concrete bridge deck precast panel connections under reversed cyclic loading.

Despite of having excellent mechanical and material properties, the use of Ultra-High-Performance Fiber Reinforced Concrete (UHP-FRC) is not widespread due to its high cost and lack of widely accepted design guidelines. This research also aims to develop a UHPC mixture using locally and domestically available materials without heat curing in hopes of reducing the production cost. Several trial mixtures of UHPC have been developed using locally available basalt and domestically available steel fibers. Among them, one trial mixture of 20.35 ksi compressive strength was selected for further study. To investigate the applicability of this locally produced UHPC in bridge closure, two full scale-8 ft. span hybrid bridge deck slabs with UHPC closure were constructed and tested under monotonic loading to identify the structural and material responses. The load- deflection response of the hybrid connection confirms that the deflection increased linearly until the initiation of first crack, after that it increased non-linearly up to the failure of the connection. The strain response also confirms that UHPC experiences less strain than normal strength concrete under compression loading. In addition, a moment curvature analytical graphical user interface model of hybrid bridge deck connection has been developed using MATLAB to predict ductility, curvature, and the stress distributions in those connections. The predicted value of moment and curvature from the code was found in good agreement with experimental data as well. The code provides a tool to professional engineers to predict ductility, curvature, and the stress distributions in those connections. The code is built in such a way to allow various input parameters such as concrete strength, dimensions of hybrid connection and deck panels, reinforcement configuration and the shape of the connection.

Though, ultra-high-performance fiber reinforced concrete (UHP-FRC) has very high compressive strength compared to conventional concrete, the failure strain of UHP-FRC is not enough to withstand large plastic deformations under high strain rate loading such as impact and blast loading. Hence, a numerical study has been conducted to simulate low-velocity impact phenomenon of UHP-FRC. The responses obtained from the numerical study are in good agreement with the experimental results under impact loads. Five different types of UHP-FRC beams were simulated under impact loading to observe the global and local

material responses. The key parameters investigated were the reinforcement ratio (ρ), impact load under various drop heights (h), and the failure phenomena. It was observed that higher reinforcement ratio showed better deflection recovery under the proposed impact. Also, for a specific reinforcement ratio, the maximum deflection increases approximately 15% when drop height decreases from 100 mm to 25 mm. Moreover, the applicability of concrete damage plasticity model for impact loading is investigated. The results also provided recommendations for predicting the location of the local damage in UHP-FRC beams under impact loading.

Moreover, this research work includes a nonlinear finite element analysis of high-strength concrete confined with opposing circular spiral reinforcements. The spiral reinforcement is a very common technique used for reinforcing columns in active seismic regions due to its high ductility and high energy absorption. The results are compared with previously tested small-scale concrete columns made with the same technique under monotonic axial loads. The proposed technique is developed to improve the strength and ductility of concrete columns confined with conventional spiral systems. The finite element (FE) analysis results have shown that the proposed model can predict the failure load and crack pattern of columns with reasonable accuracy. Beside this, the concrete plasticity damage showed very good results in simulating columns with opposing spirals. The FE model is used to conduct a study on the effect of spiral spacing, γ (ratio of the core diameter to the whole cross section diameter) and compressive strength on the behavior of circular spiral reinforced concrete columns confined with opposing circular spiral reinforcements. The results of the parametric study demonstrated that for the same spacing between spirals and same strength of concrete, increasing γ increases the failure load of the column. It is also observed from the study that the ductility of the studied columns is not affected by changing the value of γ . In addition, a correlation between the γ factor, three different compressive concrete strengths, and the spacing of opposing spirals was developed in this study.

Acknowledgements

To my supervisor, Dr. Ahmed Ibrahim, I would like to express my gratitude for the motivation, support, and guidance he provided me throughout my research work. His valuable comments and insights helped me to improve my work enormously. I really appreciate the time and effort he dedicated to me for achieving my research goals and the way he promptly responded to my difficulties and queries. Working with him was an excellent opportunity to me for learning engineering knowledge as well as practical experience. Needless to say, none of this would have been possible without his help and direction.

My sincere and profound thanks are due to Dr. Richard Nielsen, Dr. S. J. Jung and Dr. Gabriel Potirniche for serving as members of my dissertation reviewing committee and guiding me towards the Ph.D. degree.

I would also like to thank all my lab mates Mahmoud, Tawfeeq, Kevin, Robin, Al-Assi, Abdulallah, Niyi, Charles, Simpson, Eric, and Ebenezer for helping me throughout the testing of the specimens. Also, special thanks to Don Parks for his technical supports. Without his help and constant support, it would not be possible for me to execute the experimental program. Additional thanks go to Pre-mix Concrete Plant, and Poe Asphalt Plant for their generous support by donating all high strength concrete and mix design materials required for it.

I greatly appreciate all the support provided by the Department of Civil and Environmental Engineering at the University of Idaho for completing this research. Acknowledgement is due to the University of Idaho for the support given to this research through its facilities and granting me the opportunity to pursue my graduate studies and fulfill my dream.

Dedication

This work is dedicated to my father Late Md. Nazmul Islam Miah, Ph.D., my mother Meherun Nessa Khan, my husband Nurullah Bin Humayun, my brother Dr. Manzurul Islam and all my friends and family. Without their moral support, this would not have been possible.

Table of Contents

Authorization to Submit Dissertation	ii
Abstract	iii
Acknowledgements	vi
Dedication	vii
Table of Contents	viii
List of Tables	xiii
List of Figures	xiv
Chapter 1: Finite-Element Modeling of UHPC Hybrid Bridge Deck Connections.....	1
Abstract	1
Introduction	2
Experimental Program.....	3
Finite Element Modeling.....	5
Precast Panels	5
Concrete model proposed by Hsu and Hsu (1994)	6
Concrete model proposed by Park and Paulay (1975).....	6
Concrete model proposed by Saenz (1964)	7
UHPC.....	8
Reinforcing steel.....	10
Sensitivity Analysis.....	13
Effect of Concrete Model	14
Effect of Dilation Angle	15
Effect of Steel Properties	16
Convergence Study	18
Contact modeling	19

Validation of the Finite element Model	20
Structural Performance under Low Cyclic Loading	24
Load-deformation response	25
Axial strain response of reinforcing steel	28
Failure of the specimens	29
Conclusions	30
References	32
Chapter 2: Flexural Response of UHPC Bridge Deck Connections Made with Idaho Local Materials	35
Abstract	35
Introduction	35
Theoretical Concepts of UHPC Production	37
Reduction in Porosity	37
Improvement of Microstructure.....	38
Enhancement in Homogeneity.....	39
Increase in Toughness	39
Development of UHPC with Local Materials	39
Material Constituents.....	41
Mix Designs.....	43
Flow Table Test.....	45
Compressive Strength Test.....	45
Flexural Response of UHPC Hybrid Bridge Deck Connection made with Local Material	47
Reinforcement Details	47
Construction of Specimens	48
Material Properties	50

High Strength Concrete.....	50
UHPC.....	52
Experimental Setup	55
Instrumentation.....	55
Strain Gauges.....	56
Stage One: Fixing Reinforcement Strain Gauges in the bottom bar and connection ..	56
Stage Two: Fixing of Concrete Strain Gauges and LVDT	57
Test Results and Discussion.....	57
Development of Moment-Curvature Relationship.....	60
Analytical Investigation	60
Validation of Analytical Model.....	65
Graphical User Interface (GUI) for Parametric Study	67
Conclusions	69
References	70
Chapter 3: Numerical Study on the Low-Velocity Impact Response of Ultra-High-	
Performance Fiber Reinforced Concrete Beams.....	74
Abstract	74
Introduction	74
Experimental Program.....	76
Finite Element Modeling.....	77
Material Constitutive Models	78
<i>Concrete damage plasticity model for low-velocity impact modeling</i>	78
UHP-FRC constitutive model.....	79
Steel-reinforcement constitutive model	82
Mesh configuration, Load and boundary condition.....	83

Sensitivity Analysis.....	84
Effect of Dilation Angle	84
Effect of Shape Factor	85
Effect of Stress Ratio (σ_{b0}/σ_{c0}).....	86
Validation of Finite Element Modeling	87
Results and Discussion.....	91
Effect of Reinforcement Ratio.....	92
Effect of Drop Height of Impact Load	94
Axial Strain Response under Impact Load	95
Time lag in Impact Test.....	97
Conclusions	98
References	99
 Chapter 4: Finite Element Analysis of Confined High Strength Concrete Bridge Columns with Opposing-Spiral Reinforcement	
Abstract	103
Introduction	104
Experimental Program.....	106
Finite Element Modelling.....	107
Material Properties	107
Steel reinforcing bars	108
Concrete	108
Results and Discussions	110
Verification of the Finite Element Model.....	110
Parametric Study.....	113
Axial stress versus axial strain response	114

Effect of Spiral Spacing	116
Conclusions	117
References	118
Chapter 5: Conclusions and Recommendations	120
Conclusions	120
Recommendations	121
Appendix A - Permissions	122

List of Tables

Table 1.1: Test Specimen (Graybeal, 2010)	3
Table 1.2: Concrete parameters used in the plastic damage model	8
Table 1.3: Ultrahigh-Performance Concrete parameters used in the plastic damage model (Chen & Graybeal, 2010).....	9
Table 1.4: Parameters of reinforcing steel	10
Table 1.5: Variables used for sensitivity analysis.....	13
Table 1.6: Comparison between FEM and Experimental results	24
Table 1.7: Displacement and ductility ratio	28
Table 2.1: Grain Size Distribution of Fine Aggregate	41
Table 2.2: Physical properties of steel fiber.....	42
Table 2.3: Mixture proportion of UHPC.....	44
Table 2.4: Compressive strength of UHPC.....	46
Table 2.5: Concrete Mix Design.....	50
Table 2.6: UHPC mix design	53
Table 3.1: Mix Proportions of UHPFRC (Yoo et al. 2015).....	77
Table 3.2: Ultra-High-Performance Concrete parameters used in the plastic damage model	82
Table 3.3: Parameters of reinforcing steel	83
Table 3.4: Sensitivity Analysis results.....	87
Table 3.5: Summary of the test and FEM results.....	88
Table 4.1. Parameters Used for the Concrete in Plastic Damage Model.	109
Table 4.2. Column samples used in the finite element verification.....	111

List of Figures

Figure 1.1: Reinforcement details for panel 8H (Graybeal 2010)	4
Figure 1.2: Reinforcement details for panel 8G (Graybeal 2010)	5
Figure 1.3: Axial stress-strain behavior for UHPC (a) in Compression and (b) in Tension (Graybeal 2006a)	9
Figure 1.4 Displacement time history (8H)	11
Figure 1.5: (a) Concrete mesh configuration (b) Reinforcement details (straight bars) (c) Reinforcement details (headed bars).....	12
Figure 1.6: Effect of concrete models (a) 8G and (b) 8H	15
Figure 1.7: Effect of Dilation Angle (a) 8G and (b) 8H	16
Figure 1.8: Effect of Steel Properties (a) 8G and (b) 8H	17
Figure 1.9: Axial stress vs axial strain response for the reinforcement steel at the UHPC connection	18
Figure 1.10: Convergence Study for 8G	19
Figure 1.11: Effect of Contact Model	20
Figure 1.12: Load vs Displacement response at mid span.....	20
Figure 1.13: Damage (a) in Compression and (b) in Tension (FEM) (c) in Tension, (Graybeal, 2010)	22
Figure 1.14: Damage in tension around (a) headed bar (b) straight bar	22
Figure 1.15: Strain response of NSC and UHPC in compression and tension (8H).....	23
Figure 1.16 Displacement-time history.....	25
Figure 1.17: Location of load application (a) at the interface (b) middle of interface and UHPC connection	25
Figure 1.18: Load-deformation response (a) UC-I-S (b) UC-M-S (c) UC-I-H (d) UC-M-H. 26	26
Figure 1.19: Envelope curve of loading cycles.....	27
Figure 1.20: Axial Strain time history of steel reinforcement	28
Figure 1.21: Concrete damage in tension (a) Loading at interface with headed bar (b) Loading at interface with straight bar (c) Loading at the middle of interface and UHPC with headed bar (d) Loading at the middle of interface and UHPC with straight bar	29
Figure 2.1. Sample Sieved Materials	42
Figure 2.2. Steel Fibers	43

Figure 2.3. Horizontal Concrete Mixture.....	43
Figure 2.4. Flow Table Test (M9).....	45
Figure 2.5. Cube Specimen.....	46
Figure 2.6. Stress-strain response of M9 mixture at 28 days.....	47
Figure 2.7. Reinforcement details.....	48
Figure 2.8. Pre-Mix Concrete Plant unloading HSC from their truck outside BEL.....	49
Figure 2.9. Wooden forms before pouring concrete.....	49
Figure 2.10 Casting of precast panels.....	51
Figure 2.11. Samples for conducting 28-day compressive strength.....	51
Figure 2.12 Removal of formworks.....	52
Figure 2.13 Form work for UHPC connection.....	53
Figure 2.14 (a) Sieving procedure (b) Sieved materials (#50 passing and #100 retained).....	54
Figure 2.15 Deck Panels after UHPC pour.....	54
Figure 2.16. Test Set up.....	55
Figure 2.17. Campbell Scientific CR6 series data logger.....	56
Figure 2.18. LVDT for recording midspan deflection (Underneath the beam).....	57
Figure 2.19. Load -Deflection Response for UHPC hybrid bridge connection made with Idaho local materials.....	58
Figure 2.20. (a) Crack pattern observed in flexure, BC-1 (b) Crack pattern observed in flexure, BC-2 (c) Cracks at the bottom surface of the hybrid connection, BC-1 (b) Cracks at the bottom surface of the hybrid connection, BC-2.....	59
Figure 2.21. (a) BC-1 (b) BC-2.....	60
Figure 2.22. Cross section, Strain, and Stress Diagram of the connection.....	64
Figure 2.23. Flow diagram of the numerical process.....	65
Figure 2.24. Whitney stress block for calculating moment-curvature relationship.....	66
Figure 2.25. Moment-Curvature diagram for a specific cross section.....	66
Figure 2.26. Comparison between analytical and experimental load-deflection response.....	67
Figure 2.27: Graphical User Interface (after initialization).....	68
Figure 2.28: Graphical User Interface (after plotting).....	69
Figure 3.1: (a) Experimental Program (b) cross section details of UH-N (c) UH-S-0.53% (Yoo et al. 2015).....	77

Figure 3.2: (a) The yield surface in the deviatoric plane for different K_c values (b) yield surface in meridian plane.....	79
Figure 3.3: (a) Compressive behavior of UHPFRC (Yoo et al. 2015) (b) Tensile behavior of UHPFRC (Al-Osta et al. 2017).....	80
Figure 3.4: (a) Concrete compressive hardening (b) Concrete tension stiffening (ABAQUS Analysis User's Manual, 6.10).....	81
Figure 3.5: Load and Boundary condition	83
Figure 3.6: Mesh Configuration.....	84
Figure 3.7: Effect of dilation angle on midspan deflection (a) UH-N (b) UH-S-0.53%	85
Figure 3.8: Effect of shape factor on midspan deflection (a) UH-N (b) UH-S-0.53%.....	86
Figure 3.9: Effect of shape factor on midspan deflection (a) UH-N (b) UH-S-0.53%.....	86
Figure 3.10: Deflection-time history at midspan	88
Figure 3.11: Comparison of maximum and residual deflections between experimental program and FEM.....	89
Figure 3.12: Internal energy-time history of whole beam	89
Figure 3.13: Crack Pattern of UH-N (top: experiment Yoo et al. 2015; bottom : FE).....	90
Figure 3.14: Crack Pattern of UH-S-0.53% (top: experiment, Yoo et al. 2015; bottom : FE).....	91
Figure 3.15: Cross Sections of (a) UH-0S-50 (b) UH-0.53S-50 (c) UH-1.05S-50 (d) UH-1.71S-50 (e) UH-2.28S-50.....	92
Figure 3.16: (a) Deflection-time history (b) Comparison of maximum and residual deflections according to reinforcement ratio	93
Figure 3.17: Deflection-time history for different drop heights (a) $\rho = 0\%$ (b) $\rho = 1.71\%$..	94
Figure 3.18: Tensile Strain -time history	95
Figure 3.19: Strain response under impact loading (a) $\rho=0\%$ (b) $\rho=2.28\%$	96
Figure 3.20: Impact load and reaction time history (a) $\rho=1.71\%$ (b) $\rho=2.28\%$	97
Figure 4.1: Specimen comparison, opposing spiral spacing of (S), single spiral spacing of (S), opposing spiral spacing of (2S) (Marvel 2014).	106
Figure 4.2: Schematic representation of test specimen (Marvel et al. 2014).....	108
Figure 4.3: Stress-Strain curve of reinforcing steel bars and spirals.	108
Figure 4.4: σ - ϵ in compression and σ - ϵ in tension for CDP model [ABAQUS]	109
Figure 4.5: The compression concrete inelastic stress-strain curve.....	110

Figure 4.6. The FE mesh for concrete, the reinforcing steel, and the boundary conditions.	111
Figure 4.7: Comparison of Stress-Strain behavior between the experimental and the FEM.	113
Figure 4.8. Comparison of concrete damage between the experimental and the FEM.	114
Figure 4.9: Axial Stress vs Axial Strain response for different γ	114
Figure 4.10: Axial load vs γ for different concrete strength.	116
Figure 4.11. Confined Axial Stress vs Spiral Spacing for different f'_c	117

Chapter 1: Finite-Element Modeling of UHPC Hybrid Bridge Deck Connections

“Finite-element modeling of UHPC hybrid bridge deck connections”, published in *International Journal of Advanced Structural Engineering*, September 2018, Volume 10, Issue 3, pp 199–210

Abstract

In recent years, linked bridge deck elements have gained popularity for facilitating more durable components in bridge decks, however these components require field-applied connections for constructing the entire bridge. Ultra-high-performance concrete (UHPC) is becoming a major material for closure pours in bridges and various department of transportation have been developing guidelines. UHPC is known for its superior quality over conventional concrete in terms of constructability, strength and durability. So far, very limited data are available on the finite-element modeling (FEM) of hybrid bridge deck connections. In this study, finite element models have been presented to define the crucial factors affecting the response of bridge hybrid deck panel systems under monotonic loads. The commercial software ABAQUS was used to validate the failure modes and to generate the data presented herein and the concrete damage plasticity was used to simulate both conventional concrete and UHPC. Numerical results were validated using available experimental data in literature. The key parameters studied were the mesh size, the dilation angle, reinforcement type, concrete models, steel properties, and the contact behavior between the UHPC and the conventional concrete. The models were found to capture the load–deflection response of experimental results, failure modes, crack patterns and ductility indices show satisfactorily response. A sensitivity test was also conducted by considering various key parameters such as concrete and steel constitutive models and their associated parameters, mesh size, and contact behavior. It is perceived that increasing the dilation angle leads to an increase in the initial stiffness of the model. The damage in concrete under monotonic loading is found higher in normal concrete than UHPC with no signs of de-bonding between the two materials. Changing the dilation angle from 20° to 40° results in an increase of 7.81% in ultimate load for the panel with straight reinforcing bars, whereas for the panel with headed bars, the increase in ultimate load was found 8.56%.

Introduction

The ASCE 2017 report card listed that about 9% of bridges in the USA are classified structurally deficient and each year more than 3000 new bridges are being constructed (Bhide 2008). It has been always a challenge for the bridge engineers to find new ways to build better bridges with reduced construction time. So far, significant efforts have been provided in developing innovative ways to increase the long-term structural performance, and currently, the use of UHPC has become more popular in the construction industry for its superior properties such as its early very high strength that might reach 96 MPa (14,000 psi) in 3 days, its promising toughness, and long-term steadiness. The term UHPC is classified as innovative cementitious composite materials, where ground-breaking technology of cement and concrete industry grouped together (Graybeal 2010). In fact, the concept of using UHPC for connection between precast concrete panels started in the mid-90s. At that time, a building was being constructed at Aalborg University using UHPC as a closure pour material, and additional project was completed, where UHPC was used for slab-column connections and its bond characteristics, (Aarup et al. 2009; Hansen and Jensen 1999; Nielsen et al. 1996; Aarup and Jensen 1998). Additional research was completed at Chalmers University focusing on the application of UHPC as closure material (Broo and Broo 1997; Harryson 1999, 2000). Simplicity in construction and outstanding performance made UHPC connection more popular than conventional modular-component connections, where conventional concrete connections require post-tensioning, complex confinement reinforcement, large volume of concrete, etc., (Graybeal 2010). An ample amount of studies has been conducted to investigate the bond strength between UHPC and various materials. Perry and Seibert (2012) reported on applications related to precast joints of UHPC. The bond characteristics between timber and UHPC were studied by Schäfers and Seim (2011). The interfacial behavior of hollow glass fiber-reinforced plastic beams having a UHPC filled compressive zone was examined by El-Hacha and Chen (2012). Graybeal and Swenty (2012) investigated the performances of precast deck joints with variable cross sections. More research has been conducted on developing analytical models to predict the compressive and tensile strength. As it is not always feasible to conduct large-scale test of UHPC connection of bridge deck elements, a need for developing dependable 3D finite-element model is needed. Graybeal (2006a, b, 2008, 2009a, b), performed comprehensive experimental tests

on UHPC characterization, full-scale flexural and shear of I-girders, and pi-girders. Numerical modeling of UHPC connected deck panels has been always challenging due to non-availability of post peak behavior of UHPC either under compression or tension loads. The post-peak behavior is very important to predict the damage parameters needed for numerical modeling (Chen and Graybeal 2012). Different modeling approaches considering diverse assumptions have been proposed, but sensitivity analyses are needed for identifying the major parameters affecting the numerical results. In this paper, a finite-element model is developed which can be applied for a variety of UHPC bridge connections subjected to monotonic loading. The model also recognizes the major factors affecting the numerical results and evaluates the sensitivity of the material input parameters on the variability. The experimental program and finite element modeling are described in the following sections.

Experimental Program

Two full-scale experimentally tested deck panels were selected from Graybeal (2010). The two specimens had two different UHPC connections, where straight and headed bars were used. Table 1.1 provides the details of the two test specimens. The details for each of the specimens, the location of UHPC filled connection, and normal strength concrete deck panels are provided in Figure. 1.1 and 1.2. In all cases, the size of the test specimens was 2400×2152 mm (94.5×84.7 inch). The diamond shape UHPC connection runs parallel to the length of the slab specimen with a 152 mm (6 inch) nominal width, as shown in Figure 1.1. No post-tensioning was included in the test panels and the connection reinforcements were extended from the adjacent precast slabs into the UHPC connection, (Graybeal 2010).

Table 1.1: Test Specimen (Graybeal, 2010)

Specimen	Orientation	Depth	Reinforcement
8H	Transverse	200 mm	16M (#5) headed black reinforcement with 90 mm lap length and 450 mm (top) and 180 mm (bottom) spacing
8G	Transverse	200 mm	16M (#5) galvanized straight bars with 150 mm lap length and 450 mm (top) and 180 mm (bottom) spacing

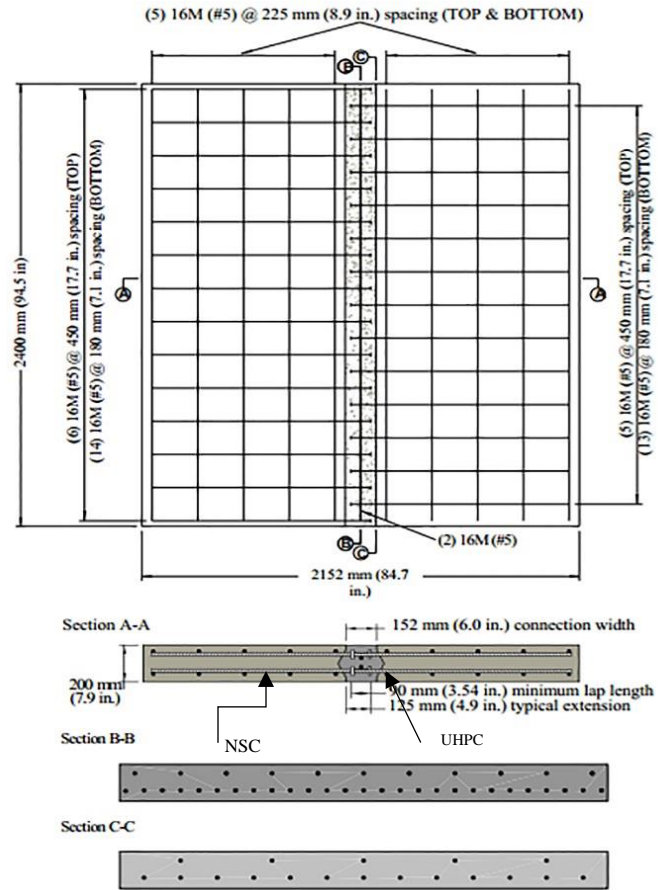


Figure 1.1: Reinforcement details for panel 8H (Graybeal 2010)

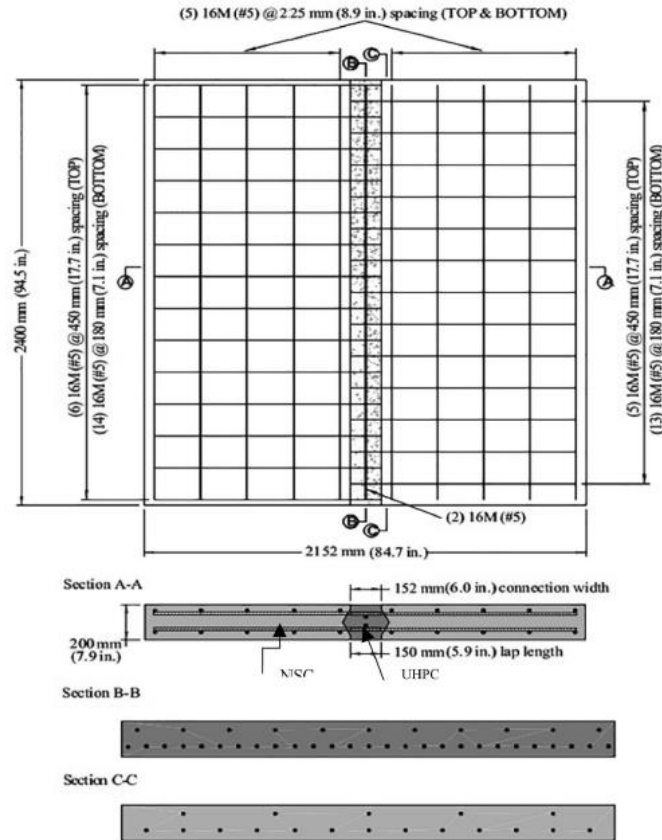


Figure 1.2: Reinforcement details for panel 8G (Graybeal 2010)

Finite Element Modeling

The numerical simulations were conducted using the ABAQUS code, which is a general FE analysis software for modeling the nonlinear material behavior, interaction between different materials, heat transfer, fluid dynamics problem etc. Both implicit and explicit numerical methods are available in ABAQUS for solving problems associated with large deformation and multi-loading environments. ABAQUS/Explicit method was used for simulating the FE models as it can effectively handle severely nonlinear behavior.

Precast Panels

Various models are available in the ABAQUS software library to model the concrete material. The “concrete damaged plasticity” model used in this paper was developed by (Lubliner et al., 1989) and then elaborated by (Lee & Fenves, 1998). The constitutive relationships in the model require the following material input parameters:

- Uniaxial stress-strain constitutive relation under compressive and tensile loading.

- Damage parameters d_c and d_t for compressive and tensile load, respectively.

These parameters are used to identify and validate damage and crack patterns of the developed model and compare it with experimental results. Three different concrete constitutive models were adopted in this study to identify the most suitable concrete model. These models were only used to predict the behavior of precast panels.

Concrete model proposed by Hsu and Hsu (1994)

The concrete model derived by Hsu and Hsu (1994) is limited to a concrete compressive strength of 62 MPa. For other concrete grades, modifications should be made by referring to the original work reported by Hsu and Hsu (1994). This model assumes a linear stress-strain relationship up to 50% of the ultimate compressive strength (σ_{cu}) in the ascending portion. The model was only used to predict the compressive stresses from $0.5\sigma_{cu}$ to $0.3\sigma_{cu}$ in the descending portion.

$$\sigma_c = \left(\frac{\beta \left(\frac{\varepsilon_c}{\varepsilon_0} \right)}{\beta - 1 + \left(\frac{\varepsilon_c}{\varepsilon_0} \right)^\beta} \right) \sigma_{cu} \quad (1.1)$$

where, the parameter β depends on the shape of the stress-strain diagram and is given by:

$$\beta = \frac{1}{1 - \left[\frac{\sigma_{cu}}{\varepsilon_0 E_0} \right]} \quad (1.2)$$

$$\varepsilon_0 = 8.9 \times 10^{-5} \sigma_{cu} + 2.114 \times 10^{-3} \quad (1.3)$$

The initial tangential modulus, E_0 is given by

$$E_0 = 1.243 \times 10^2 \sigma_{cu} + 3.28312 \times 10^3 \quad (1.4)$$

Concrete model proposed by Park and Paulay (1975)

This model considers concrete as an elastic-plastic and strain hardening material. The constitutive relation in compression is assumed to follow this expression:

$$f_c = f' \left[\frac{2\varepsilon_c}{\varepsilon_0} - \left(\frac{\varepsilon_c}{\varepsilon_0} \right)^2 \right] \quad (1.5)$$

Where, f' is the cylinder compressive strength of concrete in MPa. ε_0 , is the strain at peak stress and; ε_{cu} is the crushing strain.

Concrete model proposed by Saenz (1964)

The uniaxial compressive stress-strain relationship proposed by Saenz (1964) is as follows:

$$\sigma_c = \frac{E_c \varepsilon_c}{1 + (R + R_E - 2) \left(\frac{\varepsilon_c}{\varepsilon_0}\right) - (2R - 1) \left(\frac{\varepsilon_c}{\varepsilon_0}\right)^2 + R \left(\frac{\varepsilon_c}{\varepsilon_0}\right)^3} \quad (1.6)$$

Where,

$$R = \frac{R_E (R_\sigma - 1)}{(R_\varepsilon - 1)^2} - \frac{1}{R_\varepsilon}, \quad R_E = \frac{E_c}{E_0}, \quad E_0 = \frac{f'_c}{\varepsilon_0}$$

Where, $R_E = 4$ and $R_\sigma = 4$

Concrete compression and tension damage parameters were calculated using the following equations which were proposed by Birtel and Mark, (2006)

$$d_c = 1 - \frac{\sigma_c E_c^{-1}}{\varepsilon_c^{pl} \left(\frac{1}{b_c} - 1\right) + f_c E_c^{-1}} \quad (1.7)$$

where

d_c = Concrete compression damage parameter

f_c = Compressive Stress

E_c = Modulus of elasticity of concrete

ε_c^{pl} = Plastic strain corresponding to compressive strength

b_c = Constant ranges $0 < b_c < 1$

$$d_t = 1 - \frac{\sigma_t E_c^{-1}}{\varepsilon_t^{pl} \left(\frac{1}{b_t} - 1\right) + f_t E_c^{-1}} \quad (1.8)$$

where

d_t = Concrete tension damage parameter

f_t = Tensile Stress

E_c = Modulus of elasticity of concrete

ϵ_t^{pl} = Plastic strain corresponding to tensile strength

b_t = Constant ranges $0 < b_t < 1$

The concrete parameters used in the plastic damage model are shown in Table 1.2.

Table 1.2: Concrete parameters used in the plastic damage model

Concrete Strength (MPa)	Mass Density (ton/mm ³)	Young's Modulus (MPa)	Poisson's Ratio	Dilation Angle ψ (Degrees)	Eccentricity (ϵ)	f_{bo}/f_{co}	b_c / b_t
45	2.4E-009	26764.7	0.2	20, 36,40	0.1	1.16	0.7

UHPC

Very limited analytical model has been developed for predicting the compressive and tensile behavior of UHPC up to the knowledge of the authors. The UHPC compressive strength was 210 MPa and the tensile strength was taken as 6.40 MPa (Graybeal 2006a). Figure 1.3 shows the stress-strain history of the UHPC used in this study and provided as input in ABAQUS.

Concrete compression damage parameter that was used based on equations 1.7 and 1.8 (Birtel and Mark, 2006). Table 1.3 shows the input parameters used in the damage model.

(a)

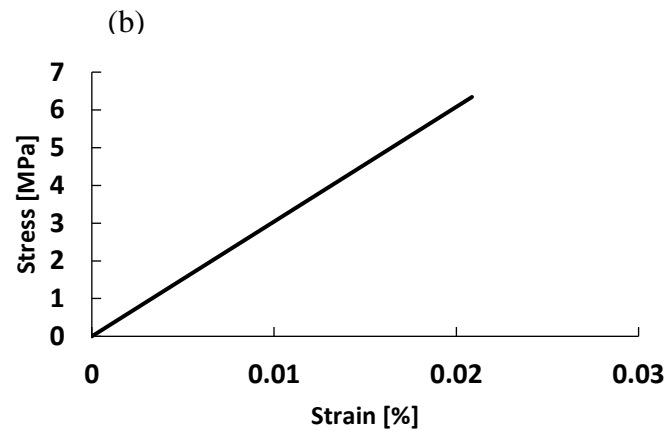
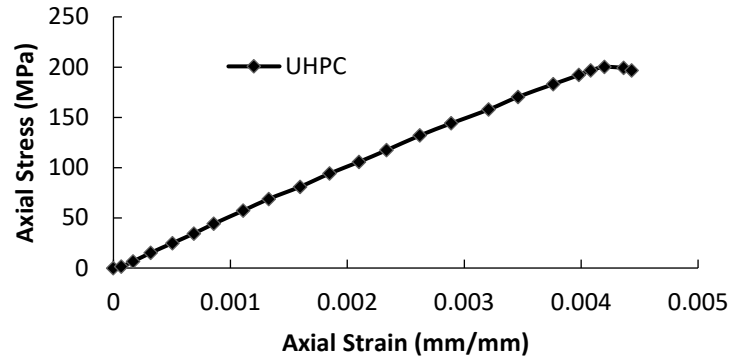


Figure 1.3: Axial stress-strain behavior for UHPC (a) in Compression and (b) in Tension
(Graybeal 2006a)

Table 1.3: Ultrahigh-Performance Concrete parameters used in the plastic damage model
(Chen & Graybeal, 2010)

Concrete	Mass	Young's	Poisson's	Dilation	Eccentricity	f_{bo}/f_{co}	b_c/b_t
Strength	Density	Modulu	Ratio	Angle ψ	ϵ		
(MPa)	(ton/m	s		(Degrees)			
	m^3)	(MPa)					
210	2.565E-	53000	0.18	15	0.1	1.16	0.7
	009						

Reinforcing steel

Reinforcing steel has been modeled using a 2-noded linear 3-D truss element (T3D2), however solid elements were used to model the headed end. The reinforcing bars within the concrete slab were simulated using the embedded element technique available in ABAQUS. Both elastic-perfectly plastic and bilinear stress-strain curves are tested for the simulation. The other parameters used to define the behavior of reinforcing steel are shown in Table 1.4.

Table 1.4: Parameters of reinforcing steel

Type	Poisson's ratio	Elastic Modulus (MPa)	Mass Density (tonne/mm ³)	Yield Stress (MPa)
Steel	0.3	200,000	7.85E-009	414/517

Panel 8H has been reinforced at the connection using headed bars of 16M (#5) as normal reinforcement whereas panel 8G was reinforced by straight, lapped bars of 16M (#5). The thickness of the headed bars was 12.7 mm (0.5 in) and a diameter of 50.5 mm (1.987 in.). For panels 8H and 8G, the minimum lap length in the connection was 90 mm (3.54 inch) and 150 mm (5.9 inch), respectively. Two additional 16M (#5) bars were provided along the length of the connection between the top and bottom layers. Steel reinforcement is assumed to have perfect bond with concrete as an embedded element in ABAQUS. The mesh configuration and reinforcement details are shown in Figure 1.5.

A displacement-controlled loading was applied to the panels through a rigid steel plate placed on the top of the panels until the failure occurs as reported in the test program which is shown in Figure 1.4. In the experiment, the deck panels were supported by elastomeric pads on the top of steel plates. The roller supports represent the elastomeric pads at both sides of the deck panels. The load was applied in very small increments using the explicit dynamic option in ABAQUS. The edge of the loading plate was parallel to the precast-UHPC interface.

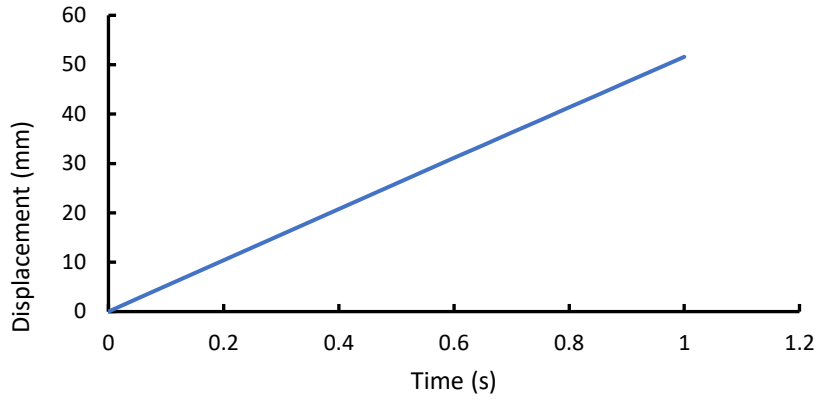
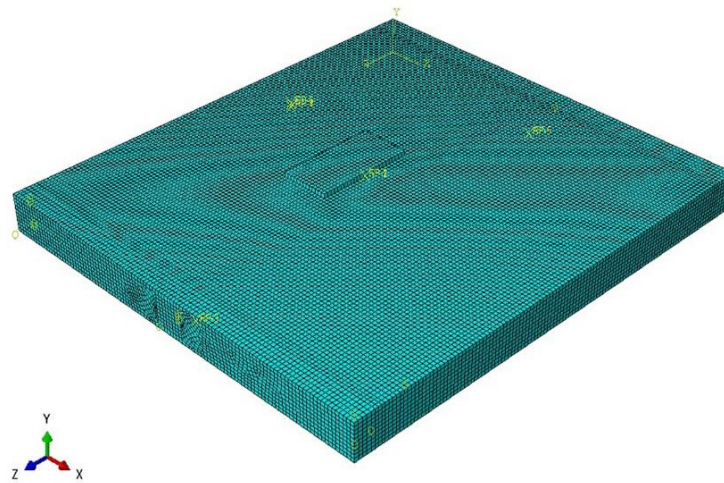
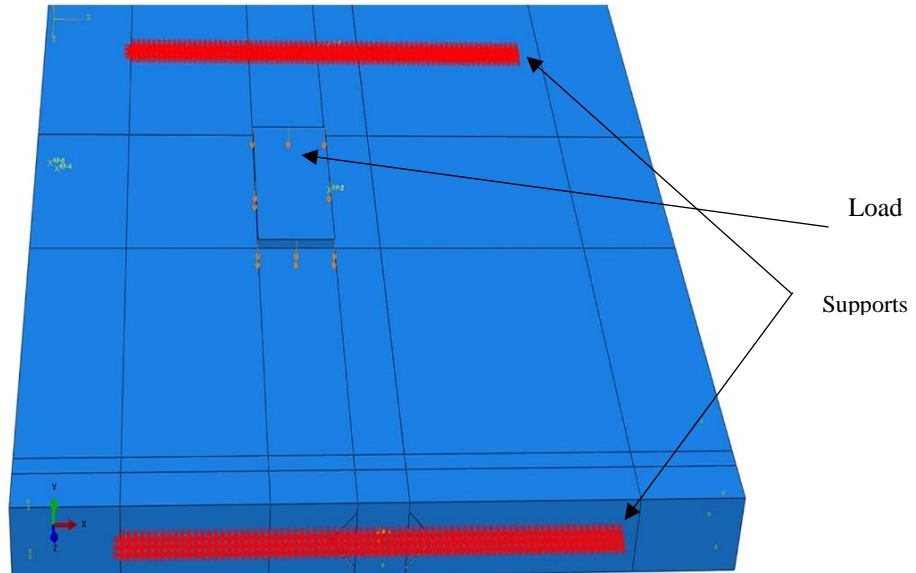
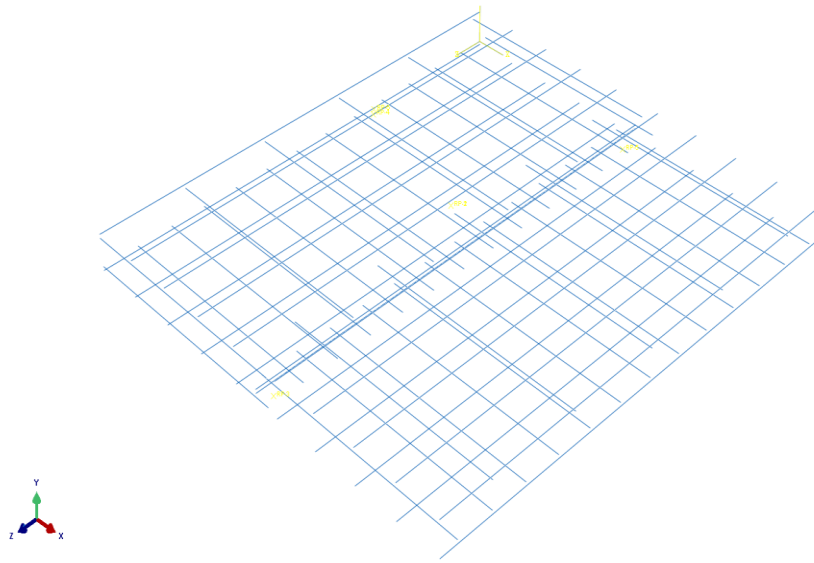


Figure 1.4 Displacement time history (8H)

(a)



(b)



(c)

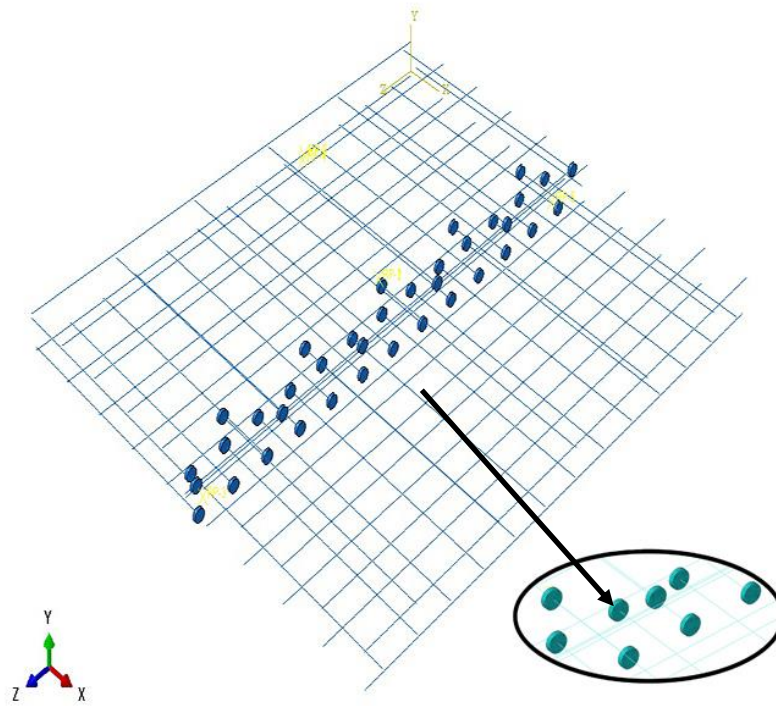


Figure 1.5: (a) Concrete mesh configuration (b) Reinforcement details (straight bars) (c) Reinforcement details (headed bars).

Sensitivity Analysis

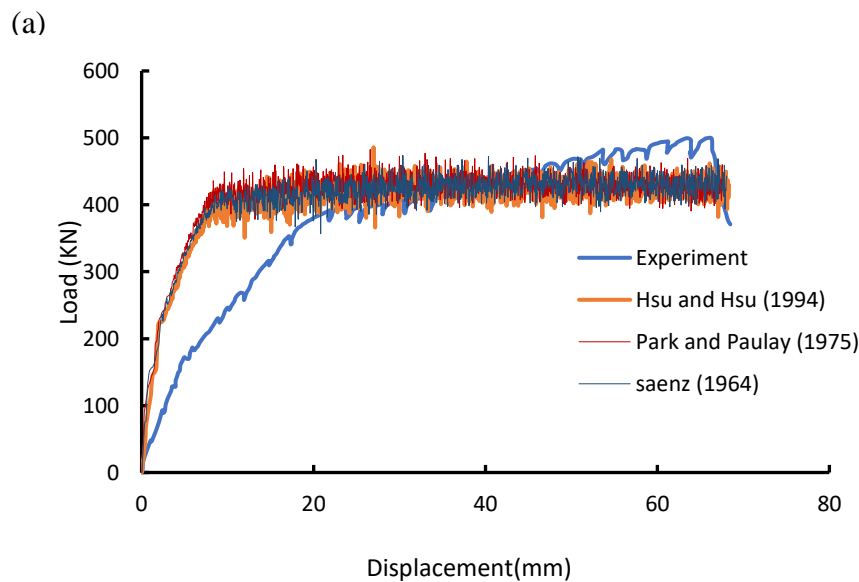
A sensitivity analysis of the numerical models was conducted based on the constitutive models of concrete and steel, concrete input properties such as dilatancy angle and mesh size of the elements. Numerical models for both straight and headed bars were named SB-XYZ-P ϕ and HB-XYZ-P ϕ , where SB and HB stands for straight bar and headed bars, respectively, X represents the initial letter of the concrete constitutive model being used (H, S, and P), Y is the mesh size (5, 10, and 20 mm), Z represents the contact model type used (T for Tie contact and F for friction model), P stands for steel model (E for elastic–perfectly plastic and B for bilinear model) and ϕ is the angle of dilatancy. All these variables are shown in Table 1.5.

Table 1.5: Variables used for sensitivity analysis

Sensitivity Test	Parameters	Straight bars	Headed bars
Mesh size	20mm	SB-H20T-E35°	HB-H20T-E35°
	10 mm	SB-H10T-E35°	HB-H10T-E35°
	5mm	SB-H5T-E35°	HB-H5T-E35°
Dilation angle	$\phi=20$	SB-H20T-E20°	HB-H20T-E20°
	35	SB-H20T-E35°	HB-H20T-E35°
	40	SB-H20T-E40°	HB-H20T-E40°
Concrete Model	Hsu and Hsu (1994)	SB-H20T-E35°	HB-H20T-E35°
	Saenz et. Al (1964)	SB-S20T-E35°	HB-S20T-E35°
	Park & Paulay (1975)	SB-P20T-E35°	HB-P20T-E35°
Steel properties	Elastic-Perfectly Plastic	SB-H20T-E35°	HB-H20T-E35°
	Bilinear	SB-H20T-B35°	HB-H20T-B35°
Contact modeling	Perfect bond (Tie)	SB-P20T-E35°	HB-P20T-E35°
	Penalty (Friction)	SB-P20F-E35°	HB-P20F-E35°
UHPC	All Parameters were constant for all cases		

Effect of Concrete Model

Three different constitutive models of concrete were considered to investigate the overall behavior the UHPC hybrid connections. The ultimate load carrying capacity for the models HB-S20T-E35°, HB-P20T-E35°, HB-H20T-E35° were found 480.21 kN, 486.07 kN and 469.811 kN respectively. For SB-S20T-E35°, SB-P20T-E35° and SB-H20T-E35° the ultimate load carrying capacity was found to be 486.98 kN 473.76 kN and 482.62 kN. Though all the models predicted the ultimate load quite satisfactorily, these models showed stiffer behavior compared to the experimental results which was expected due to the initial cracking developed in the real specimens due to casting, and shrinkage. It is observed from Figure 1.6 that the model proposed by Saenz et al. (1964) indicates a decrease in initial stiffness which is 2% and 45% less than the models proposed by Hsu and Hsu (1994) and Park & Paulay (1975) respectively for headed bar. Concrete damage plasticity (CDP) model was used for modeling both normal strength concrete and UHPC which incorporates both tensile cracking and compressive crushing of concrete. Defining tension stiffening in CDP model is necessary as it can model strain-softening behavior for cracked concrete. Due to unavailability of post-peak behavior of UHPC, the ratio of the strength in the biaxial state to the strength in the uniaxial state, the eccentricity, are assumed in the CDP model.



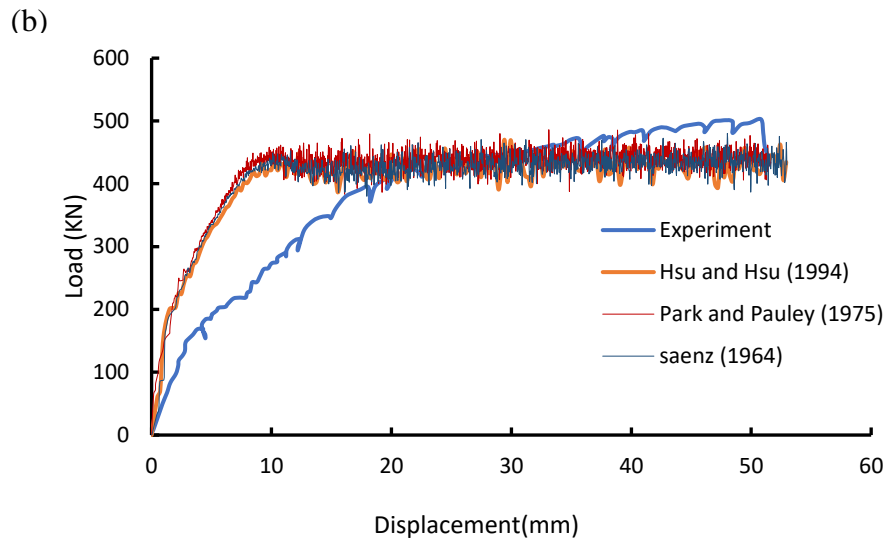


Figure 1.6: Effect of concrete models (a) 8G and (b) 8H

Effect of Dilation Angle

In this section, the angle of dilatancy of concrete was varied from 20° to 40° for the precast concrete. Figure 1.7 shows that the results do not vary drastically as the dilation angle changes. Numerical results from both panels 8G and 8H also showed that higher dilation angle results in slightly higher ultimate load without affecting the initial stiffness. For panel 8G, changing the dilation angle from 20° to 40° results in an increase of 7.81% in ultimate load whereas for panel 8H, the increase in ultimate load was found 8.56%. The amount of dilation depends strongly on the density of the material (ABAQUS). For this reason, increasing confinement results in an increase in the angle of friction. In both 8G and 8H panels, higher dilation angles produced slightly higher initial stiffness which was expected. In case of headed bar specimens, the stiffness of the composite panel for a dilation angle of 40° was found to be 9.69% greater than the stiffness for dilation angle of 20° , whereas for the 8G panel, initial stiffness was found 5.47% higher for the 40° dilation angle.

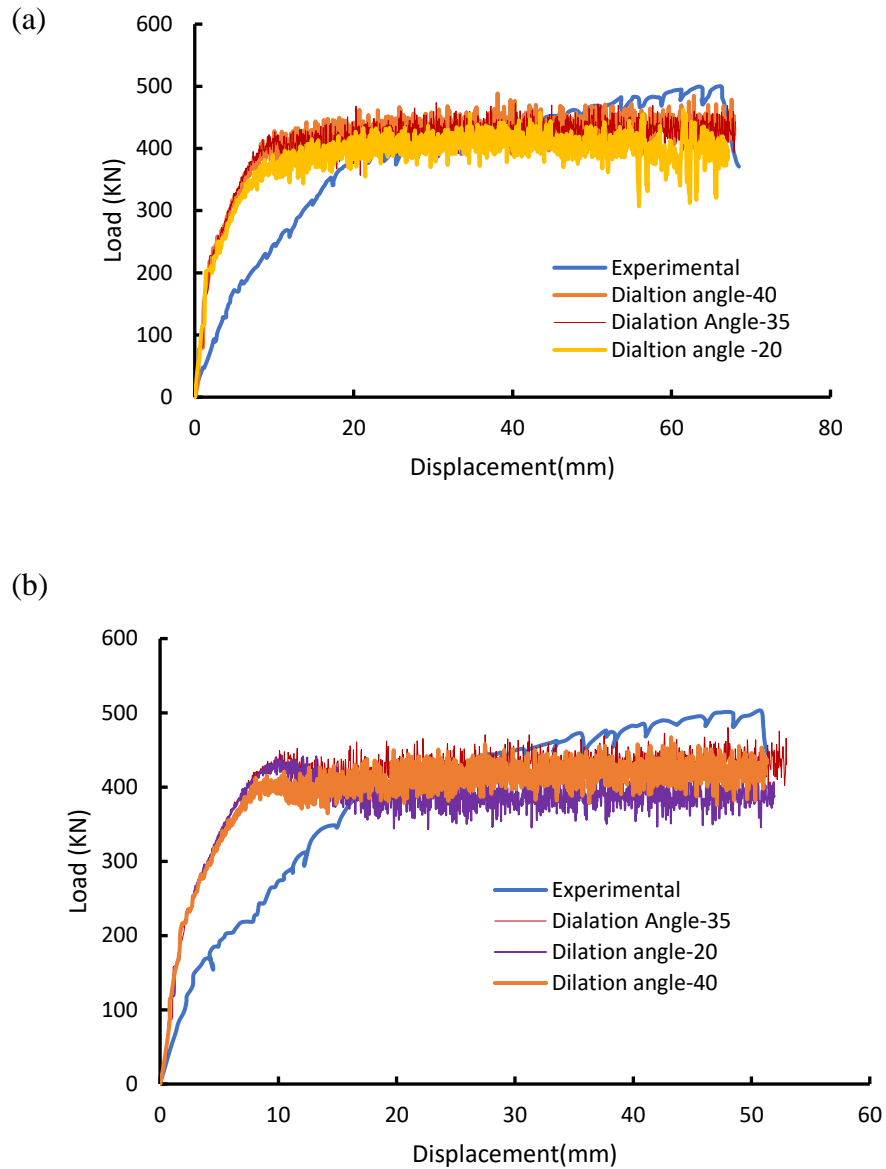


Figure 1.7: Effect of Dilation Angle (a) 8G and (b) 8H

Effect of Steel Properties

Both elastic-plastic and bilinear models of the reinforcement steel were implemented to investigate their effect on the overall performance of the panels. It is evident from Figure 1.8 that the bilinear model of the steel showed lesser stiffness than the elastic-perfectly model and both models showed low stiffness compared to the experimental load-displacement response. The initial stiffness decreased 8% and 20% for 8G and 8H panels respectively

which justifies that the bilinear model could predict the experimental results quite satisfactorily in both panels.

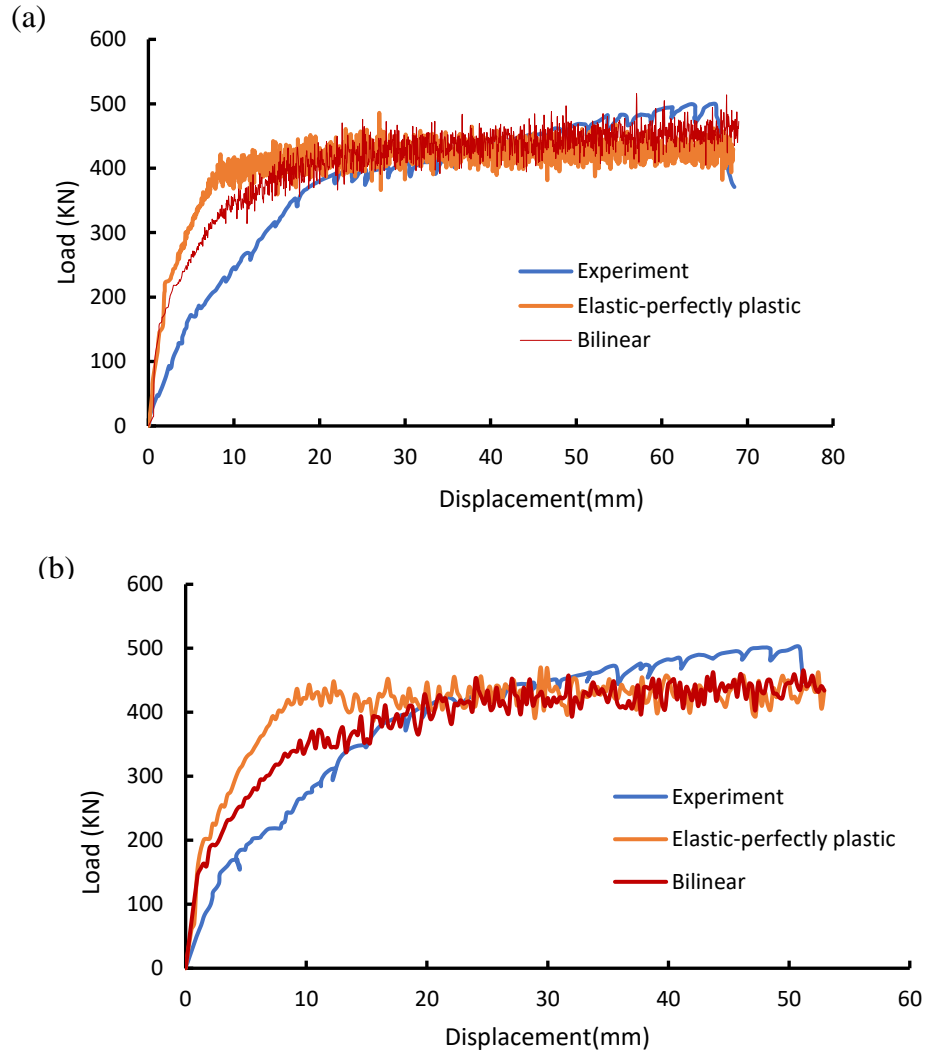


Figure 1.8: Effect of Steel Properties (a) 8G and (b) 8H

The highest strain in steel bars was observed at mid span in the connection between UHPC and normal strength precast concrete. The stress-strain history of the steel bar for both elastic-perfectly plastic and bilinear cases is shown in Figure 1.9. In both cases, the steel bar reached the yield stress which was 414 MPa. It also verifies that the finite element model is in good agreement with the input data provided for steel properties.

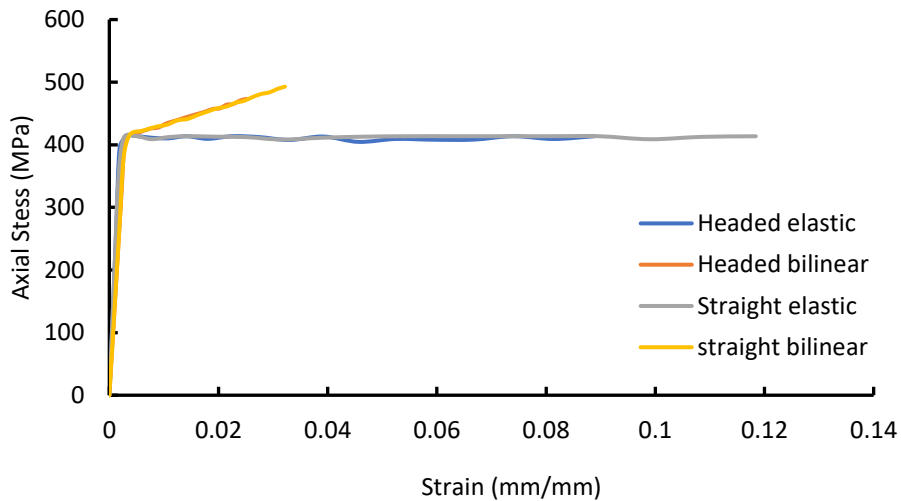


Figure 1.9: Axial stress vs axial strain response for the reinforcement steel at the UHPC connection

Convergence Study

A sensitivity test was carried out to determine optimum mesh size for the simulation to capture the load-displacement response accurately. The numerical simulation was performed for 5 mm, 10 mm and 20 mm mesh size. Figure 1.10 shows that there is no significant change observed between 20 mm and 5 mm mesh size. However, the computational time decreased significantly for coarser mesh. The ultimate load is found 486.98 kN and 490.31 kN for 20 mm and 5 mm mesh respectively which are very close. In consequence, all the simulations were conducted for 20 mm mesh.

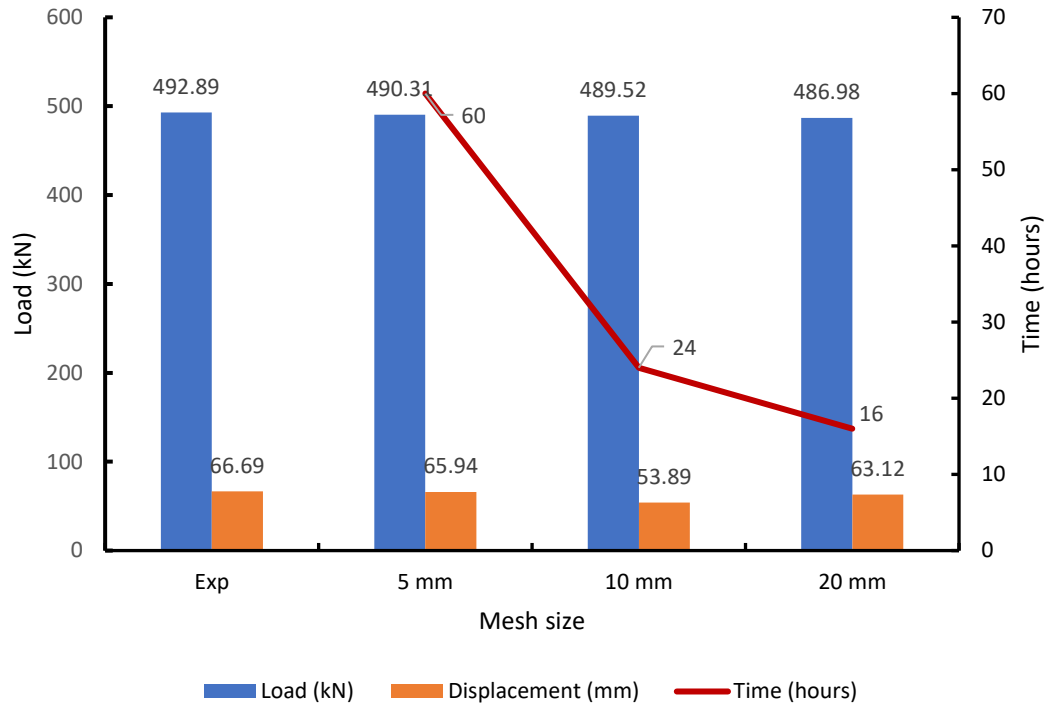


Figure 1.10: Convergence Study for 8G

Contact modeling

The contact between the normal strength precast concrete deck panels and UHPC is the most crucial part to model in ABAQUS because no numerical data available about the behavior of this kind of hybrid connection. Two different kinds of contact properties were used in ABAQUS to predict this behavior. Firstly, a perfect bond between the UHPC and the conventional concrete was assumed and second, a friction model with a friction coefficient of 1.09 (Hussein et al. 2016) was implemented in which little slip between the interfaces (normal concrete and UHPC) was allowed. Figure 1.11 shows that both models were quite capable of predicting the response of experimental program satisfactorily. It seems that the friction model has less stiffness than the perfect bond model which was anticipated though the predicted ultimate load was less than the experimental one.

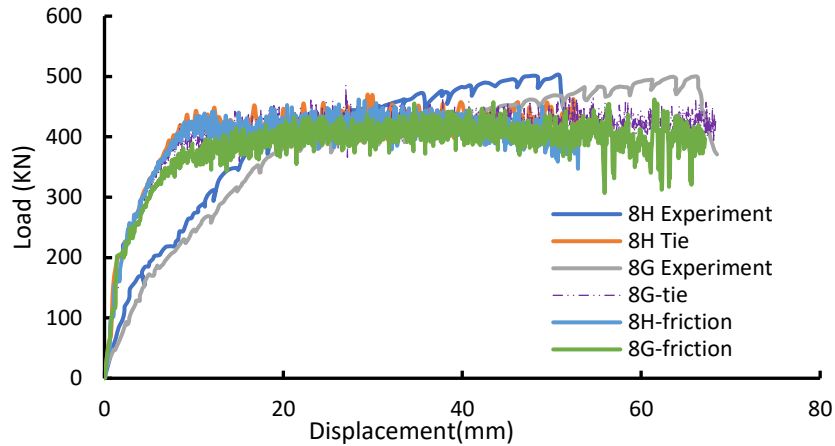


Figure 1.11: Effect of Contact Model

Validation of the Finite element Model

The proposed finite element model has been validated with two full-scale experimentally tested deck panels as described in all the previous sections, which includes both headed and straight reinforcement bars under monotonic loading. The failure mode of deck panels was due to the large deformemim associated with a reduction in ultimate load.. A comparison of full-scale experimentally tested and the finite element model is presented in Figures 1.12 and 1.13 to validate the competency of FEM to observe the failure load, mode of failure and overall behavior of UHPC connection in precast deck panels.

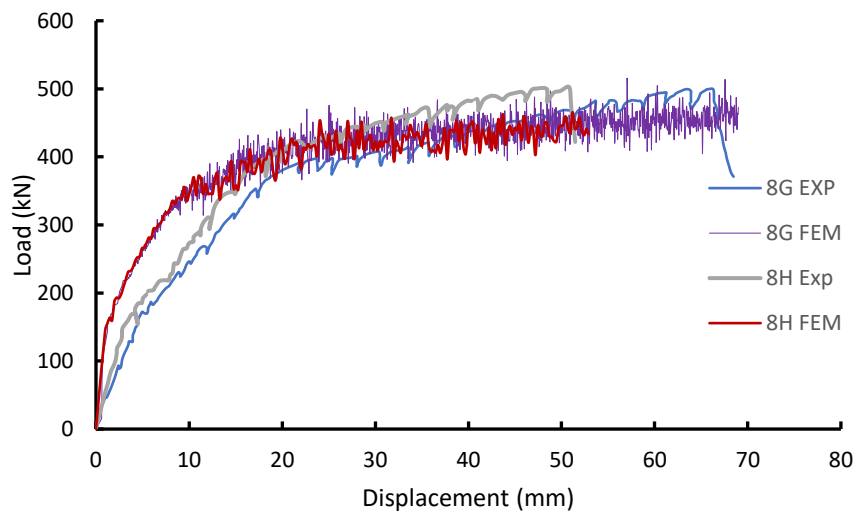
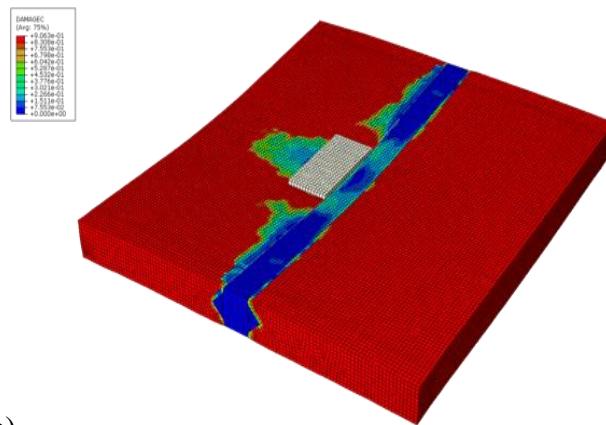


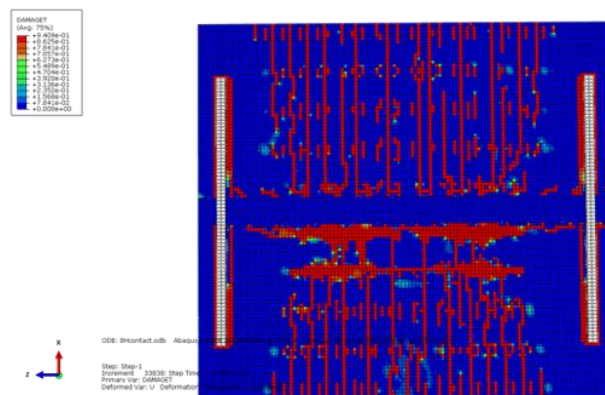
Figure 1.12: Load vs Displacement response at mid span

Figure 1.12 shows that inelastic cracking response continued to increase until the load reaches to approximately 370-390 kN. Up to this level the numerical models showed higher initial stiffness than the experimental ones. Above that load level, the displacement has been changed significantly without noticeable increase in the failure loads. The same behavior is also observed in the experimental results. Figure 1.13 shows the damage in concrete panels both in compression and tension. As UHPC has a higher compressive strength than normal strength concrete, less damage was found in the UHPC connection. It is also apparent from the figure that there is no indication of slip or de-bonding along either of the two connection interfaces which is in good agreement with the experiments. The crack pattern found in the tension side of the deck panels is in good agreement with the cracks observed from the experiment. Figure 1.14 shows the damage pattern found around the reinforcement bars in tension. It is evident from Figure 1.14 (a) and (b) that less damage is found around headed bar.

(a)



(b)



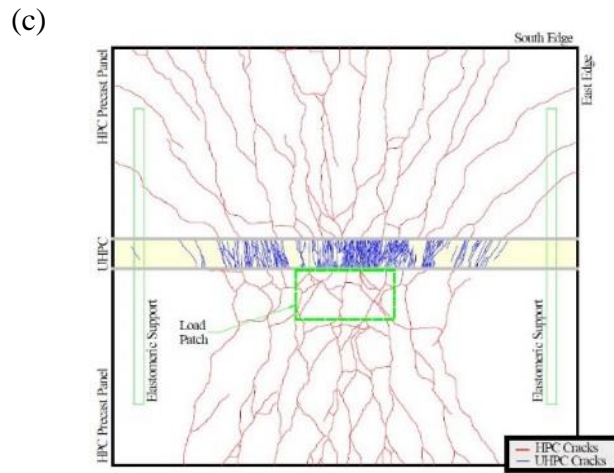


Figure 1.13: Damage (a) in Compression and (b) in Tension (FEM) (c) in Tension, (Graybeal, 2010)

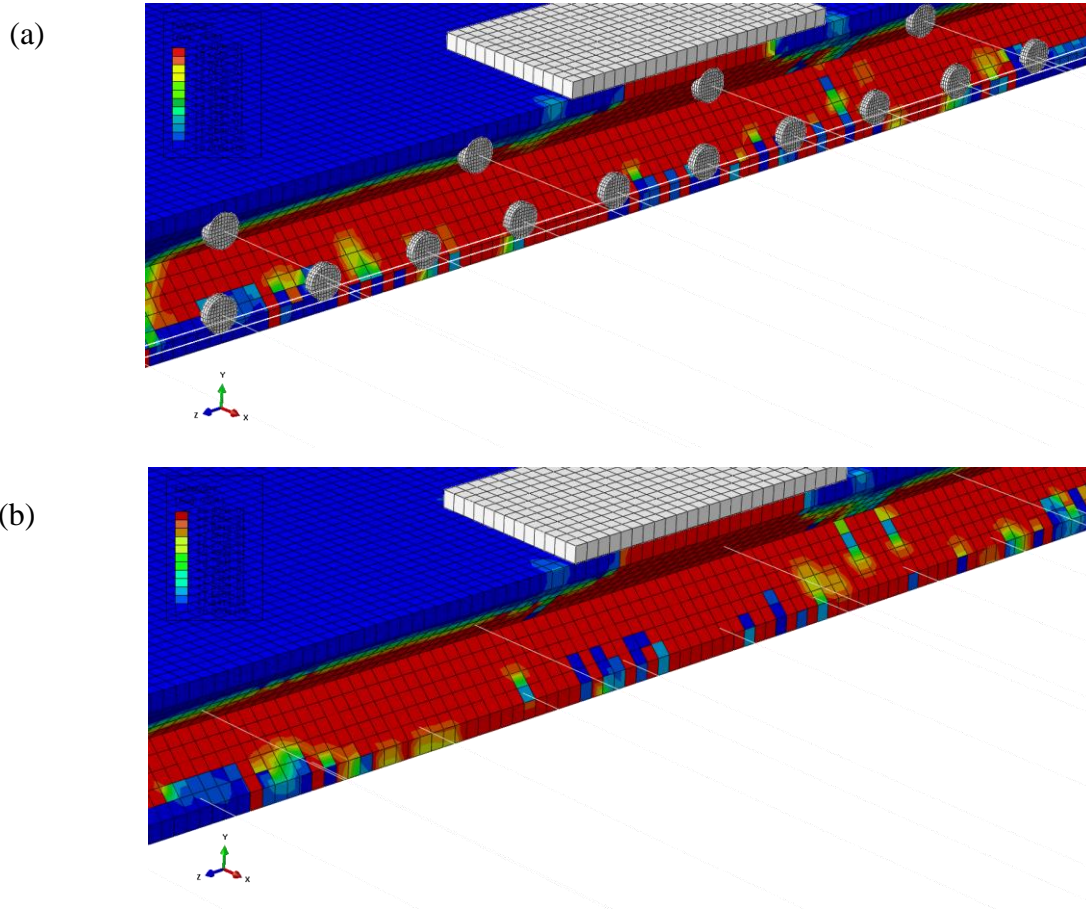


Figure 1.14: Damage in tension around (a) headed bar (b) straight bar

The axial strain history of normal precast concrete and the UHPC in panel 8H for both compression and tension is shown in Figure 1.15. The ultimate axial compressive strain was found 0.01 mm/mm and 0.0065 mm/mm for normal concrete and UHPC, respectively. As UHPC can withstand more tensile strain, it was observed that the tensile strain is higher in UHPC which is 0.08 mm/mm.

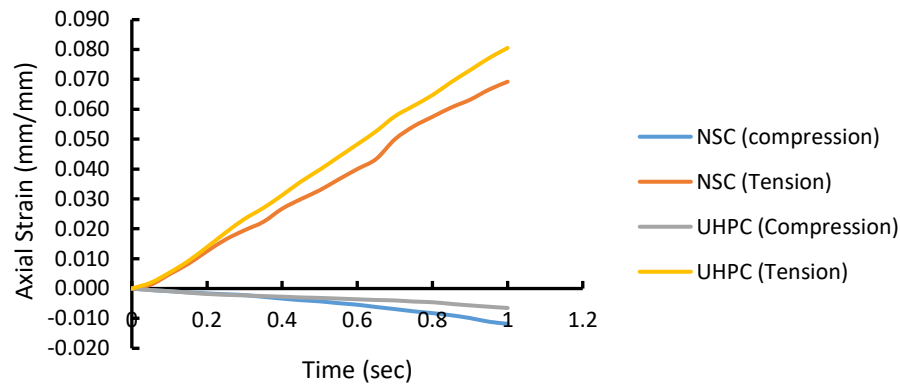


Figure 1.15: Strain response of NSC and UHPC in compression and tension (8H)

The overall comparison between the FEM and experimental results is summarized in Table 1.6. The energy absorption was calculated for each case (A_{FEM}) and compared with the respective experimental results (A_{exp}). The ratio between the energy absorption in the experiments to the energy absorption in the FEM ranges from 0.91 to 1.01. Table 1.6 also shows that the FEM considering the bilinear steel properties with a friction interface between the panel and the UHPC connection predicts more close results than other parameters.

Table 1.6: Comparison between FEM and Experimental results

Sensitivity Test	Variables	Straight bar	A_{exp}/A_{FEM}	Ultimate Load (kN)	Headed bar	A_{exp}/A_{FEM}	Ultimate Load (kN)
Mesh size	20mm	SB-H20T-E35°	0.95	486.98	HB-H20T-E35°	0.92	469.81
	10 mm	SB-H10T-E35°	0.95	445.21	HB-H10T-E35°	N/A	N/A
	5mm	SB-H5T-E35°	0.94	490.31	HB-H5T-E35°	N/A	N/A
Dilation angle (ϕ)	20	SB-S20T-E20°	0.93	453.17	HB-S20T-E20°	1.01	442.33
	35	SB-S20T-E35°	0.94	473.76	HB-S20T-E35°	0.91	467.13
	40	SB-S20T-E40°	0.93	488.54	HB-S20T-E40°	0.98	480.21
Concrete Model	Hsu and Hsu (1994)	SB-H20T-E35°	0.95	486.98	HB-H20T-E35°	0.92	469.81
	Saenz (1964)	SB-S20T-E35°	0.94	473.76	HB-S20T-E35°	0.92	480.21
	Park & Paulay (1975)	SB-P20T-E35°	0.93	482.62	HB-P20T-E35°	0.92	486.07
Steel properties	Elastic-Perfectly Plastic	SB-H20T-E35°	0.95	486.98	HB-H20T-E35°	0.91	469.81
	Bilinear	SB-H20T-B35°	0.94	515.74	HB-H20T-B35°	0.97	465.59
Contact Modeling	Perfect bond (Tie)	SB-P20T-E35°	0.93	482.62	HB-P20T-E35°	0.92	486.07
	Penalty (Friction)	SB-P20F-E35°	0.95	462.05	HB-P20F-E35°	1.01	462.02

Structural Performance under Low Cyclic Loading

The following section describes the behavior of the hybrid bridge deck connections under low cyclic loads.

All specimens were subjected to a low cyclic loading which is shown in Figure 1.16. The load was applied at the mid-span in two different locations. To minimize the computational effort, the whole model is scaled down to 457 mm x 200 mm x 2400 mm long as a strip slab. The total time for load application was 7 seconds (s). Four beams with a UHPC connection in

the middle were simulated and named UC-I-H, UC-M-S, UC-I-H and UC-I-S where, UC stands for UHPC connected beam, I and M represent interface and middle of the interface, respectively as shown in Figure 1.17. H and S are for headed bars and straight bars which represent the type of steel connection.

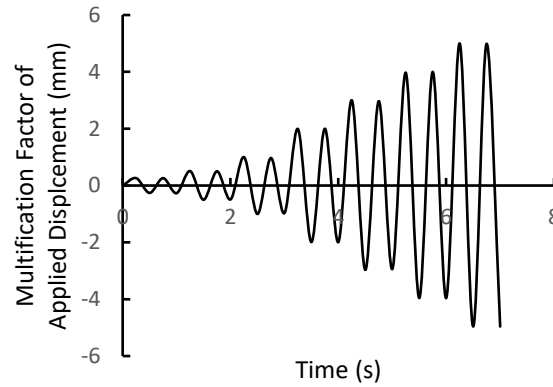


Figure 1.16 Displacement-time history

The location of applied load is shown in Figure 1.17 (a) and (b)

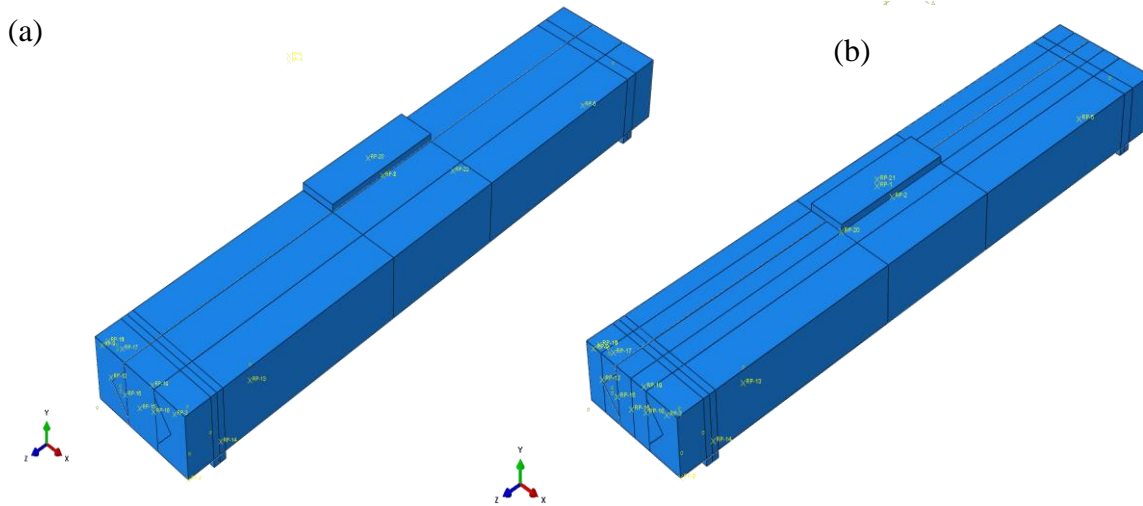


Figure 1.17: Location of load application (a) at the interface (b) middle of interface and UHPC connection

Load-deformation response

The load-deflection response of each beam is presented in Figures 1.18 (a), (b), (c) and (d),. It can be shown from Fig. 1.18 that the beam having headed bars experiences more deflection

than the beam reinforced with straight bars under the same cyclic load. The ultimate load carrying capacity and deflection of the specimens in the tension cycle were mostly dependent on the bond resistance and slip response of the spliced bars. For this reason, the shape of the load-deflection response in the tension cycle for all specimens were intrinsically similar for all cases. However, the beams with loading placed at the interface are stiffer than the beams with mid span loading. Ultra-high-performance concrete has a discontinuous pore structure that significantly enhancing stiffness as compared to conventional and high-performance concretes which increases its resistance towards the applied load. The ultimate loads under both tension and compression for all cases are summarized in Table 1.7. Table 1.7 also confirms that for a specific steel type, the slab can withstand 14.45% to 16.29% more load under compression and 2.4% to 30.38% more load under tension when load is applied in the middle of the connection.

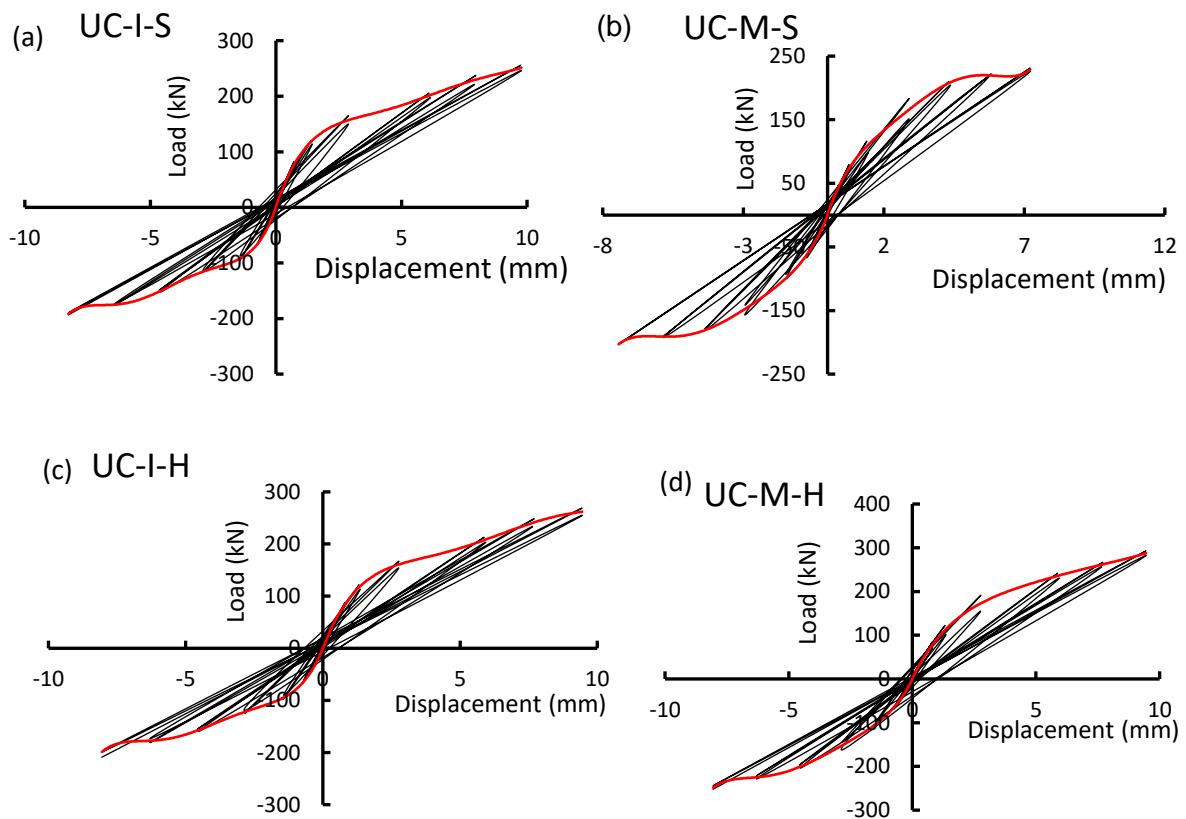


Figure 1.18: Load-deformation response (a) UC-I-S (b) UC-M-S (c) UC-I-H (d) UC-M-H

The failure envelope curve of the loading cycles for UC-I-S is shown in Figure 1.19. Three straight lines were developed joining the four distinct points where stiffness changed

significantly. The points were labelled as A-D (Kim and LaFave 2007) in both the compression and tension sides. The first change in stiffness indicates the initiation of cracking in concrete which was identified as point A and point B is associated with the initial yielding of steel. The maximum capacity is designated as point C whereas, point D corresponds to the final deformation at failure. The positive and negative values of displacement for all four beams are listed in Table 1.7. The ratio between the final deformation and the displacement after initial yielding was calculated to get the ductility indices of these beams which is reported in Table 1.7 as well. It is evident from Table 1.7 that all cases with headed bars experienced 10.12%-30.70% more ductility than the straight bar connections and for a specific type of connection, loading in the middle of interface has higher ductility value which ranges from 24.62% to 71.63%.

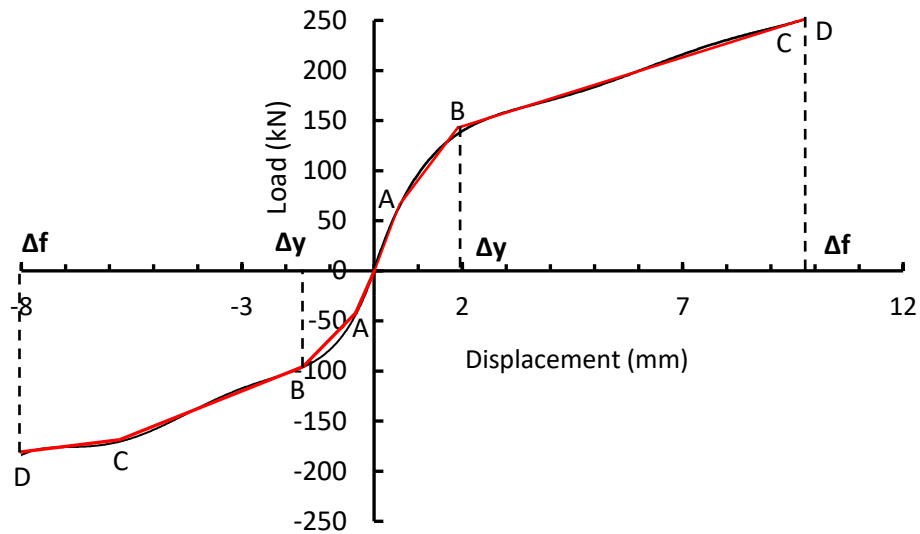


Figure 1.19: Envelope curve of loading cycles

Table 1.7: Displacement and ductility ratio

Designation	Positive Displacement (mm)		Negative Displacement (mm)		Positive Ductility ratio	Negative Ductility Ratio	Ultimate load under compression (kN)	Ultimate load under tension (kN)
	Δy	Δf	Δy	Δf	$\Delta f / \Delta y$	$\Delta f / \Delta y$	F_c	F_t
UC-I-S	2.30	9.74	1.55	8.27	4.23	5.33	231.18	203.91
UC-M-S	1.30	7.20	1.15	7.44	5.53	6.46	268.86	208.96
UC-I-H	1.30	9.44	1.10	8.05	7.26	7.31	255.67	193.42
UC-M-H	1.10	9.44	1.00	8.05	8.58	8.05	292.62	252.19

Axial strain response of reinforcing steel

Figure 1.20 represents the axial strain time history of steel reinforcements for the simulated beams. For all cases, the steel started to yield at 125-165 kN after 3.5s of load application. It is observed from Figure 1.20 that the straight and headed bars experienced 69% and 180.59% more strain respectively when load is applied at the middle of interface and UHPC connection. However, for a specific location of applied load, the straight bars undergo less strain (10.67%-46.14%) than the headed bars.

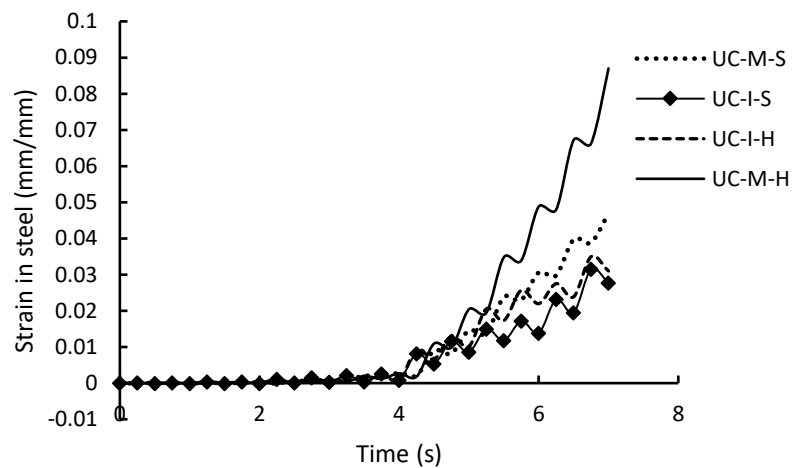


Figure 1.20: Axial Strain time history of steel reinforcement

Failure of the specimens

Figures 1.21 (a) to (d) represent the damage patterns in concrete after low cyclic loading in tension. The damage in normal concrete and UHPC connection at the interface loading having headed and straight bars are shown in Figure 1.21 (a) and Figure 1.21 (b), respectively. It is evident from Figure 1.21 (a) and Figure 1.21 (b) that the concrete underneath the loading plate is completely damaged although the UHPC connection experienced less damage. Figure 1.21 (c) and Figure 1.21 (d) illustrate the damage for midspan loading for both straight and headed bars. For midspan loading, the UHPC connection did not endure any damage. However, the normal concrete panels are almost fully damaged.

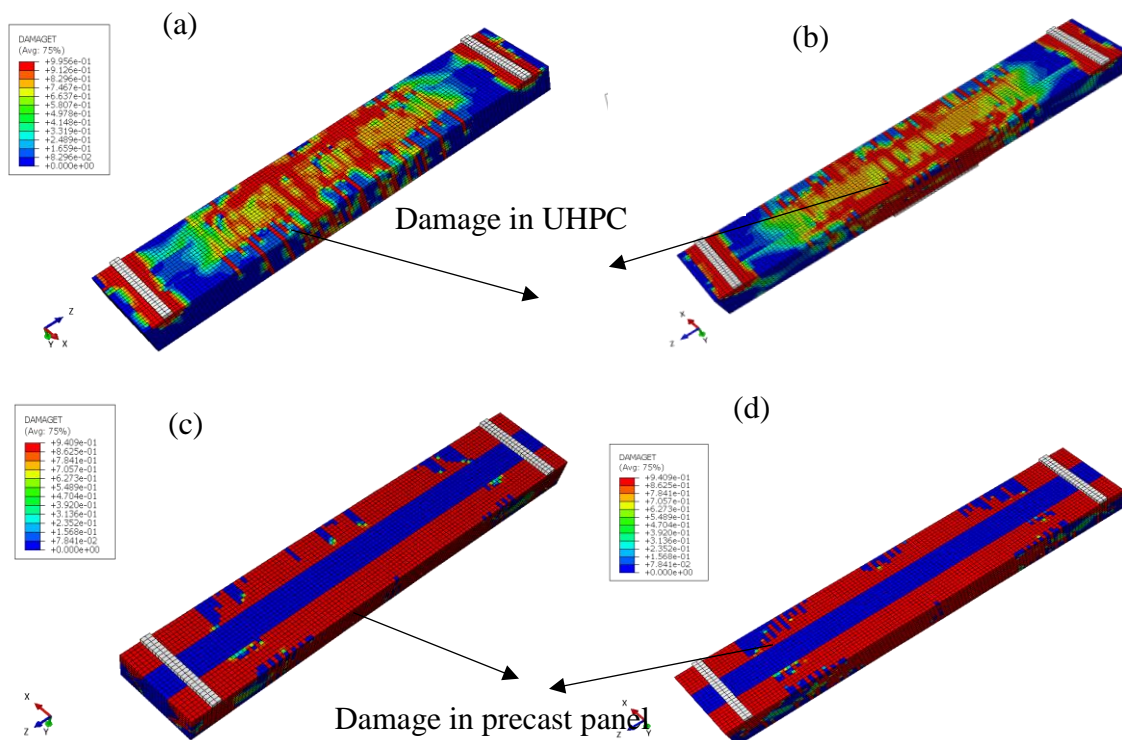


Figure 1.21: Concrete damage in tension (a) Loading at interface with headed bar (b) Loading at interface with straight bar (c) Loading at the middle of interface and UHPC with headed bar (d) Loading at the middle of interface and UHPC with straight bar

Conclusions

This study presents a sensitivity analysis based on numerical simulations of the behavior of UHPC bridge deck connections under monotonic and low cyclic loading. The software package ABAQUS was used to perform all the simulations. Various key parameters were investigated such as the concrete constitutive models for the normal concrete, steel stress strain behavior, mesh size, contact properties and concrete dilation angles with the following conclusions were drawn:

- The damage in concrete under monotonic loading is higher in normal concrete than UHPC with no signs of de-bonding between the two materials.
- The FE model captured the damage pattern of the composite slab deck quite satisfactorily.
- The numerical model is well capable of predicting the load displacement response though it experiences higher stiffness initially.
- Changing the dilation angle from 20° to 40° results in an increase of 7.81% in ultimate load for the panel with straight reinforcing bars, whereas for panel with headed bars, the increase in the ultimate load was found 8.56 %.
- The panel with straight reinforcement bars higher dilation angle produced slightly higher initial stiffness. In case of headed bar specimens, the stiffness of the composite panel for a dilation angle of 40° was found 9.69% greater than the stiffness found for dilation angle 20° , whereas for the straight bar panel, 5.47% higher value of initial stiffness was found for 40° dilation angle.
- The initial stiffness decreased 8% and 20% for panel with straight bars and panels with headed bars, respectively which justifies that the bilinear model could predict the overall panel performance closely to the experimental results.
- The energy absorption ratios of all the experimental results compared to the developed FEM models were in the range of 89% to 110%, which indicates that the FEM models are in good agreement with the experimental results.

- Under low cyclic loading, the headed bar connection experienced higher ductility ranging from 10.12% to 30.70% in all loading condition which is crucial for ensuring safe structural performance.
- The connection can withstand 14.45% to 16.29% more load under compression and 2.4% to 30.38% more load under tension when load is applied in the middle of the connection.
- No damage was found on UHPC connection when load is applied between the interface and UHPC connection due to its high resistance towards the applied load.
- To predict the structural response more accurately, further experimental works should be conducted.

References

- Aarup, B., and B. Jensen (1998). Bond Properties of High Strength Fiber Reinforced Concrete. Bond and Development of Reinforcement ACI Publication SP-180 pp. 459-472.
- Aarup, B., J. Karlsen, and G. Lindström (2009). Fiber Reinforced High Performance Concrete for In-Situ Cast Joints. Proceedings PCI/FHWA/FIB International Symposium on High Performance Concrete Orlando Florida. pp 9.
- ABAQUS Theory Manual, ABAQUS Inc., USA, 2016.
- Birtel, V. & Mark, P. (2006). Parameterised Finite Element Modelling of RC Beam Shear Failure. ABAQUS Users' Conference: 95–108.
- Bhide, S., Material Usage and Condition of Existing Bridges in the US, PCA, Skokie, Illinois USA, 2008.
- Broo, H., and M. Broo, (1997). Fog av högpresterande fiberbetong i prefabricerad brobanaplatta. examensarbete 97:2, Chalmers Tekniska Högskola, avd. för Betongbyggnad. (in Swedish, "Joint of High Performance Fiber Reinforced Concrete in Precast Bridge Slabs.
- Chen, L, Graybeal, B. (2012). Modeling Structural Performance of Ultrahigh Performance Concrete I Girders - J. Bridge Eng.
- El-Hacha, R., and Chen, D. (2012). Behavior of hybrid FRP–UHPC beams subjected to static flexural loading. *Composites Part B: Engineering*, 43(2): 582–593.
- Graybeal, B (2010). Behavior of Field-Cast Ultra-High-Performance Concrete Bridge Deck Connections Under Cyclic and Static Structural Loading. Federal Highway Administration, Report No. FHWA-HRT-11-023, November 2010, 186 pp.
- Graybeal, B. (2006a). Material property characterization of ultra-high-performance concrete. Rep. FHWA-HRT-06-103, Federal Highway Administration, Washington, DC.
- Graybeal, B. (2006b). Structural behavior of ultra-high-performance concrete prestressed I-girders. Rep. FHWA-HRT-06-115, Federal Highway Administration, Washington, DC.
- Graybeal, B. (2008). Flexural performance of an ultrahigh-performance concrete I-girder. *J. Bridge Eng.*, 13(6), 602–610.

Graybeal, B. (2009a). Structural behavior of a prototype ultra-high performance concrete pi-girder. NTIS Accession No. PB2009-115495, Federal Highway Administration, Washington, DC.

Graybeal, B. (2009b). Structural behavior of a 2nd generation ultra-high performance concrete pi-girder. NTIS Accession No. PB2009-115496, Federal Highway Administration, Washington, DC.

Graybeal, B.A., and Swenty, M. (2012). UHPFRC for prefabricated bridge component connections. In Proceedings of the Third International Symposium on Ultra High Performance Concrete, Kassel, Germany, #1223

Harryson, P. (1999). Bøjprovning av fog i högpresterande fiberbetong för prefabricerade brobanepplattor, statisk belastning,” rapport 99:1, Chalmers Tekniska Högskola, avd. för Betongbyggnad. (in Swedish). “Bending Test of Joint in High Performance Fiber Reinforced Concrete for Precast Bridge Slabs, Static Loading”.

Harryson, P. (2000). Utmattningprovning av fog i högpresterande fiberbetong för prefabricerade brobanepplattor,” rapport 00:2, Chalmers Tekniska Högskola, avd. för Betongbyggnad. (in Swedish, “Fatigue Test of Joint in High Performance Fiber Reinforced Concrete for Precast Bridge Slabs”)

Hsu, L.S., & Hsu, C.-T.T. (1994). Complete stress-strain behavior of high-strength concrete under compression. Magazine of Concrete Research, 46(169), 301-312.

Hussein, H. H., Walsh, K.K., Sargand, S.M., Steinberg, E. P.(2016), Interfacial Properties of Ultrahigh-Performance Concrete and High-Strength Concrete Bridge Connections. J. Mater. Civ. Eng., 2016, 28(5).

Lee, J. and Fenves, G. (1998). Plastic-Damage Model for Cyclic Loading of Concrete Structures. Journal of Engineering Mechanics, 124(8):892-900.

Lublinter, J., Oliver, J., Oller, S. and Oñate, E. (1989). A Plastic-Damage Model for Concrete. International Journal of Solids and Structures, 25(3): 299–326.

Nielsen, C., J. Olesen, and B. Aarup. (1996). Effects of Fibers on the Bond Strength of High Strength Concrete. BHP96 Fourth International Symposium on Utilization of High Strength/High-Performance Concrete, May 1996, Paris, France.

Perry, V., and Seibert, P. (2012). Field cast UHPC connections for precast bridge elements and systems. In Proceedings of the Third International Symposium on Ultra High Performance Concrete, Kassel, Germany, #1225.

R. Park, T. Paulay. (1975). Reinforced Concrete Structure, Wiley, Canada

Saenz LP (1964). Discussion of "equation for the stress-strain curve of concrete" by Desayi and Krishnan. *ACI J.*, 61(9): 1229-1235.

Schäfers, M., and Seim, W. (2011). Investigation on bonding between timber and ultra-high-performance concrete. *Construction and Building Materials*, 25(7): 3078–3088.
doi:10.1016/j.conbuildmat.2010.12.060

Chapter 2: Flexural Response of UHPC Bridge Deck Connections Made with Idaho Local Materials

Abstract

In recent years, the use of Ultra-High-Performance Concrete (UHPC) as a bridge joints closure material has increased significantly. Some state DOTs and Federal Highway Administration (FHWA) have successfully implemented UHPC in bridge deck connections. Despite of having excellent mechanical and material properties, Ultra-High-Performance Fiber Reinforced Concrete (UHPFRC) is not widely used due to its high cost and lack of widely accepted design guidelines. This study aims to develop a UHPC mixture using locally and domestically available materials without heat curing in hopes for reducing the production cost. Several trial mixtures of UHPC have been developed using locally available basalt and domestically available steel fibers. Among them, one trial mixture of 20.35 ksi compressive strength was selected for further study. Two full scale 8-ft. span hybrid bridge deck slabs with UHPC closure pour were constructed and tested under monotonic loading to identify the structural and material responses. The load- deflection response of the hybrid connection confirms that the deflection increased linearly until the initiation of cracks; after that it increased non-linearly up to the failure of the connection. The strain response also confirms that UHPC experiences less strain than normal strength concrete under compression. In addition, a moment-curvature analytical graphical user interface model of hybrid bridge deck connection has been developed using MATLAB to predict ductility, curvature, and the stress distributions in those connections. The predicted value of moment and curvature from the code was found in good agreement with experimental data.

Keywords: UHPC, Local materials, flexural response, analytical model, moment-curvature.

Introduction

During the past four decades, researchers all over the world have conducted numerous studies on high performance concrete which can significantly reduce construction time, maintenance cost as well enhance durability and exhibit high toughness. State, regional and municipal bridge engineers are always in search of new ways to build better bridges, reduce travel time and reduce maintenance cost as, most often, they need to replace critical bridge components within a limited time period or overnight road closure. In 1993, Richard et al.

(1994) developed a high strength reactive powder concrete (compressive strength over 150 MPa) consisting high binder content, very low water/cement ratio, silica fume, fine quartz powder, superplasticizer, and fibers. This incredible concrete exhibited very impressive mechanical properties, ductility, and toughness and eventually termed as “Ultra-High-Performance Concrete (UHPC)” by De Larrard and Sedran (1994) in the following year. Although UHPC can produce very high compressive strength but the production of UHPC often needs high curing temperature (90°C or above), vacuum mixing, and pressure before and during setting which can result in low production efficiency and high energy absorption. Therefore, additional research has been conducted on developing UHPC with conventional mixing procedures, low cost materials, and common curing (Reda and Shrive, 1999; Yunsheng et al. 2008). So far, UHPC has been used in Europe, North America, Australia, Asia and New Zealand (Rebentrost & Wight, 2008; Schimidt & Fehling, 2005; Graybeal, B. 2008).

The U.S. Federal Highway Administration (FHWA) has been conducting research on the utilization of UHPC for the highway infrastructure since 2001 and has been working with state Departments of Transportation to implement this new technology for accelerated bridge construction since 2002 (Graybeal, B. 2008).

Now a days, lots of efforts are being implemented to produce low cost UHPC by eliminating expensive materials i.e. ground quartz, accelerator. Also curing conditions plays an important role in achieving high compressive strength. It is reported in FHWA website that heat curing can increase the compressive strength of UHPC by 53% with respect to untreated specimens. But it is not always feasible to ensure heat curing in the field. This study aims to develop a low cost UHPC using local materials without heat curing and evaluate the performance of the developed UHPC mix in bridge connections.

In addition, a moment curvature analytical model of hybrid bridge deck connection has been developed using MATLAB code. The goal is to provide a tool to professional engineers to predict ductility, curvature, and the stress distributions in those connections. The code is built to allow input parameters such as concrete strength, dimensions of hybrid connection and deck panels, reinforcement configuration and shape of the connection. The code is verified

for the full UHPC beam, and UHPC hybrid connection. Furthermore, the code is also verified for normal strength reinforced concrete beam using the Whitney stress block for concrete design along with an elastic-perfectly plastic steel behavior. Material nonlinearity for both normal strength concrete and UHPC were considered in the code.

Theoretical Concepts of UHPC Production

UHPC is a fine-grained concrete with a very dense and homogeneous cement matrix which prevents the development of microcracks within the structure. The fundamental concepts of producing UHPC include reduction in porosity, improvement in microstructure, enhancement in homogeneity, and increase in toughness.

Reduction in Porosity

Porosity plays an important role in predicting the strength of cement-based materials. Many studies showed that the compressive strength of a mix can be achieved predicted from its total porosity. Although pore size distribution, shape and position of pores influence the strength development, it is quite difficult as well as impractical to include these parameters in the compressive strength prediction. Very few relationships involving strength and porosity of cement-based material have been reported so far (Li & Aubertin, 2004). Balshin (1949) conducted research on the effect of porosity on tensile strength of ceramics and proposed the following relation:

$$\sigma = \sigma_0 (1 - P)^b \quad (2.1)$$

where σ is the strength, σ_0 is the strength at zero porosity, P is the porosity, and b is an empirical constant. The study conducted by Ryshkewitch (1953) on the compressive strength of Al_2O_3 and ZrO_2 proposed the equation:

$$\sigma = \sigma_0 e^{-kp} \quad (2.2)$$

where k is the empirical constant.

Based on the study of set sulfate plasters, Schiller (1971) proposed the relation:

$$\sigma = n \ln \frac{P_0}{P} \quad (2.3)$$

where n is an empirical constant, and P_0 is the porosity at zero strength. Hasselman (1969) conducted an extensive study on developing a linear relationship between strength and porosity for different refractory materials and suggested the equation:

$$\sigma = \sigma_0 - cP \quad (2.4)$$

where c is an empirical constant.

All these equations confirm that the strength is dependent on porosity and the low porosity results in higher strength.

The porosity and the pore size distribution can be improved by using superplasticizer, reactive admixtures and close packing raw materials. Low initial porosity can be achieved by applying close packing models for the proportion of cement, silica fume, quartz powder, superplasticizer etc. The use of superplasticizer can significantly reduce water-to-binder (w/b) ratio for a given workability. Typical water-to-binder ratio (w/b) for UHPC ranges between 0.14 and 0.20 whereas in conventional concrete it ranges from 0.4–0.5. For producing high quality UHPC, it is important to select a superplasticizer efficiently to produce high quality UHPC.

Improvement of Microstructure

UHPC is a very dense material and its uniform microstructure is achieved through close packing of solid materials, facilitating hydration and pozzolanic reactions, and improving the interfacial transition zone between aggregates and cementitious products. The internal microstructure of UHPC is mainly comprised of un-hydrated cement clinker particles, quartz sand, and hydration products, such as C–S–H. Low w/b ensure low porosity which eventually decrease the space available for the growth of calcium hydroxide (CH) crystals. The hydration of cement and the pozzolanic effects of mineral admixtures are accelerated by using elevated temperature curing which consumes most of the CH crystals and converts them to C–S–H. There are almost no pores observed in the nano-porous range with pore sizes up to 100 nm, and no significant CH was detected by X-ray diffraction (XRD) (Reda and Shrive, 1999). Ensuring homogenous microstructure is very important for the performance of UHPC. Ultra-high-performance concrete virtually has no capillary pores and is almost impervious to liquid and gases, ensuring zero corrosion. It can also serve as the wearing

surface for bridge decks without any additional protection against chlorides, alkalis and de-icing salts.

Enhancement in Homogeneity

Homogeneity of aggregates is ensured in UHPC by eliminating coarse aggregate and using fine raw materials. In conventional concrete, coarse aggregates act like skeleton as they have higher hardness than cement paste. Cracks in concrete are proportional to the size of the aggregates. Therefore, the use of quartz sand instead of coarse aggregate can significantly decrease the size of microcracks. Moreover, the reduction in aggregate size decreases the inhomogeneity in concrete by reducing the probability of its own defect.

Increase in Toughness

Toughness of a material is a measure of its energy absorption capacity and characterized by its ability to resist fracture. Incorporation of fibers in concrete can enhance its toughness and control crack initiation and propagation. The presence of fibers in UHPC not only increases its toughness but also increases its impact resistance. The most common types of fibers used in UHPC are steel and carbon. UHPC specimens incorporating glass fibers and polypropylene fibers showed lower strength than UHPC consisting steel fibers (Yang, 2008).

Development of UHPC with Local Materials

The material constituents of UHPC are not completely different from those of conventional concrete. However, additional materials i.e. silica fume, silica powder, fine aggregate, HRWRA, steel fibers are used to achieve high strength in UHPC. The proportion of the material constituents in UHPC are determined based on optimization of granular mixture. In North America, some companies produce the premix for UHPC. Among them, the patented product of a major worldwide concrete manufacturer under the name Ductal is commonly used (Graybeal, 2006). Willie et al. (2011) provided the following general recommendations for producing UHPC commercially.

- Cement with a moderate fineness and C_3A content significantly lower than 8 percent.
- Sand-to-cement ratio of 1.4 for a maximum grain size of 0.8 mm (0.03 inches).
- Silica fume with very low carbon content at 25 percent of the weight of cement.
- Glass powder with a median particle size of 67×10^{-6} inches (1.7 μm) at 25 percent of the weight of cement.

- High-range water-reducing admixture.
- Water-cement ratio of about 0.22.
- Steel fibers at 2.5 percent by volume.

It is observed from the mix proportions proposed by different researchers that for producing UHPC, it is important to keep water-cement ratio very low. Due to low water-cement ratio, some cement particles cannot participate in hydration process and remain un-hydrated. These un-hydrated particles work as aggregates in the mix. The workability of the UHPC can be improved by using HRWRA, thus ensuring self-compacting concrete to be produced. The largest particle used in UHPC mixture is found to be sand having a diameter of 150 micrometers (μm) to 600 micrometers (μm). The second largest particle is the cement having an average diameter of 15 μm , whether crushed quartz has almost same average diameter of 10 μm . The size of the silica fume should be small enough to fill the interstitial voids to ensure low porosity and low permeability. Generally, coarse aggregates are not used for UHPC mix to ensure homogeneity. Though, Collepardi et al. (1997) reported that no significant change occurred on the compressive strength of UHPC when small amount of coarse sand was incorporated in the mixture. Some researchers have tried to use coarse aggregates (such as crushing basalt, natural sand, and limestone) up to 12.7 mm as partially replacement of fine sand. However, the porosity increased with the increase of particle size resulting in a lower compressive strength as expected (Reda et al., 1999; Zhao et al., 2014; Wille and Boisvert-Cotulio, 2015; Liu et al, 2016; Sobuz et al., 2016). Dimensionally, the largest constituent of UHPC mix is the steel fiber. A volume of 2% is recommended by the commercial manufacturer Ductal to produce economical and workable UHPC mixtures (Graybeal, 2006; Richard and Cheyrezy, 1995). It is reported by Habel et al. (2008) that self-compacting UHPC mix can be produced for precast application and Cast-in-Place applications. Kazemi and Lubell (2012) further improved this mix design without requiring heat curing and pressure.

The possibility of using metakaolin, pulverized fly ash, limestone micro filler, siliceous micro filler, micronized phonolith, or rice husk ash as a replacement of silica fume was investigated by Rougeau and Borys (2004). Coppola et al. reported that using acrylic

polymer admixtures resulted in higher compressive strengths compared with naphthalene and melamine admixtures.

To get the desired compressive strength, nine different mix designs are implemented and a compressive strength of 20.35 ksi is achieved without heat curing.

Material Constituents

Portland cement Type I-II with a specific gravity of 3.15 was used in this study for preparing UHPC samples. The cement was generously donated by Premix Inc., Pullman, WA.

Commercially available densified powder silica fume “Sikacrete 950DP” was used as a partial replacement of cement for improving the mechanical properties and durability of UHPC.

Local natural sand was provided by Premix Inc and basalt was provided by Poe Asphalt Paving Inc. The fine aggregate was washed to remove the clay/silt particles and then oven-dried at 110°C (230°F) to achieve zero moisture content. The materials were sieved according to ASTM C136 (2014). Table 2.1 presents the grain size distribution of the fine sand and basalt from sieve analysis. The sample sieved materials are presented in Figure 2.1. According to ASTM C128 (2015), the specific gravity and water absorption of the fine sand were 2.60 and 2.6% respectively.

Table 2.1: Grain Size Distribution of Fine Aggregate

Fine Aggregate		
Sieves	Individual % Retained	Cumulative % passing
#30	0	100
#50	71	29
#100	22.7	6.3
#200	6.3	0



Figure 2.1. Sample Sieved Materials

Steel fibers (NYCON-SF Type I, Figure 2.2) were added in the UHPC at 2 percent by volume to increase durability and toughness. The physical properties of steel fiber are presented in Table 2.2, which meets the requirements of ASTM A820 (2015).

Table 2.2: Physical properties of steel fiber

	Steel fiber
Fiber Length, in. (mm)	0.5 (13)
Filament Diameter, in. (mm)	0.008 (0.2)
Specific Gravity	7.8
Aspect Ratio	65
Tensile strength, ksi (MPa)	400 (2,660)
Flexural strength, ksi (GPa)	29,000 (203)
Melting Point, °F (°C)	2760 (1516)
Color	Copper
Water Absorption	Nil
Alkali Resistance	High
Corrosion Resistance	High



Figure 2.2. Steel Fibers

Mix Designs

Nine trial mixtures of UHPC were carried out at the BEL concrete laboratory with varying water-cementitious materials (w/cm) ratios, amounts of silica fume, cement, HRWRA, and fine aggregates. A horizontal mixer of one (1) cubic feet capacity (Figure 2.3) was used to mix the concrete. Primarily based on the flowability and the 28-day compressive strength, one mixture proportion of UHPC (M9) was selected. The compressive strength of M9 was found 20.35 ksi at 28 days. The corresponding water to cementitious materials ratios (w/cm) of mix design M9 was 0.21.



Figure 2.3. Horizontal Concrete Mixture

Generally, mixing time required for UHPC is relatively longer than that of conventional concrete due to absence of coarse aggregate and low w/cm ratio. The mixing time also depends on the power of the mixer (Russel and Graybeal, 2013). In this study, the whole mixing time

of the horizontal mixer ranged 30-40 minutes and completed according to the following four stages:

1. Dry constituents were mixed for 4-5 minutes.
2. Then 75% of the water was added and mixed for 6-7 minutes
3. Later, HRWRA was added with the remaining 25% of water and mixed for 8-10 minutes
4. Finally, steel fibers were added with the mixture, and the mixing was continued for 8-10 minutes till thorough.

After completing the mixing, the fresh UHPC was poured into oiled steel molds according to ASTM C192 (2016). UHPC was poured in three layers and manually vibrated with 25 blows by tamping rod. After approximately 24 hours, specimens were demolded and placed for curing. The curing of UHPC specimens was conducted in two phases: initial curing after casting and standard curing prior to testing. All specimens in the molds were cured in a humid room with temperature 73.5 ± 3.5 °F (23.0 ± 2.0 °C) from the time of casting to prevent the moisture loss. After 24 ± 4 hours, all specimens were then demolded and soaked in lime-saturated water until testing age. Table 3.3 represents all the mixture proportions.

Table 2.3: Mixture proportions of UHPC

Mixture Type		Unit	M1	M2	M3	M4	M5	M6	M7	M8	M9
Type	I/II	Portland									
Cement		lb/yd ³	1146	1500	1500	1500	1500	1500	1500	1500	1500
Silica Fume		lb/yd ³	303	260	375	375	375	375	375	260	375
Glass Powder		lb/yd ³	0	0	0	0	375	375	0		
Fine Aggregate	Sand	lb/yd ³	1641	1574	1355	1297	2070	1980			
	Basalt	lb/yd ³							1297	1574	1355
Steel Fibers		lb/yd ³	0	236	240	267	0	225	267	236	240
HRWRA		gal/yd ³	6.5	10.5	6.25	6	7.00	7.25	6	11.5	7.25
Water		lb/yd ³	309	325	394	413	330	398	413	325	394
w/cm			0.21	0.18	0.21	0.22	0.22	0.21	0.22	0.18	0.21
Spread Testing		in.	7.0	9.00	8.75	8.00	7.75	8.25	8.25	8.75	8.50

Flow Table Test

The flow table test for hydraulic cement mortar is widely used to evaluate its rheology, as UHPC does not contain any coarse aggregate. After completing the mix, the flow test was conducted following the procedures of ASTM C1437 (2015, Figure 2.4). After lifting the flow mold away, the flow table was dropped 25 times in 15 seconds and the average diameter of flow was measured.



Figure 2.4. Flow Table Test (M9)

Compressive Strength Test

The compressive strength tests were conducted in accordance to ASTM C109 “Standard Test Method for Compressive Strength of Hydraulic Cement Mortars (Using 2 in. or [50-mm] Cube Specimens)” (2016) (Figure 2.5). All the compressive tests were conducted under a specific stress rate, 35 ± 7 psi/s. Therefore, the required loading rate was calculated corresponding to the size of the specimen, i.e., 8400 ± 1680 lbf/min, for 2-inch cubes (Figure 2.5). The compressive strength was measured at 7 days, 14 days, and 28 days to study age-dependent compressive behaviors. Three replicates were tested for all mix designs. A 28-day compressive strength of 20.35 ksi was achieved from mixture M9. The averaged test data for the compressive strength is shown in Table 2.4.

Table 2.4: Compressive strength of UHPC

Specimen	Age	M1	M2	M3	M4	M5	M6	M7	M8	M9
	7	7.85	8.53	8.85	5.6	7.1	9.3	7.5	9.54	9.96
2-inch cubes	14	9.78	10.26	10.86	8.8	9.5	11.5	9.1	11.19	12.91
	28	11.43	12.71	13.06	10.63	11.88	14.6	13.8	16.52	20.35

Considering the compressive strength, flowability as well as setting time, M9 was selected to conduct the future experimental program.



Figure 2.5. Cube Specimen

Figure 2.6 shows the stress-strain curve for M9 sample specimen. The ultimate compressive stress was found 20.35 ksi (140.30 MPa) and the modulus of elasticity was found nearly 8822.935 ksi (60.832 GPa). The graph indicates that the stress-strain response is almost linear until failure and UHPC undergoes brittle failure.

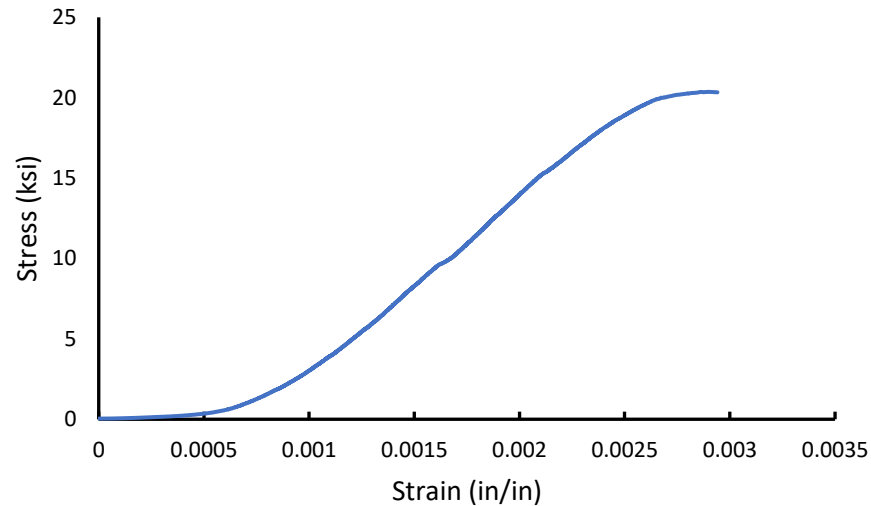


Figure 2.6. Stress-strain response of M9 mixture at 28 days

Flexural Response of UHPC Hybrid Bridge Deck Connection made with Local Material

The flexural behavior of a complete UHPC connected bridge deck is yet to be experimentally investigated. To examine the flexural response of locally made UHPC, two-8-ft. span hybrid bridge deck slabs with UHPC closure constructed in the department of civil engineering laboratory and were tested under monotonic loading to identify the structural and material responses. The members were designed to fit the roller supports and hydraulic actuator set up located in the Department of Civil and Environmental Engineering Laboratory (Structures). There are currently no ACI codes or design guides for testing UHPC connected bridge deck panels.

Reinforcement Details

From the literature review, the connection details developed by NYSDOT were used to develop the test specimens. Each specimen consists of two conventional concrete precast panels connected by a UHPC closure pour. Figure 2.7 presents the reinforcement details for specimen. The connection reinforcement consisted of straight, lapped 16M (#5) mild-steel reinforcement. The minimum lap length for the reinforcement in the connection was 150 mm (5.9 inch). Two additional 16M (#5) bars were provided along the length of the connection between the top and bottom layers. At the interface between the precast panel and the field-cast UHPC, this reinforcement configuration resulted in a 180 mm (7.1 inch) spacing of the

bottom mat of reinforcement. In the middle of the connection, the spacing between any two adjacent non-contact lap spliced bars was 90 mm (3.5 inch).

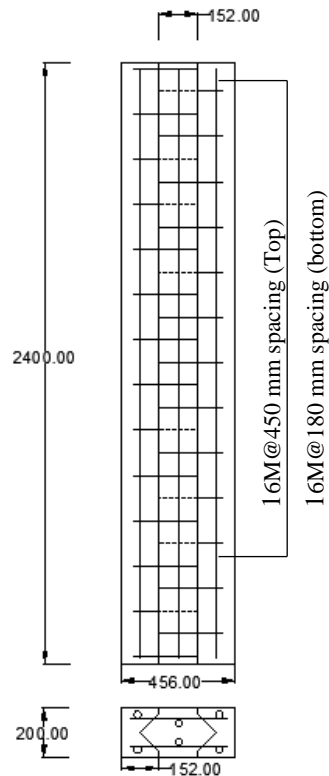


Figure 2.7. Reinforcement details

Construction of Specimens

The HSC deck panels were cast in the BEL structures laboratory using high strength concrete provided by Pre-Mix Concrete Incorporated located in Pullman, Washington. Figure 2.8 shows the Pre-Mix concrete truck in final mixing before pouring into the wheelbarrow. The wheelbarrow was hauled to the BEL lab for pouring concrete into forms. Wooden formworks were constructed according to the dimensions required for the specimens, with provision of the desired concrete cover, 1 inch, on all sides of the panels using plastic seats. Figure 2.9 provides the structural details of the wooden forms as well as the locations of the reinforcements throughout the panel.



Figure 2.8. Pre-Mix Concrete Plant unloading HSC from their truck outside BEL



Figure 2.9. Wooden forms before pouring concrete

Material Properties

High Strength Concrete

The high-strength concrete was donated by the Pre-Mix Concrete plant, with a target strength of 7 ksi. A total of 1.5 yard³ of HSC was provided for this experiment. Five 4-inch diameter by 8-inch height cylindrical samples and one 6-inch diameter by 12-inch height cylindrical sample were taken from the batch to conduct 28-day compressive strength test and modulus of elasticity tests according to ASTM standards. An average compressive strength of 6.7 ksi was achieved at 28 days. Table 2.5 shows the material quantities batched by Pre-Mix for this concrete mix. A water-to-cement ratio of 0.33 resulting in a 3-inch slump was achieved by this mix. Air-entrained, Daravair, was used as well as a water reducing agent, Daracem was used to maintain the strength while keeping the water-to-cement ratio low. To limit air voids, a concrete vibrator was used while pouring concrete into the form work. Figure 2.10 shows pouring concrete into wooden form works. The samples taken for 28-day compressive strength tests are shown in Figure 2.11.

Table 2.5: Concrete Mix Design

Materials	1 yd ³		1.5 yd ³	
	Design		Batched	
Coarse – ¾ "	1725	lb	2560	lb
Fine -Blend Sand	1450	lb	2260	lb
Cement (Type I-II)	846	lb	1260	lb
Daravair	3	oz	4.0	oz
Daracem	50	oz	75	oz
Water	33	gl	39.9	gl



Figure 2.10 Casting of precast panels



Figure 2.11. Samples for 28-day compressive strength test

The forms were removed after 24 hours when the concrete was set. As the reinforcement was extended from shear key face, removal of formwork from that side was difficult. Some forms needed to be removed by saw. Figure 2.12 shows the removal of forms with a reciprocating saw. All the precast panels were cured with water towels for 28 days.

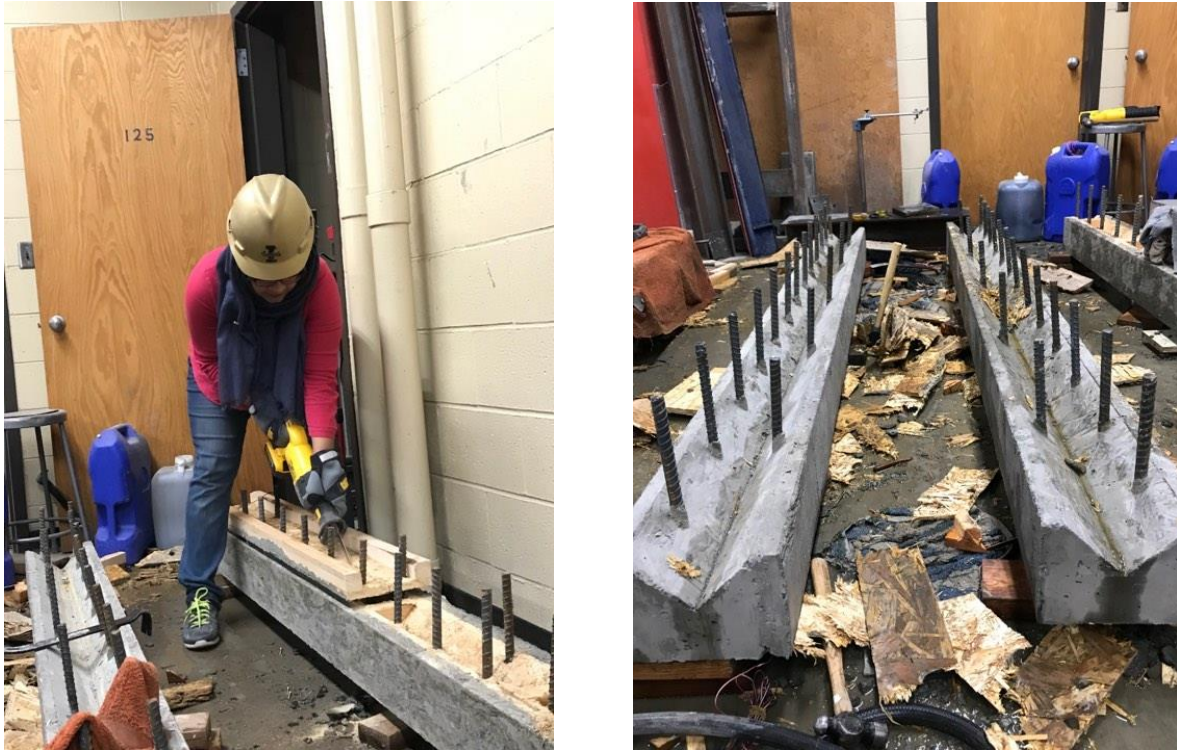


Figure 2.12 Removal of formworks

UHPC

Before starting concrete mixing, two precast panels were placed in formwork to ensure proper dimension of the hybrid connection. Two #5 rebars were attached longitudinally between top and bottom layers of the connection (Figure 2.13). For the two UHPC connections, a total of 10 cubic foot of UHPC was needed which include 500 lbs. of sieved basalt fine particles. Naturally available basalt is generally coarse in size. Tons of materials were sieved in the laboratory using big sieve shaker to produce 500 lbs. of #50 downgraded basalt particles, (Figure 2.14) which was not only time consuming but also labor intensive. Figure 2.14 (b) shows three 30-gallon buckets filled with sieved materials. All the required materials were weighed and placed in the laboratory before starting the mixing procedure. The concrete was mixed in two batches. The dry ingredients were poured first in the drum mixture and mixed for 4-5 minutes. Then 75% of the water was added. After mixing for 6-7 minutes, HRWRA was added with the remaining 25% of water and poured into the mixture. At last, steel fiber was added, and mixing was continued for 8-10 minutes till thorough. Figure 2.15 shows deck panels connected with UHPC pour. Table 2.6 shows the UHPC mix design.

Table 2.6: UHPC mix design

Materials	1 yd ³		10 ft ³	
	Design		Batched	
Cement (Type I-II)	1500	lb.	556	lb
Silica Fume	375	lb	140	lb
Basalt	1355	lb	500	lb
Steel Fiber	240	lb	88	lb
Water	393	lb	145	lb
HRWRA				
w/c	0.21		0.21	



Figure 2.13 Form work for UHPC connection



Figure 2.14 (a) Sieving procedure (b) Sieved materials (#50 passing and #100 retained)



Figure 2.15 Deck Panels after UHPC pour

Experimental Setup

The test setup available in the structural lab was utilized to simulate the loading and boundary conditions that occurs in bridges. Load was applied vertically at three points on the top surface of the test specimen by the actuator hanging from the top beam of a reaction frame. The load cell in this hydraulic actuator has a maximum capacity of 50,000 pounds. The test specimen was supported by fixed supports welded to the frame in both ends. The welded supports allow for a minimum of 7-foot clear span between two ends. Each beam was tested with a displacement-controlled loading rate of 1 mm/min. Figure 2.16 shows the experimental setup. All specimens were loaded with the same geometric configurations.

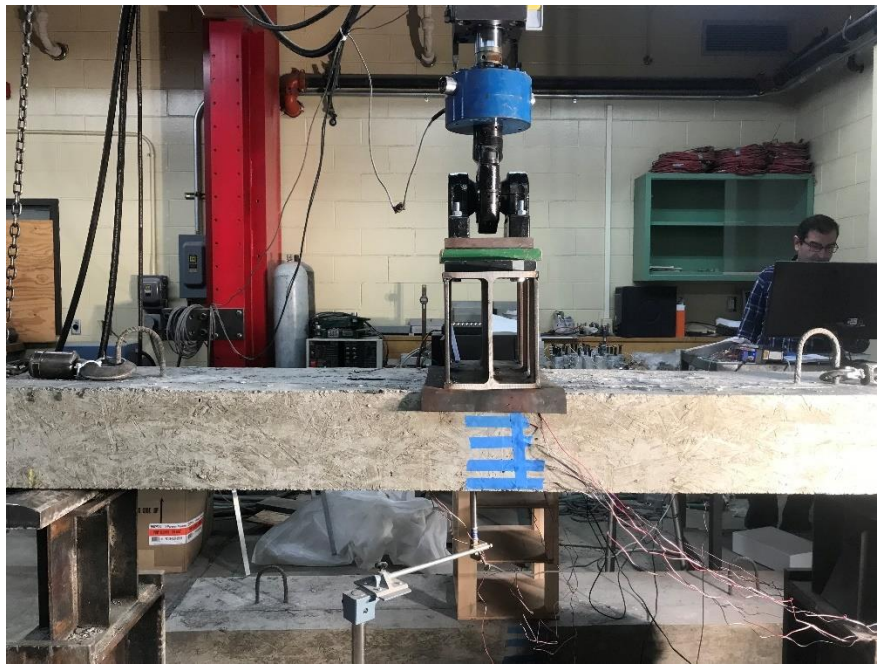


Figure 2.16. Test Set up

Instrumentation

All the specimens were designed to capture the necessary testing information required for the study. This information includes strains in concrete, steel and UHPC, mid-span displacement, and applied load. The instrumentation was completed in two stages. The first stage involved fixing the strain gauges to the reinforcement before placing concrete. The second stage was

completed by fixing the external equipment to the loaded specimens, such as the Linear Variable Differential Transformer (LVDT), as well as the concrete strain gauges placed externally on the hardened concrete at mid-span.

Strain Gauges

Stage One: Fixing Reinforcement Strain Gauges in the bottom bar and connection

In this stage of instrumentation, Micro-Measurements™ strain gauges of 350Ω electrical resistance capacity were attached to the mid-span of all bottom reinforcements used in the deck panels. The surface of the steel bars was cleaned with baking soda and vinegar and smoothed out to create a proper fixation surface for the strain gauge. They were glued to the surface using epoxy and then left 24 hours to cure. Next, self-fusing tape was used to protect the strain gauges from moisture and other potential distresses experienced from placing of the concrete. Strain conditioners were attached to all gauges to magnify the millivolt output of the gauge and the gauge factors were input into the data logger as specified by the manufacturer. Two more strain gauges were attached to the top and bottom bar of the longitudinal connection. Figure 2.17 shows the data logger used in the experiment.

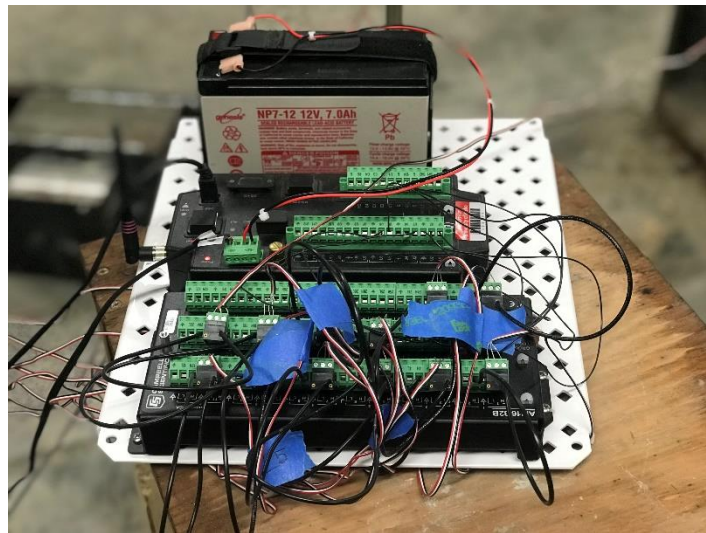


Figure 2.17. Campbell Scientific CR6 series data logger

Stage Two: Fixing of Concrete Strain Gauges and LVDT

In this stage, an LVDT, a 350-ohm strain gauge bridge to sense movable rod displacement, and concrete strain gauges were installed. The LVDT was used to monitor deflection of the specimen at the mid-span. The LVDT location can be seen in Figure 2.18.

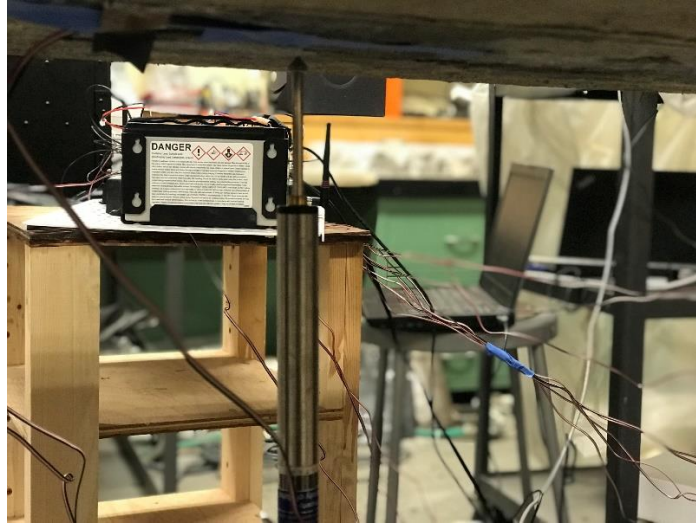


Figure 2.18. LVDT for recording midspan deflection (Underneath the beam)

Test Results and Discussion

Figure 2.19 shows the load deformation response of both UHPC hybrid bridge deck connections made with local materials. The deflection of the connection was measured with LVDT installed in the midspan and plotted against the load in Figure 2.19. The deflection increased linearly until the initiation of first crack, after that it increased non-linearly.

The initiation of cracks was indicated by micro cracks which were barely visible. As the test continued, more cracks were added between the existing cracks. However, Figure 2.20 (a) and (b) confirms that the cracks were not visually widened. The cracks were found to propagate from the lower tensile side to the upper face of the beam.

The initial cracking load was found nearly 15 kip (66 kN). For BC-1, an ultimate value of 29.87 kip (132.87 kN) with a deflection of 0.31 in. (7.84 mm) was achieved. For BC-2, an ultimate value of 29.20 kip (129.90 kN) with a deflection of 0.32 in. (8.14 mm) was achieved which confirms that the locally made UHPC performed well as a closure material in flexural resistance.

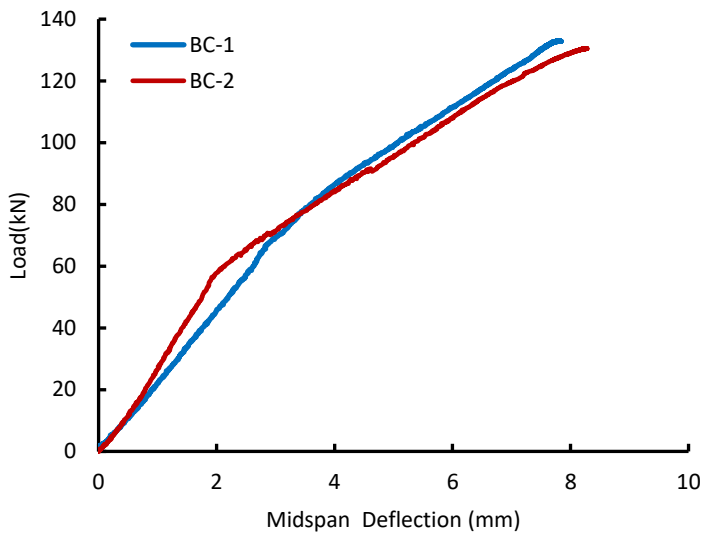


Figure 2.19. Load -Deflection Response for UHPC hybrid bridge connection made with Idaho local materials

Failure of the connection occurred due to propagation of tensile cracks at the bottom surface of the connection. The cracks were found propagating perpendicular to the interface as shown in Figure 2.20 (c) and (d). However, there was no indication of debonding between the UHPC and HSC interface. The cracks in the HPC could be identified by eye, though the cracks in the UHPC were not easily visible. Figure 2.20 (c) and (d) demonstrates that the crack patterns exhibited by the two types concrete were completely different.



(a)

(b)



Figure 2.20. (a) Crack pattern observed in flexure, BC-1 (b) Crack pattern observed in flexure, BC-2 (c) Cracks at the bottom surface of the hybrid connection, BC-1 (d) Cracks at the bottom surface of the hybrid connection, BC-2

Figure 2.21 (a) and (b) show the strain response measured by strain gauges at different layers of HSC and UHPC for BC-1 and BC-2 respectively. Five strain gauges were installed in the HSC surface from top fiber to bottom fiber. These strain gauges were named as layer 1 to layer 5. The negative strains correspond to compressive strains while positive strains represent tensile strains. In general, as the load was increased, compressive strains were developed in layers 1 and 2 and tensile strains were developed in layers 4 and 5. Layer 3 was positioned at the mid-height at the neutral axis. The strain in layer 3 changed from zero to positive value as the neutral axis shifted upward due crack propagation (Figure 2.21 a). In both cases, UHPC experienced less strain which is obvious as UHPC is stiffer than HSC. A maximum tensile strain of 0.00236 was experienced by UHPC while the maximum compressive strain was found 0.001086 for BC-1. Both compressive and tensile strain followed a linear pattern until it reached the peak. From Figure 2.21 it is evident that no rebar yielded during the test procedure.

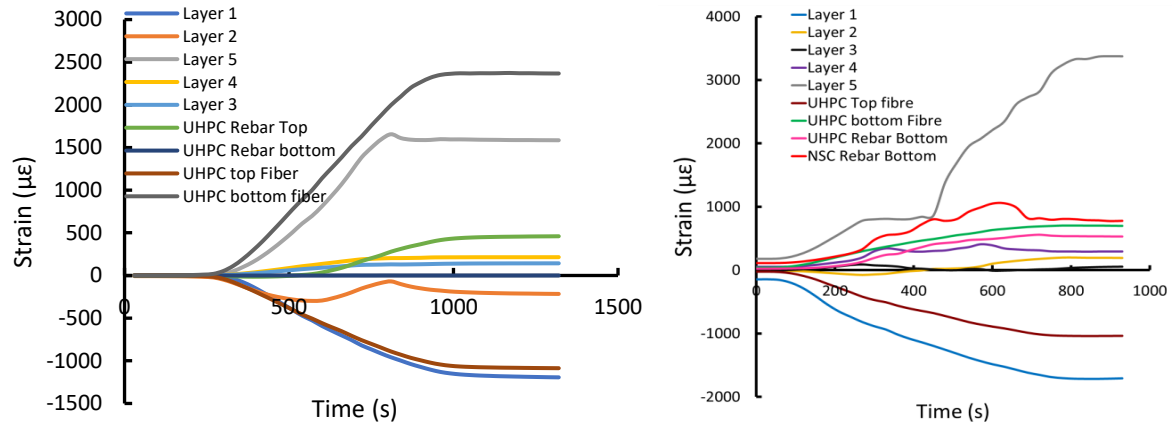


Figure 2.21. (a) BC-1 (b) BC-2

Development of Moment-Curvature Relationship

In order to analyze the flexural response a reinforced concrete member up to the failure load, it is necessary to develop a realistic relationship between moment and curvature. There is no such relationship developed for UHPC hybrid connected bridge deck panels so far to the best of author's knowledge and that is due to its complex geometry. It is not always feasible to conduct large-scale experiments in the laboratory due to high cost and lack of expertise. In this section, an analytical model is developed to predict the moment-curvature relationship of hybrid bridge deck connections which is versatile regardless of its shape and length. It uses a theoretical stress-strain constitutive model, as developed by Hsu and Hsu (1994) for normal strength concrete. Due to unavailability of theoretical stress-strain equation for ultra-high-performance concrete, a modified equation proposed by Wu et. al (2016) was implemented though the equation was prescribed for UHPC with hybrid fibers. It is observed from the analytical investigation that UHPC connected bridge deck panels can resist higher moment than NSC connected bridge deck panels for same curvature.

Analytical Investigation

The moment capacity of concrete hybrid specimens was analyzed using an analytical/mechanistic model based on cross section materials and cross-section properties. The analysis used the internal stresses based on the sectional stress-strain distribution to predict internal forces. Failure moment was calculated from the internal forces at equilibrium

of the whole member at that particular cross section. A bilinear stress-strain curve was used for modelling the steel reinforcing bars and UHPC in tension (i.e. elastic, perfectly plastic) as shown in Figure 2.22. The equations (2.5) to (2.6) of previous chapter were used for calculating the compressive stress in NSC. The model proposed by Wu et al. was used to calculate the compressive force of UHPC. The model assumes that the uniaxial stress-strain response follows the Carreira and Chu (1985) model in the ascending portion which is as follow:

$$f = \left(\frac{\beta \left(\frac{\varepsilon_c}{\varepsilon_0} \right)}{\beta - 1 + \left(\frac{\varepsilon_c}{\varepsilon_0} \right)^\beta} \right) f_0 \quad (2.5)$$

$$\beta = \frac{1}{1 - \left[\frac{f_0}{\varepsilon_0 E_0} \right]} \quad (2.6)$$

For predicting the response of descending portion, Wu et al. proposed the following modifications in the above equations

$$f = \left(\frac{k_1 \beta \left(\frac{\varepsilon_c}{\varepsilon_0} \right)}{k_1 \beta - 1 + \left(\frac{\varepsilon_c}{\varepsilon_0} \right)^{k_2 \beta}} \right) f_0 \quad (2.7)$$

$$k_1 = -4.2143 + 7.6911x - 3.5819x^2 + 0.6827x^3 - 0.0574x^4 + 0.0018x^5 \quad (2.8)$$

$$k_2 = 0.3226 + 14.9 V_l + 1980 (V_l - 0.01) * (V_s - 0.01) \quad (2.9)$$

Where, k_1 = parameter related to compression toughness index; x = compression toughness index; k_2 = parameter that depends on hybrid fiber content; V_l = long fiber content; and V_s = short fiber content

The strain profile along the height of the connection is obtained from the following equations, based on the assumption that the planar section remains planar (Figure 2.22)

$$\varepsilon_s = \frac{\varepsilon_c \times (d-c)}{c} \quad (2.10)$$

$$\varepsilon_{ut} = \frac{\varepsilon_c \times (h_c - c)}{c} \quad (2.11)$$

where, ε_c , ε_s , ε_{ut} , h_c , and d denote the strain in the extreme fiber of both NSC, and UHPC; strain in rebar; strain in the UHPC in tension; height of the slab, and effective depth of rebar.

Compressive force in normal strength concrete,

$$C_c = 2 \times \sum_{i=0}^n A_{c(i)} \left(\frac{\beta \left(\frac{\varepsilon_c}{\varepsilon_0} \right)}{\beta - 1 + \left(\frac{\varepsilon_c}{\varepsilon_0} \right)^\beta} \right) \sigma_{cu} \quad (2.12)$$

$$\text{Compressive force in UHPC, } C_u = \sum_{i=0}^n A_{u(i)} \times \left(\frac{k_1 \beta \left(\frac{\varepsilon_c}{\varepsilon_0} \right)}{k_1 \beta - 1 + \left(\frac{\varepsilon_c}{\varepsilon_0} \right)^{k_2 \beta}} \right) f_0 \quad (2.13)$$

$$\text{Tensile force of reinforcement bar, } T_s = n \times A_s \times f_y \quad (2.14)$$

$$\text{Tensile force in UHPC, } T_{u1} = 0.5 \times f_{ut} \times \sum_{i=0}^n A_{ut1(i)}; T_{u2} = f_{ut} \times \sum_{i=0}^n A_{ut2(i)} \quad (2.15)$$

$$\text{Moment capacity, } M = C_c \times y_c + C_u \times y_u + T_s \times (d - c) + T_{u1} \times y_{t1} + T_{u2} \times y_{t2} \quad (2.16)$$

where y_c , y_u , y_{t1} , and y_{t2} are the distance from the neutral axis to the centroid of the respective area calculated using the following expression

$$\bar{y} = \frac{\sum_{i=0}^n A_{(i)} \times y_{(i)}}{\sum_{i=0}^n A_{(i)}} \quad (2.17)$$

A MATLAB program was developed to execute the procedures as shown below. The program uses an iterative approach based on numerical integration. The steps are as follows

1. Select the input parameters h_c , b_c , b_u , σ_{cu} , f_0 , A_s , d and f_u . Select concrete compressive strain for both normal strength concrete and UHPC in the extreme compression fiber and assume neutral axis depth (see strain diagram in Figure 2.23).
2. The steel tensile strains are determined by similar triangles of the strain diagram (Figure 2.23). Steel tensile stresses are then determined from the stress–strain relationships of the steel rebars.

3. The tensile forces in the steel rebars are determined from the steel stress and the area of steel.
4. For the selected strain and neutral axis depth, determine concrete compressive stress for both normal strength concrete and UHPC from equations (2.5) and (2.13).
5. The UHPC tensile force is determined by multiplying the tension area of the concrete's cross-section by the stress calculated from the diagram. The centroid of the tension area represents the location of the concrete's tensile force. Both, the area and its centroid were found using numerical integration.
6. The concrete compressive force is determined by multiplying the compression area of the concrete's cross-section by the stress calculated from the equations (2.5-2.8; 2.13-2.17). The centroid of the compression area represents the location of the concrete's compressive force. Both, the area and its centroid were found using numerical integration.
7. If the compressive and tensile forces are not equal, the neutral axis depth is adjusted and steps 2–6 are repeated. It should be noted that the calculations are lengthy and hence, the iterative approach may be used.
8. After finding the neutral axis depth that satisfies force equilibrium, the internal forces and neutral axis depth are used to determine the moment (M) and curvature (ϕ) corresponding to the selected strain (step 1). The moment (M) is the sum of the moments of the compressive and tensile forces about the neutral axis, and the curvature is calculated by dividing the selected strain value by its corresponding neutral axis depth (c).
9. Repeat steps 1–8 for a range of concrete compressive strain and plot the entire stress–strain and moment–curvature curves. The entire procedure is shown in Figure 2.23 as a flow diagram.

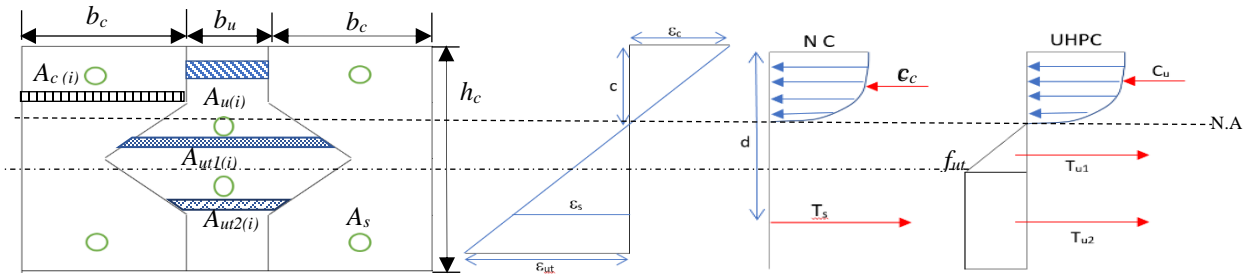


Figure 2.22. Cross section, Strain, and Stress Diagram of the connection

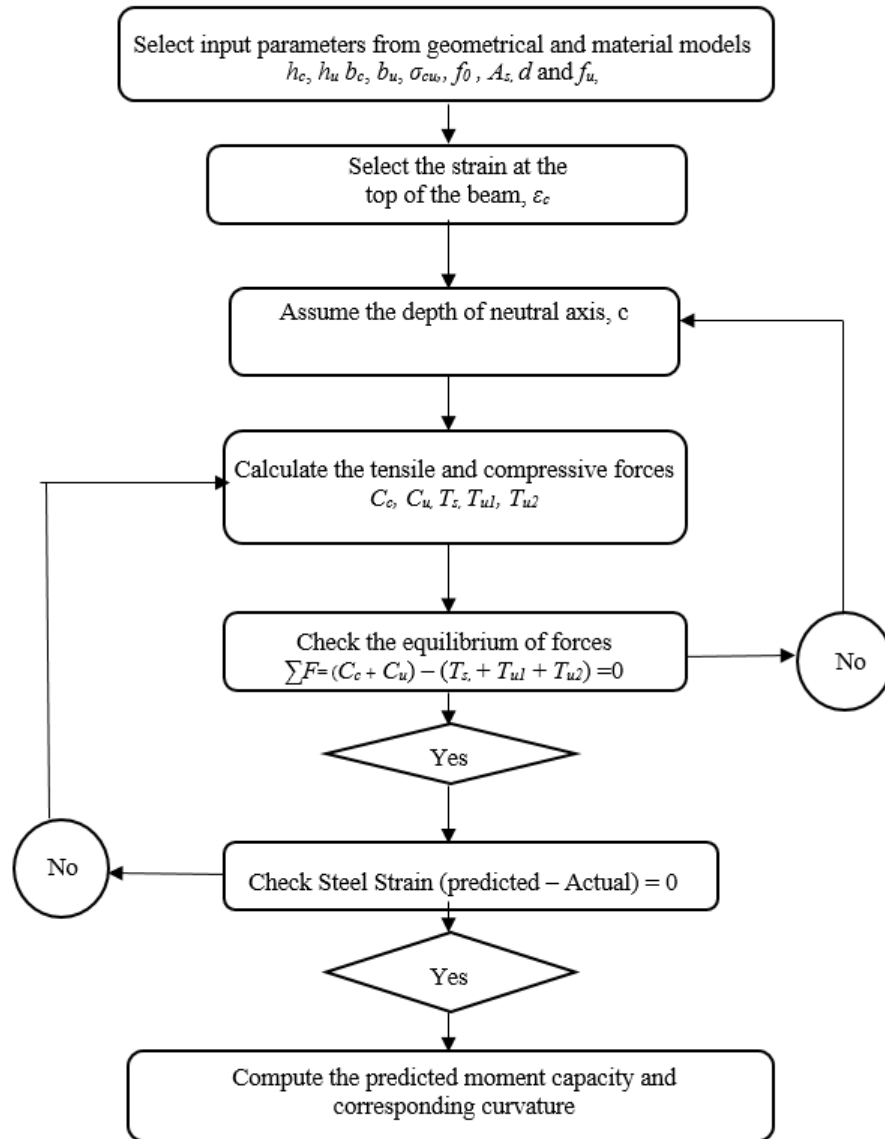


Figure 2.23. Flow diagram of the numerical process

Validation of Analytical Model

Thus far, no experimental program has been conducted to examine the moment curvature behavior of the hybrid connections made with UHPC. At first, to verify the developed code, moment curvature relationship is calculated assuming the whole connection as normal strength concrete. Whitney stress block of normal strength concrete is used for calculation and compared with the values obtained from the analytical model. Figure 2.24 shows the section and material properties used in calculating the cracking moment, yield point and

ultimate moment. It is observed from Figure 2.25 that there is no significance difference between the values obtained from the analytical model and Whitney stress block.

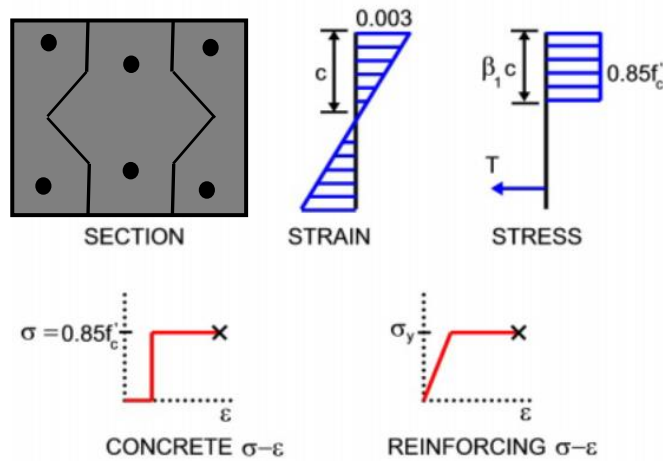


Figure 2.24. Whitney stress block for calculating moment-curvature relationship

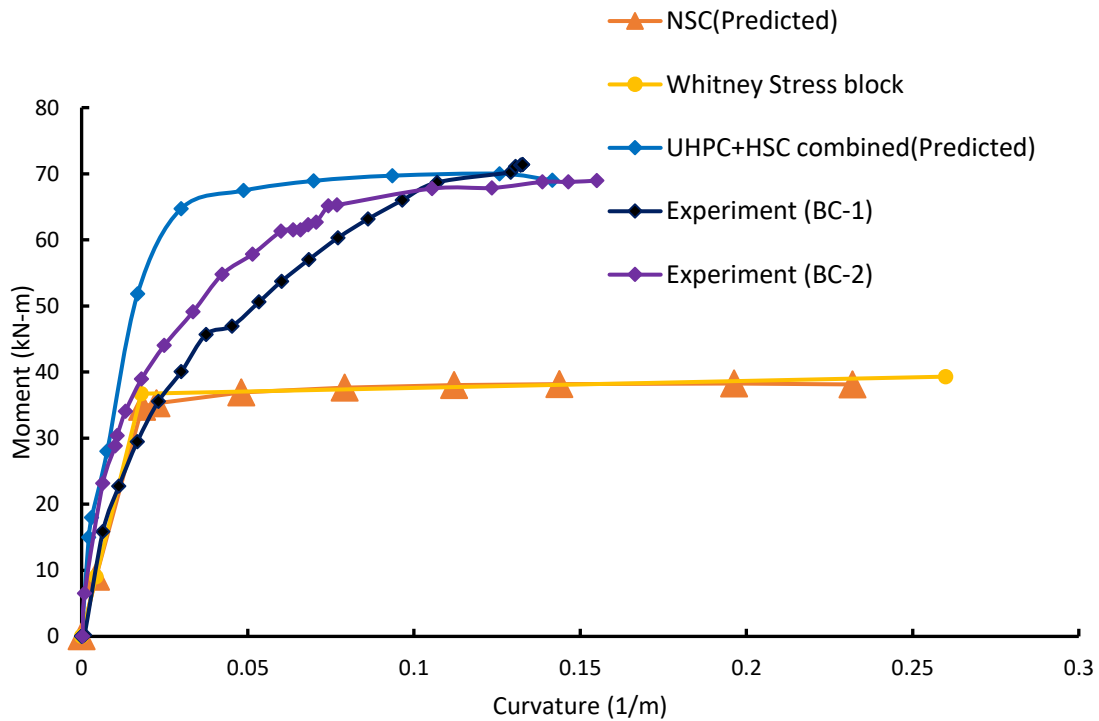


Figure 2.25. Moment-Curvature diagram for a specific cross section

The analytical model is then verified with the experimental program conducted in the laboratory. Figure 2.25 shows that the analytical model is capable of predicting the ultimate

moment quite satisfactorily though the initial stiffness is found less in experimental program. As the connection loaded twice before the final test, there might be some micro cracks which decreased the initial stiffness. It is observed from Figure 2.25 that the moment capacity increases significantly if the connection is constructed with UHPC. However, it becomes less ductile than normal strength concrete due to brittle behavior of UHPC. The analytical model is in good agreement with the conventional approach. There is a good potentiality of using this model to develop a design chart to predict the moment capacity for the design engineers.

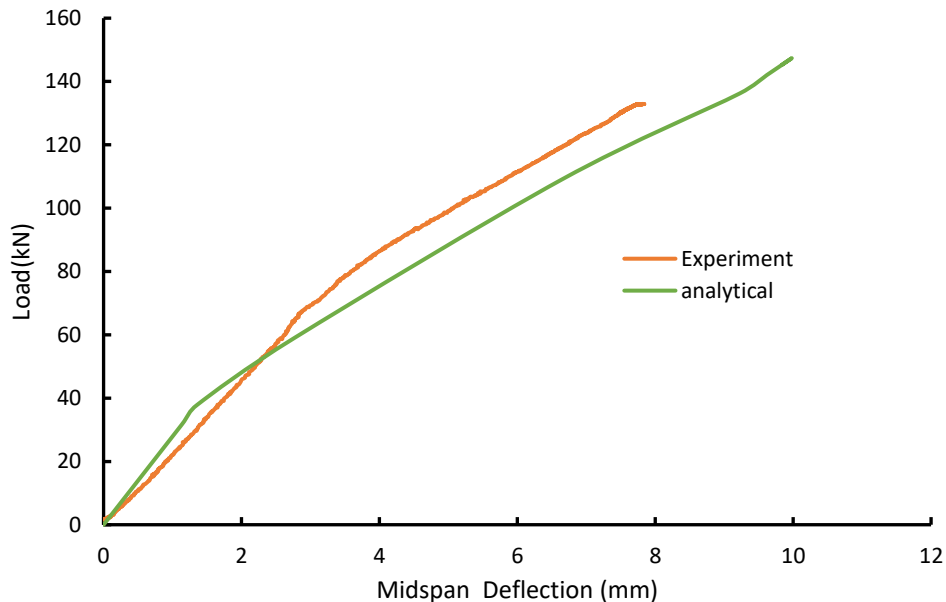


Figure 2.26. Comparison between analytical and experimental load-deflection response (BC-1)

Figure 2.26 shows the comparison between the load-deflection response of experimental program (BC-1) and the predicted one. The predicted ultimate load is found 147.36 kN which is little bit higher than the experimental value (132.88 kN). Though the analytical model is capable of tracing the load-deflection response quite satisfactorily, but the initial stiffness is slightly overestimated by the analytical model which is obvious.

Graphical User Interface (GUI) for Parametric Study

To understand the effect of different parameters such as concrete strength, connection width and type, precast panel width, reinforcement details, a program with a graphical user interface is generated using MATLAB. The program and the GUI consist 500 lines of code.

This interface will provide design engineers the ability to input certain values for the parameters and observe the moment – curvature relationship which will provide an idea about the flexural response of a hybrid connection. This graphical interface will not only save money but also it will reduce the labor cost, and time to perform experimental testing. Figure 2.27 shows the GUI for predicting moment-curvature relationship. Figure 2.28 shows the GUI after plotting the graph.

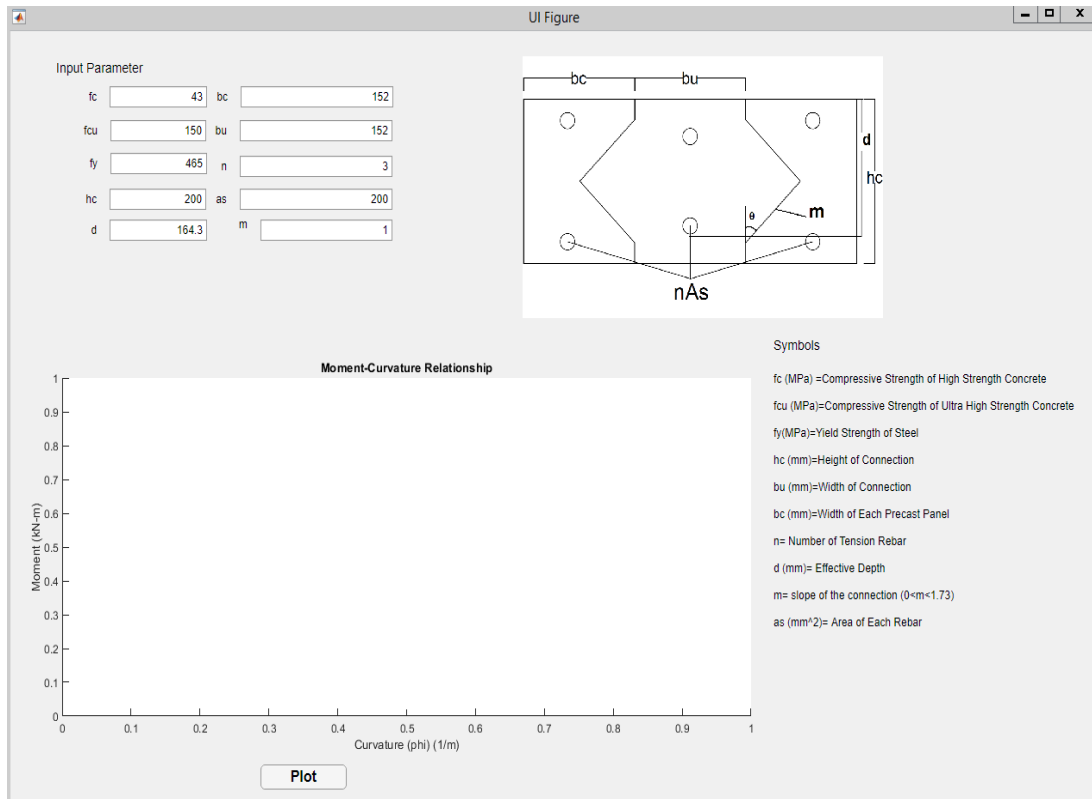


Figure 2.27: Graphical User Interface (after initialization)

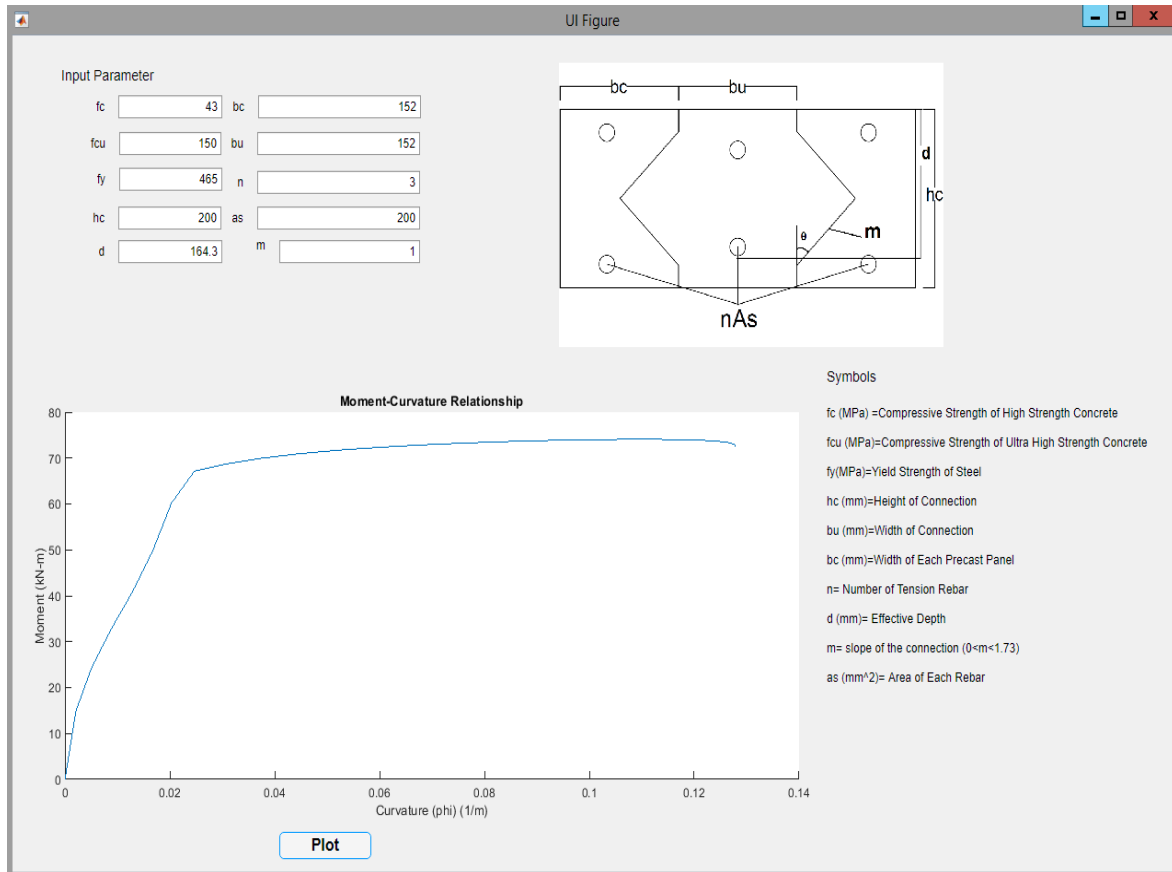


Figure 2.28: Graphical User Interface (after plotting)

Conclusions

In this study, the authors developed UHPC mixes using Idaho materials. Nine mix designs were developed using locally available materials. Among them one mix design having compressive strength of 20.35 ksi was selected for further performance evaluation. The performance of locally developed UHPC was evaluated by constructing two 8ft span hybrid connections between two precast panels with local UHPC closure pour which was tested under static loading until failure. The test results confirm better flexural performance of UHPC closure than HSC against flexure. An analytical method was developed and implemented using MATLAB code to predict the moment-curvature relationship. In addition, a graphical user interface was developed to perform the parametric study. Based on the performance evaluation the following conclusions can be drawn.

- Locally available basalt, cement, admixture and domestically available steel can produce UHPC without heat curing.
- UHPC of 20.35 ksi compressive strength can be produced without using expensive materials, such as quartz powder and imported fibers.
- The hybrid connection produced with local UHPC showed good flexural resistance.
- The cracking pattern revealed that the hybrid connection failed due to tensile cracking in NSC panels and UHPC connection.
- The analytical model is capable of predicting the moment-curvature response of UHPC hybrid connection, normal strength concrete and full UHPC beam as well.
- The Graphical User Interface app will provide the design engineers a tool for predicting the moment-curvature relationship of hybrid bridge deck connections which is versatile regardless of its shape and length.

References

ASTM C109/C109M-16a (2016) “Standard Test Method for Compressive Strength of Hydraulic Cement Mortars (Using 2-in. or [50-mm] Cube Specimens)”, ASTM International, West Conshohocken, PA.

ASTM C128-15 (2015) “Standard Test Method for Relative Density (Specific Gravity) and Absorption of Fine Aggregate”, ASTM International, West Conshohocken, PA.

ASTM C136/C136M-14 (2014) “Standard Test Method for Sieve Analysis of Fine and Coarse Aggregates, ASTM International”, West Conshohocken, PA.

ASTM C192/C192M-16 (2016) “Standard Practice for Making and Curing Concrete Test Specimens in the Laboratory”, ASTM International, West Conshohocken, PA

Balshin MY. Relation of mechanical properties of powder metals and their porosity and the ultimate properties of porous-metal ceramic materials. DoklAskd SSSR 1949;67(5):831–4.

Colleparidi, S., Coppola, L., Troli, R., Tet al. (1997) “Mechanical Properties of Modified Reactive Powder Concrete”. Proceedings of the Fifth CANMET/ACI International Conference on Superplasticizers and Other Chemical Admixtures in Concrete, Rome, Italy, Publication

No. SP-173, Ed., Malhotra V.M., American Concrete Institute, Farmington Hills, MI, pp. 1-21.

Graybeal, B., UHPC in the U.S. highway transportation system, in: Proceedings of the Second International Symposium on Ultra High-Performance Concrete, Kassel University Press GmbH, Kassel, Germany, 2008, p. 11.

Graybeal, B., 2006 b "Material Property Characterization of Ultra-High-Performance Concrete," FHWA, U.S. Department of Transportation, Report No. FHWA-HRT-06-103, McLean, VA,

Habel, K. et al., "Ultra-High-Performance Fiber Reinforced Concrete Mix Design in Central Canada," Canadian Journal of Civil Engineering, Vol. 35, No. 2, February 2008, pp. 217–224.

Hasselmann DPH. Griffith flaws and the effect of porosity on tensile strength of brittle ceramics. J Am Ceram Soc 1969; 52:457.

Kazemi, S. and Lubell, A., "Influence of Specimen Size and Fiber Content on Mechanical Properties of Ultra-High-Performance Fiber-Reinforced Concrete," ACI Materials Journal, Vol. 109, No. 6, November–December 2012, pp. 675–684.

L. Sorelli, G. Constantinides, F.J. Ulm, et al., The nano-mechanical signature of ultra-high-performance concrete by statistical nanoindentation techniques. Concr. Res. 38 (12) (2008) 1447–1456.

Larrard, F. De., Sedran, T. Optimization of ultra-high-performance concrete by the use of a packing model, Cem. Concr. Res. 24 (6) (1994) 997–1009.

Li L, Aubertin M. A general relationship between porosity and uniaxial strength of engineering materials. Can J Civil Eng 2003; 30:644–58.

Liu J., Han F., Cui G., et al. (2016) "Combined effect of coarse aggregate and fiber on tensile behavior of ultra-high-performance concrete". Construction and Building Materials, 121, pp. 310-318.

Rebentrost, M., Wight, G., Experience and applications of ultra-high-performance concrete in Asia, in: Proceedings of the 2nd International Symposium on Ultra-High-Performance Concrete, Kassel University Press GmbH, Kassel, Germany, 2008, pp. 19–30.

Reda, M.M., Shrive, N.G., Gillott, J.E., Microstructural investigation of innovative UHPC, *Cem. Concr. Res.* 29 (3) (1999) 323–329.

Richard, P., Cheyrezy, M. (1994), Reactive powder concretes with high ductility and 200–800 MPa compressive strength, *ACI Mater. J.* 144 (3) 507–518.

Richard, P., Cheyrezy, M., Composition of reactive powder concretes, *Cem. Concr. Res.* 25 (7) (1995) 1501–1511.

Rougeau, P. and Borys, B., “Ultra High Performance Concrete With Ultrafine Particles Other Than Silica Fume,” Proceedings of the International Symposium on Ultra High Performance Concrete, Ed., Schmidt, M., Fehling, E., and Geisenhanslüke, C., Kassel University Press, Kassel, Germany, 2004, pp. 213–225.

Ryshkevitch R. Compression strength of porous sintered alumina and zirconia. *J Am Ceram Soc* 1953;36(2):65–8.

Schiller KK. Strength of porous materials. *Cem. Concr. Res.* 1971; 1:419–22.

Schmidt, M. Fehling, E., Ultra-high-performance concrete: research, development and application in Europe, in: 7th International Symposium on the Utilization of High-Strength- and High-Performance-Concrete, ACI Washington, 2005, SP.228-4, pp. 51–78.

Sobuz H. R., Ali M.S. Mohamed, Singh M., Griffith M.C., and Sheikh A.H. (2016) “Manufacturing ultra-high performance concrete utilising conventional materials and production methods”. *Construction and Building Materials*, 111, pp. 251-261.

Wille K., and Boisvert-Cotulio C. (2015) “Material efficiency in the design of ultra-high performance concrete”. *Construction and Building Materials*, 86, pp. 33-43.

Wille, K., Naaman, A.E., and Parra-Montesinos, G.J., “Ultra-High-Performance Concrete with Compressive Strength Exceeding 150 MPa (22 ksi): A Simpler Way,” *ACI Materials Journal*, Vol. 108, No. 1, January–February 2011, pp. 46–54.

Yunsheng, Z., Wei, S., Sifeng, L. Preparation of C200 green reactive powder concrete and its static–dynamic behaviors, *Cem. Concr. Compos.* 30(9) (2008) 831–838.

Z. Yang, Study on mechanical properties of reactive powder concrete (Ph.D. thesis), DaLian JiaoTong University, China, 2008.

Zhao S, Fan J., and Sun W. (2014) “Utilization of iron ore tailings as fine aggregate in ultra-high-performance concrete”. *Construction and Building Materials*, 50, pp.540-548.

ASTM C192/C192M-16 (2016) “Standard Practice for Making and Curing Concrete Test Specimens in the Laboratory”, ASTM International, West Conshohocken, PA.

Chapter 3: Numerical Study on the Low-Velocity Impact Response of Ultra-High-Performance Fiber Reinforced Concrete Beams

“Numerical study on the low-velocity impact response of ultra-high-performance fiber reinforced beams” published in *Structures*, August 2019, Volume 20, Pages 570-580

Abstract

The material and structural behaviors of Ultra High-Performance Fiber-Reinforced Concrete (UHP-FRC) under a high strain rate loading are different than a quasi-static loading condition. UHP-FRC has a very high compressive strength compared to conventional concrete; However, the failure strain of UHP-FRC is not enough to withstand large plastic deformations under high strain rate loading such as impact and blast loading. Due to the high cost of large-scale experimental research of structural elements under impact loading, modeling of UHP-FRC girders using computer aided program has become a need. Hence, this study aims to develop a finite element model of UHP-FRC to simulate low-velocity impact phenomena. The responses obtained from the numerical study are in good agreement with the experimental results for impact loads. Five different types of UHP-FRC beams were simulated under impact loading to observe the global and local material response. The key parameters investigated were the reinforcement ratio (ρ), impact load under various drop heights (h), and the failure phenomena. It was observed that higher reinforcement ratio showed better deflection recovery under the proposed impact. Also, for a specific reinforcement ratio, the maximum deflection increases approximately 15% when drop height decreases from 100 mm to 25 mm. Moreover, the applicability of concrete damage plasticity model for impact loading is investigated. The results also provide recommendations for predicting the location of the local damage in UHPFRC beams under impact loading.

Keywords: Nonlinear impact analysis, Ultra-High-Performance Concrete (UHPC), Reinforcement ratio, Sensitivity analysis, and Accelerated construction.

Introduction

Impact loading is an extremely severe loading condition characterised by a force of great intensity within a very short duration. The behavior of a structural component under impact loading includes two response phases, a local response due to stress waves generated within

short duration of impact followed by a free vibration effect due to elastic-plastic deformation over an extended period after impact. The overall response depends predominantly on the loading rate and the dynamic behavior of the structural component (Fujikake et al. 2010). So far, significant efforts have been provided in developing innovative ways to increase the long-term structural performance and currently, the use of Ultra High-Performance Concrete (UHPC) has drawn the attention for its superior properties such as early high strength gain, extreme durability, low permeability and long-term stability. The term UHPC refers to a class of advanced cementitious composite materials where innovative technology of cement and concrete industry blends together (Graybeal 2006). Therefore, UHPC is considered a promising material for innovative structures subjected to severe loading conditions such as impact, shock, and explosive loadings (Fujikake et al. 2006).

Despite of having excellent mechanical and material properties, the use of UHP-FRC is not widespread due to lack of widely accepted design guidelines or a UHP-FRC constitutive law. Some experimental programs have been conducted recently focusing on material characterization (Graybeal 2006), flexural and shear tests of I-girder (Graybeal 2008; Yuan and Graybeal 2011), prototype pi-girders and second-generation pi-girders (Graybeal 2009). Studies showed that UHP-FRC girders had higher flexural capacities than conventional girders. A composite deck system was proposed by Shao et al. (2013) consisting an orthotropic steel deck stiffened with reactive powder concrete layer. Due to high compressive and tensile strength, UHP-FRC are now being considered for structural rehabilitation. A finite element analysis was conducted by Safdar et al. (2016) to investigate the flexural behavior of reinforced concrete beams strengthened with UHP-FRC. It was observed that the flexural strength of the retrofitted beams increased with the increase of UHP-FRC layer thickness.

Moreover, the stiffness was improved, and the formation of the cracks were delayed significantly. However, most of the research has been focused on the static performance of the UHP-FRC structural elements. Unfortunately, current understanding of the impact and blast resistances of Ultra High Performance Fiber Reinforced Concrete (UHP-FRC) beams under high strain rates is very limited (Fujikake et al. 2006, 2010). Ngo et al. (2007) reported that UHP-FRC is less sensitive to strain rate than normal strength concrete (NSC) and high

strength concrete (HSC). Aoude et al. (2015) demonstrated that UHP-FRC is also capable of improving blast resistance capacity by reducing maximum and residual deflection. In addition, Li et al. (2015) found the positive effect of using UHP-FRC materials in construction of blast protective structures.

Although conducting experimental tests for investigating the impact performances of UHP-FRC structures is straightforward, tests are expensive and time consuming. For these reasons, developing a dependable 3D finite element impact model has become a necessity. Numerical modeling of UHP-FRC has been always challenging due to non-availability of post-peak behavior of UHP-FRC which may have a significant effect on the prediction of the damage parameters (Chen and Graybeal 2011). The main objective of this study is to develop a finite element model that can be applied for a variety of UHP-FRC beams subjected to low velocity impact loading. The applicability of concrete-damage plasticity model for low-velocity impact loading is also investigated. Moreover, a parametric study has been conducted to observe the influence of reinforcement ratio and drop height of impact load on the structural response of UHP-FRC beams under low velocity impact loading.

Experimental Program

To validate the finite element model, two full-scale experimentally tested UHPFRC beams (UH-N and UH-S-0.53%) were selected from the study “Response of ultra-high-performance fiber-reinforced concrete beams with continuous steel reinforcement subjected to low-velocity impact loading” by Yoo et al. (2015). UH-N represents the UHP-FRC beam with no reinforcement bar and UH-S-0.53% stands for UHP-FRC beam with 0.53% reinforcement ratio. In the experimental program, a 270-kg rigid hammer with a striking face of 20 mm thick and 40 x 210 mm sized rectangular surface was dropped from a constant height of 1600 mm. The length of each beam was 2900 mm with a clear span of 2500 mm. Each beam consisted of a rectangular section cross section of 200 mm width and 270 mm height. The kinetic energy and the impact velocity were reported as 4233.6 J and 5.6 m/s, respectively. Figure 3.1 (a), (b) and (c) show more details of the experimental program. Table 3.1 represents the mix proportions of UHPFRC used in the test program. The value of the elastic modulus, compressive strength, and tensile strength of UHPFRC used in this experiment were 44 GPa, 9.2 MPa and 152.5 MPa respectively.

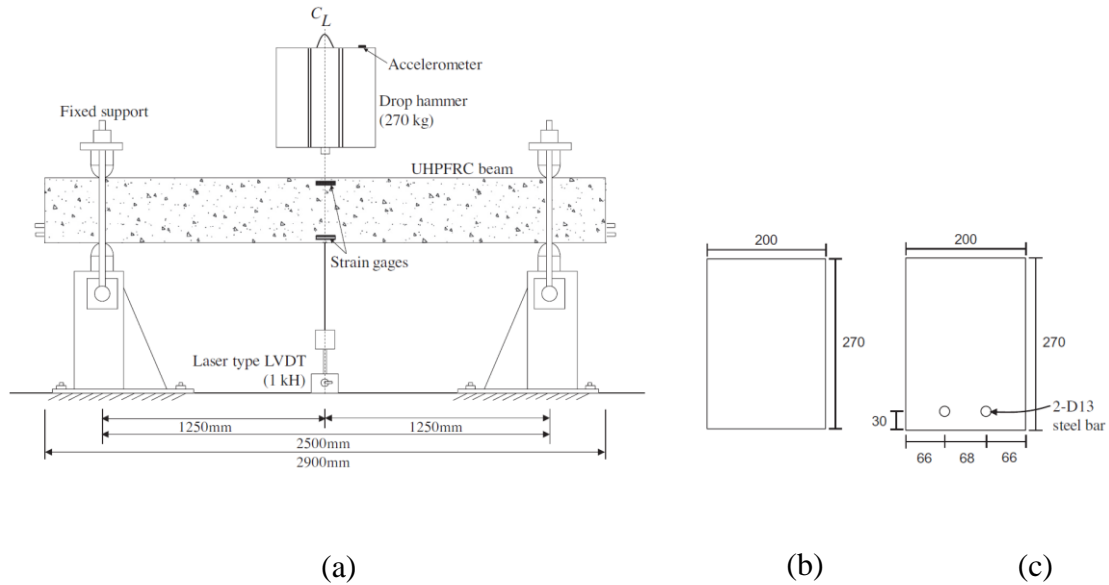


Figure 3.1: (a) Experimental Program (b) cross section details of UH-N (c) UH-S-0.53% (Yoo et al. 2015)

Table 3.1: Mix Proportions of UHPFRC (Yoo et al. 2015)

Relative weight ratios to cement						Steel Fiber (V _f , %)	Flow (mm)
Cement	Water	Silica fume	Sand	Silica flour	Superplasticizer		
1.00	0.25	0.25	1.10	0.30	0.016	2%	230

Finite Element Modeling

The numerical simulations were conducted using the ABAQUS program, which is a general FE analysis software for modeling the nonlinear mechanics of structures, fluids, and their interactions. For solving problems associated with large deformation and multiloading environments; ABAQUS offers both implicit and explicit numerical methods. The ABAQUS/explicit method was used for simulating the FE models as it can effectively handle severely nonlinear behavior.

Material Constitutive Models

Concrete damage plasticity model for low-velocity impact modeling

Various concrete models are available in the software material library to model the normal and high strength concrete in ABAQUS. However, there is a lack of enough data for developing constitutive model for UHP-FRC under various confining pressure. It is reported that the compressive strength and deformation capacity of UHP-FRC are enhanced by lateral confinement (Curbach and Speck 2008; Wang et al. 2016). Also, the multiaxial strength of UHP-FRC can be related to uniaxial strength (Curbach and Speck 2008; Fehling et al. 2008). Grünberg et al. (2008) reported that at low confinement stress with increasing hydrostatic pressure, the yield surface on the deviatoric planes changes from triangular shape to nearly circular shape. Moreover, it is also observed that the uniaxial compressive to tensile strength ratio of UHP-FRC is almost similar to NSC (Williams et al. 2009). Based on these limited researches, it can be concluded that UHP-FRC can be modelled under a three-dimensional state of stress using combined damage-plasticity models or classical plasticity-based models.

A concrete damage plasticity model (CDP) model was first introduced by Lubliner et al. (1989) for monotonic loading and then modified by Lee and Fenves (1998) for cyclic and dynamic loadings. The CDP model can incorporate separate inputs for stress-strain relationship, damage parameters and strain rate in tension and compression. Moreover, CDP model is capable of representing different concrete mixes using some adjustable input parameters which can be obtained experimentally. For NSC and HSC, these parameters are well defined. Nasrin and Ibrahim (2018) reported that CDP model can predict the behavior of UHP-FRC satisfactorily under static loading. However, the performance of CDP model in predicting UHP-FRC under low velocity impact is not evaluated yet.

The yield surface of the CDP model is noncircular in shape for allowing different yield triaxial tension and compression stresses. The shape factor K_c which is the ratio of second stress invariant for tension and compression at same hydrostatic stress governs the shape of yield surface. Figure 3.2 (a) represents the yield surface in the deviatoric plane corresponding to different K_c values. For NSC, the default value of K_c is 2/3. However, the value of K_c should be in the range of 0.5 to 1.0 to ensure convexity of the surface. Another important parameter is the ratio of biaxial to uniaxial compression stress to describe the material state

when it undergoes biaxial compression. Though the default value of stress ratio (σ_{b0}/σ_{c0}) in ABAQUS is 1.16 for NSC, studies showed that for UHP-FRC, this value is lower than the NSC value (Curbach and Speck 2008; Wang et al. 2016).

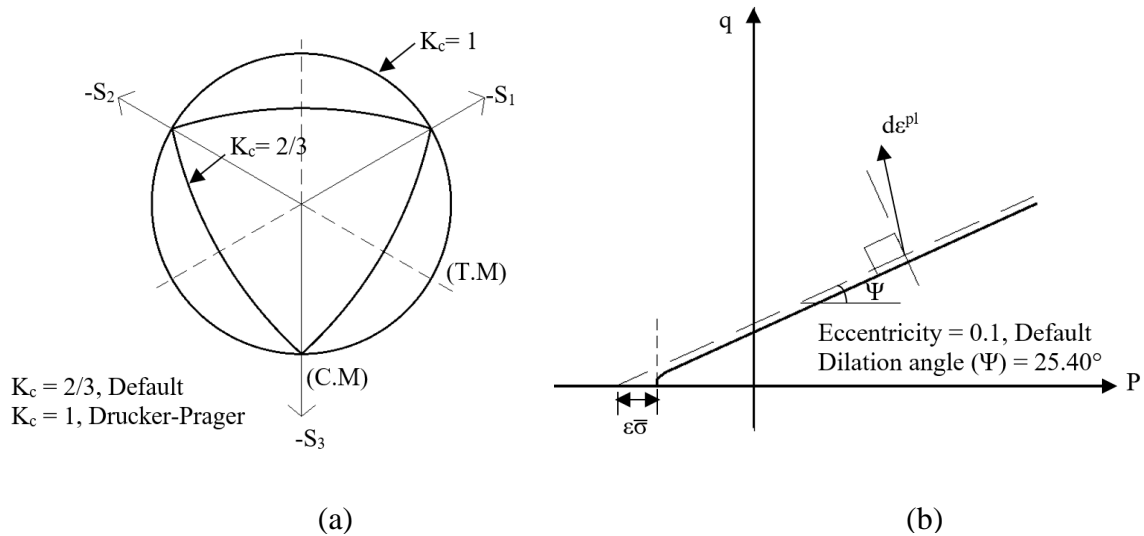


Figure 3.2: (a) The yield surface in the deviatoric plane for different K_c values (b) yield surface in meridian plane.

In CDP model, dilation angle (Ψ) and the flow potential eccentricity (ϵ) define the potential plastic flow of concrete under three-dimensional stress state. Figure 3.2 (b) shows a geometrical representation of Ψ and ϵ . The dilation angle represents the change of volumetric strain under plastic deformation whereas, the flow potential eccentricity (ϵ) represents the rate of flow function approaching the asymptote. The value of dilation angle ranges from 25° to 40° for NSC, although no research has been conducted yet to identify the dilation angle of UHP-FRC.

UHP-FRC constitutive model

The input parameters of UHP-FRC such as stress-strain response, elastic modulus, Poisson's ratio etc. are collected from the experimental program (Yoo et al. 2015). Figure 3.3 (a) and (b) show the compressive and tensile stress-strain relationship of the UHP-FRC used in this study.

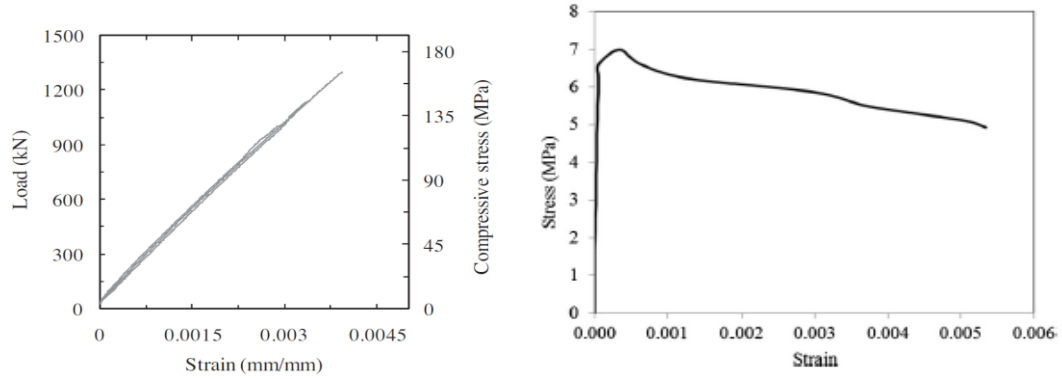


Figure 3.3: (a) Compressive behavior of UHPFRC (Yoo et al. 2015) (b) Tensile behavior of UHPFRC (Al-Osta et al. 2017)

CDP model is used for defining the non-linear behavior of compressive and tensile stresses. Hardening data are provided in terms of an inelastic strain, $\tilde{\varepsilon}_c^{in}$. The compressive inelastic strain can be calculated by Equation 3.1,

$$\tilde{\varepsilon}_c^{in} = \varepsilon_c - \varepsilon_{0c}^{el} \quad (3.1)$$

where $\varepsilon_{0c}^{el} = \frac{\sigma_c}{E_0}$, elastic strain corresponding to undamaged material as shown in Figure 3.4

(a). Unloading data are provided in terms of damage curves, $d_c - \tilde{\varepsilon}_c^{in}$. ABAQUS converts the inelastic strain to plastic strain using following relationship

$$\tilde{\varepsilon}_c^{pl} = \tilde{\varepsilon}_c^{in} - \frac{d_c}{(1 - d_c)} \frac{\sigma_c}{E_0} \quad (3.2)$$

Post failure behavior of concrete in tension is provided by cracking strain, $\tilde{\varepsilon}_t^{ck}$. The cracking strain can be calculated from Equation 3.3.

$$\tilde{\varepsilon}_t^{ck} = \varepsilon_t - \varepsilon_{0t}^{el} \quad (3.3)$$

where $\epsilon_{0t}^{el} = \frac{\sigma_t}{E_0}$, elastic strain corresponding to undamaged material as shown in Figure 3.4

(b). tension stiffening data are provided in terms of damage curves, $d_t = \tilde{\epsilon}_t^{ck}$. ABAQUS converts the cracking strain to plastic strain using following relationship

$$\tilde{\epsilon}_t^{pl} = \tilde{\epsilon}_t^{ck} - \frac{d_t}{(1-d_t)} \frac{\sigma_t}{E_0} \quad (3.4)$$

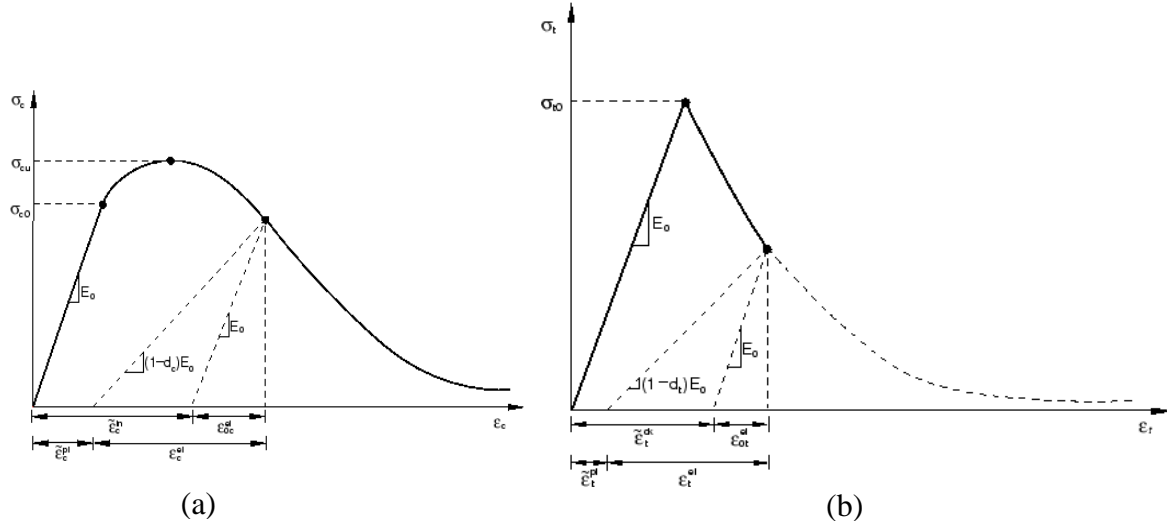


Figure 3.4: (a) Concrete compressive hardening (b) Concrete tension stiffening (ABAQUS Analysis User's Manual, 6.10).

The damage parameters in compression, d_c and tension, d_t are determined from the following equations proposed by Birtel and Mark (2006).

$$d_c = 1 - \frac{\sigma_c E_c^{-1}}{\epsilon_c^{pl} \left(\frac{1}{b_c} - 1 \right) + f_c E_c^{-1}} \quad (3.5)$$

where

d_c = Concrete compression damage parameter

f_c = Compressive Stress

E_c = Modulus of elasticity of concrete

ϵ_c^{pl} = Plastic strain corresponding to compressive strength

b_c = Constant ranges $0 < b_c < 1$

$$d_t = 1 - \frac{\sigma_t E_c^{-1}}{\epsilon_t^{pl} \left(\frac{1}{b_t} - 1 \right) + f_t E_c^{-1}} \quad (3.6)$$

where

d_t = Concrete tension damage parameter

f_t = Tensile Stress

E_c = Modulus of elasticity of concrete

ϵ_t^{pl} = Plastic strain corresponding to tensile strength

b_t = Constant ranges $0 < b_t < 1$

Initially, the value of dilation angle (ψ), plastic flow potential eccentricity (ϵ), the ratio of biaxial to uniaxial compressive strengths (σ_{b0}/σ_{co}), and the shape factor (K_c) are set to 15° , 0.1, 1.16 and 0.67, respectively according to the study conducted by Chen and Graybeal (2011). For predicting the behavior of UHP-FRC, those parameters are modified based on a sensitivity analyses which will be discussed in the following section. Table 3.2 shows the input parameters used in the damage model.

Table 3.2: Ultra-High-Performance Concrete parameters used in the plastic damage model

Compressive Strength (MPa)	Tensile Strengt h (MPa)	Mass Density (ton/mm ³)	Young's Modulus (MPa)	Poisson's Ratio	Dilation Angle ψ (Degrees)	Eccentricity ϵ	f_{b0}/f_{co}	b_c/b_t
152	7	2.565E-009	44000	0.18	15	0.1	1.16	0.67

Steel-reinforcement constitutive model

Reinforcing steel has been modeled using a 2-noded linear 3-D truss element (T3D2).

Bilinear stress-strain curve is adopted for the simulation. The other parameters used to define the behavior of reinforcing steel are shown in Table 3.3.

Table 3.3: Parameters of reinforcing steel

Type	Poisson's ratio	Elastic Modulus (MPa)	Mass Density(ton/mm ³)	Yield Stress (MPa)
Steel	0.3	200,000	7.85E-009	522.7

Mesh configuration, Load and boundary condition

After performing a mesh sensitivity analysis, a 10 mm mesh size was selected for simulating the beam which can predict the experimental results quite satisfactorily in a reduced computational time. However, a coarser mesh of 20-mm is adopted for the hammer load as hammer is not point of interest. A single impact load was modeled to apply impact at the mid-span by dropping a free-falling weight of 270 kg, and the striking face consisted of a 20-mm thick and 40 x 210 mm sized rectangular steel plate with a flat contact surface in accordance with the experimental setup. Fixed support conditions are applied to the top and bottom plate at both ends. The assigned impact velocity is 5.6 m/s, which is similar to the experimental testing. The loading conditions and mesh configuration are presented in Figure 3.5 and Figure 3.6.

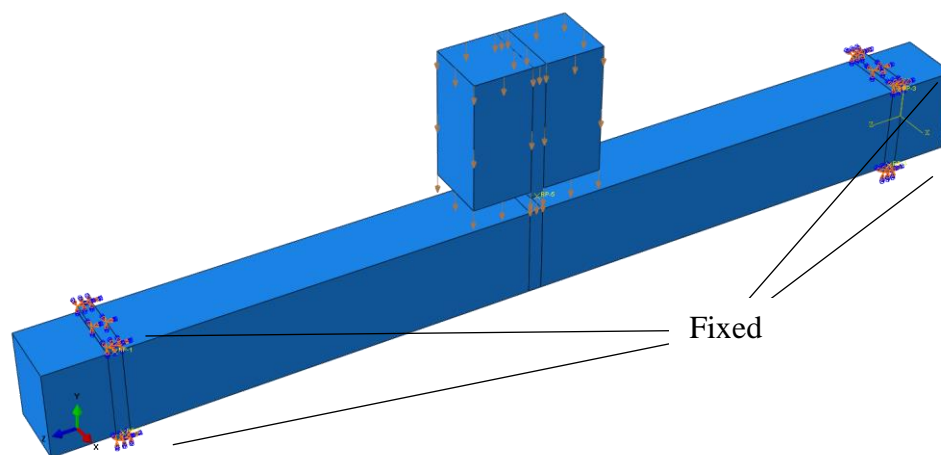


Figure 3.5: Load and Boundary condition

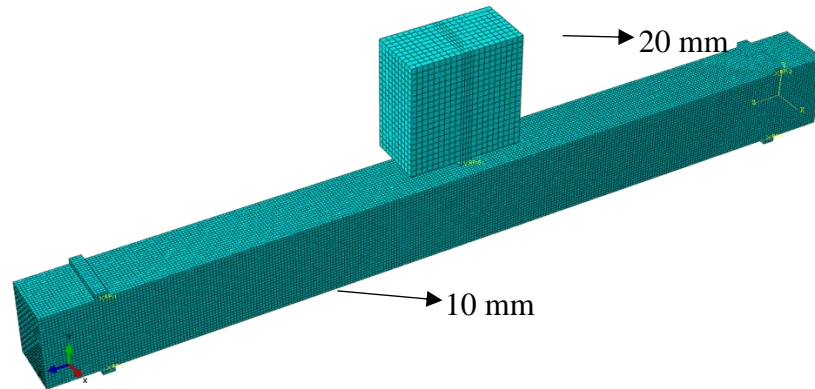


Figure 3.6: Mesh Configuration

Sensitivity Analysis

As mentioned before, the input parameters are initially taken from the study conducted by Chen and Graybeal (2011). The parameters with high uncertainty i.e. uniaxial tensile strength and CDP parameters were estimated from literature. The numerical results were matched with the experimental results to finalize the value of each parameter. Due to the lack of experimental data for defining the behavior of UHP-FRC under impact loading, sensitivity analyses were performed to observe the influence of each parameter on the overall beam performance. Each parameter is varied over a large range of possible values to observe the effect.

Effect of Dilation Angle

Dilation angle indicates the angle of inclination of the failure surface of concrete towards the hydrostatic surface. It is measured in the meridional plane. Dilation angle characterizes the performance of concrete under compound stress and interpreted as the internal friction angle of concrete (Kmieciak and Kamiński 2012). Figure 3.7 (a) and (b) show the effect of dilation angle on the midspan deflection. The angle of dilatancy of concrete was varied from 10° to 20° . Numerical results for both beams showed that the higher dilation angle results in lower midspan deflection and dilation angle of 20° fits well with the experimental results. The amount of dilation depends on the microstructure of the materials. As, UHPC is very dense material it has lower dilation angle than the conventional concrete. The midspan deflection

decreases 19.4 % and 20.62 % for UH-N and UH-S-0.53% respectively when dilation angle changes from 10° to 20° .

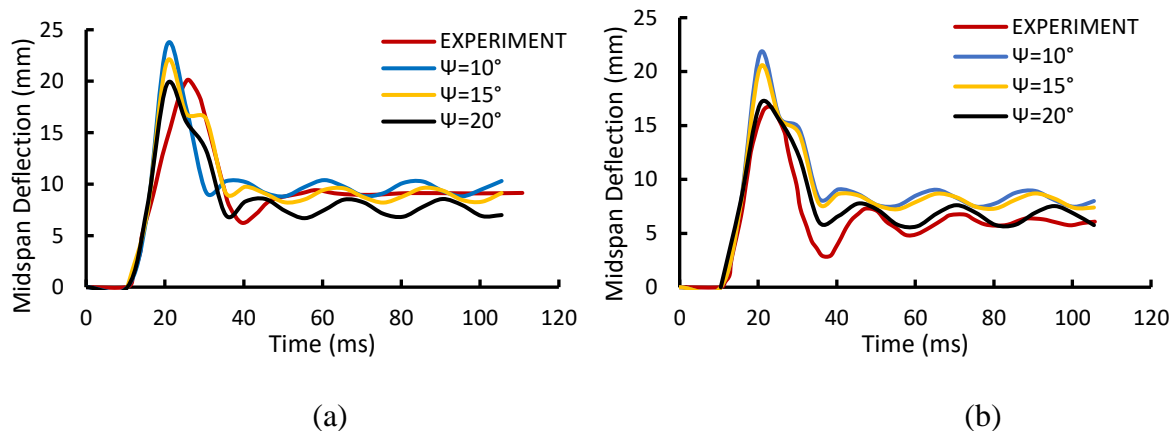


Figure 3.7: Effect of dilation angle on midspan deflection (a) UH-N (b) UH-S-0.53%

Effect of Shape Factor

The shape factor (K_c) is a ratio of the distance between hydrostatic axis and compressive meridian to the distance between hydrostatic axis and tension meridian in the deviatoric cross-section. According to the classic Drucker–Prager strength hypothesis, the deviatoric cross section of the failure surface becomes a circle when K_c is 1. This ratio is always higher than 0.5 and the CDP model recommends a value of $2/3$. Figure 3.8 (a) and (b) show the effect of different shape factors on the midspan deflection. Numerical results for both beams showed that there is no significant effect of shape factor on midspan deflection and $K_c = 2/3$ fits well with the experimental results. However, $K_c = 0.5$ showed lower values of mid-span and residual deflection in both cases.

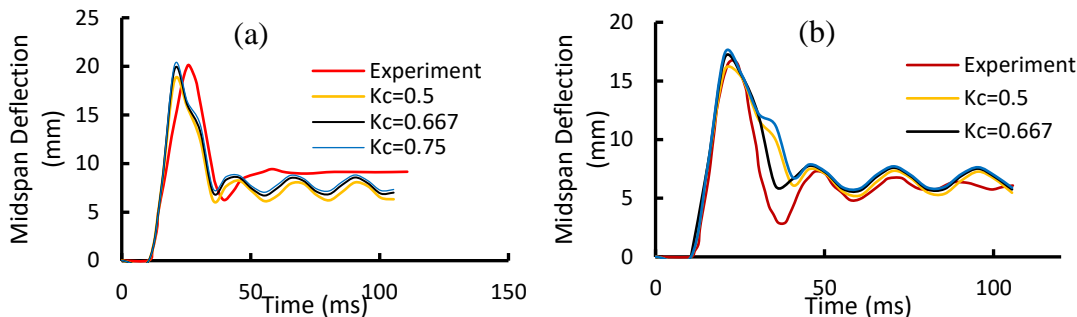


Figure 3.8: Effect of shape factor on midspan deflection (a) UH-N (b) UH-S-0.53%

Effect of Stress Ratio (σ_{b0}/σ_{c0})

The stress ratio (σ_{b0}/σ_{c0}) indicates the point in which the concrete undergoes failure under biaxial compression. Two different value of stress ratio (1.10 and 1.16) were assumed and Figure 3.9 (a) and (b) confirm that the stress ratio does not have any impact on numerical results. However, $\sigma_{b0}/\sigma_{c0} = 1.10$ is selected for further numerical study as reported by Curbach and Speck (2008) for UHPC.

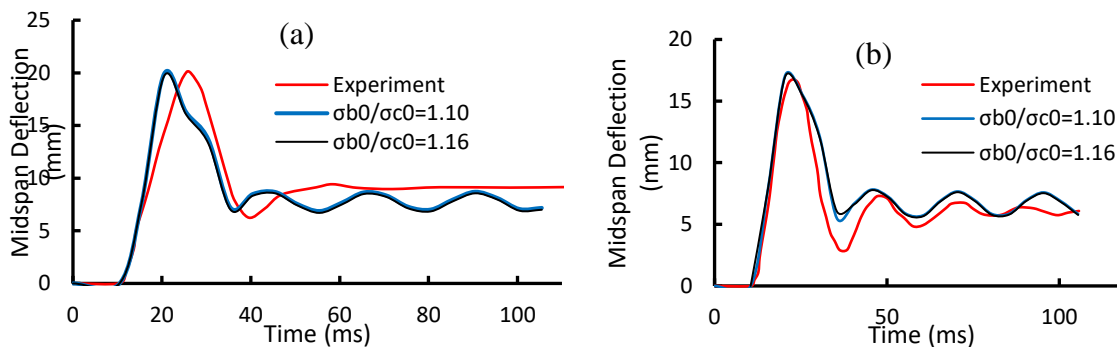


Figure 3.9: Effect of stress ratio on midspan deflection (a) UH-N (b) UH-S-0.53%

Table 3.4 summarizes the maximum and residual deflection found for all UHP-FRC beams under impact loading. After considering all the results, a dilation angle of 20° , stress factor of 1.10 and shape factor of 0.67 were selected for further study.

Table 3.4: Sensitivity Analysis results

Sensitivity Test	Variables	UH-N						UH-S-0.53%					
		δ_{max}			δ_{Res}			δ_{max}			δ_{Res}		
		(Exp.)	(FEM)	(EXP.)/ (FEM)	(Exp.)	(FE M)	(Exp.)/ (FEM)	(Exp.)	(FEM)	(EXP.)/ (FEM)	(Exp.)	(FE M)	(Exp.)/ (FEM)
Dilation angle	10	19.8	23.49	0.84	8.98	9.64	0.93	16.65	21.7	0.77	6.96	8.23	0.85
	15	19.8	21.85	0.91	8.98	8.15	1.10	16.65	20.47	0.81	6.96	7.96	0.87
	20	19.8	19.67	1.01	8.98	7.63	1.18	16.65	16.98	0.98	6.96	6.54	1.06
Shape Factor	0.5	19.8	18.56	1.07	8.98	7.05	1.27	16.65	15.97	1.04	6.96	6.33	1.10
	0.67	19.8	19.67	1.01	8.98	7.63	1.18	16.65	16.98	0.98	6.96	6.54	1.06
	0.75	19.8	20.11	0.98	8.98	7.7	1.17	16.65	17.35	0.96	6.96	6.62	1.05
Stress Ratio	1.16	19.8	19.67	1.01	8.98	7.63	1.18	16.65	16.98	0.98	6.96	6.54	1.06
	1.10	19.8	19.67	1.01	8.98	7.63	1.18	16.65	16.98	0.98	6.96	6.54	1.06

Validation of Finite Element Modeling

Figures 3.10 and 3.11 show a comparison between the experimental results and finite element model to validate of FEM in predicting the maximum deflection, residual deflection and overall behavior of UHPFRC beams. It is evident from Figure 3.10 that the numerical model is capable of predicting the overall structural response. All test specimens exhibited a similar shape of the deflection–time history curves. The forced response shows a half sine wave followed by the residual deflection during the free vibration phase (after the removal of the drop weight effect). Both maximum deflection and residual deflection decrease with the addition of reinforcement. The experimental ratio of maximum deflection to residual deflection for UH-N and UH-S-0.53% are found to be 2.20 and 2.39, respectively which are very close to the FEM (2.57 and 2.59, respectively). Figure 3.11 also confirms that FEM is in a good agreement with test results. The results from the experimental program and FEM are summarized in Table 3.5.

Table 3.5: Summary of the test and FEM results

Beam Designation	Reinforcement Ratio (ρ)	Maximum Deflection (mm)			Residual Deflection (mm)			Max./Res.	
		Experiment	FEM	% error	Experiment	FEM	% error	Experiment	FEM
UH-N	0	19.80	19.67	0.66	8.98	7.63	15	2.20	2.58
UH-S-0.53%	0.53%	16.65	16.98	1.98	6.96	6.54	6	2.39	2.59

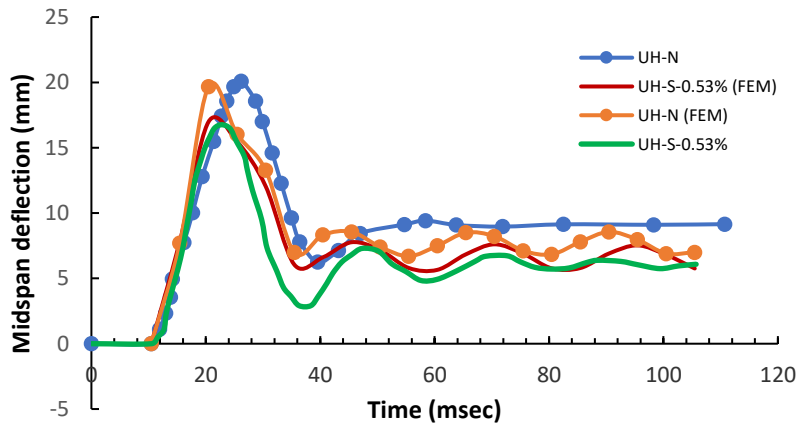


Figure 3.10: Deflection-time history at midspan

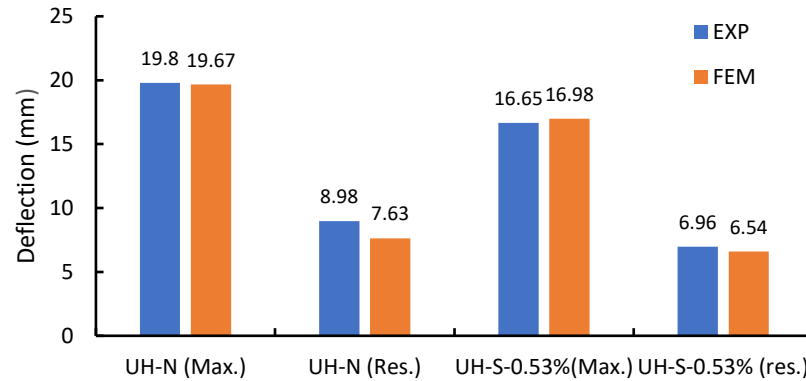


Figure 3.11: Comparison of maximum and residual deflections between experimental program and FEM

The kinetic energy was reported to be 4.2 kJ ($\text{kg}\cdot\text{m}^2/\text{s}^2$) in the literature, which is almost identical to the internal energy found from the FEM model. Figure 3.12 shows the internal energy-time history of UH-N obtained from the FEM.

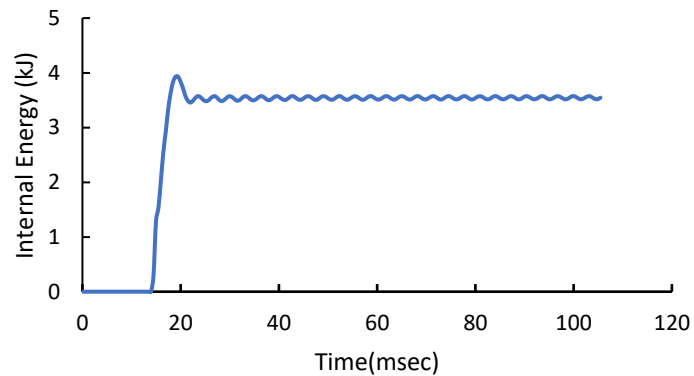


Figure 3.12: Internal energy-time history of whole beam

Figure 3.13 and 3.14 show the damage pattern obtained from FE simulation and the observed crack pattern from experimental program for both UH-N and UH-S-0.53% in tension. It is evident from both figures that FE model is capable of representing the induced damage pattern quite satisfactorily. In both cases, the damage ranges from 24% to 95%. Moreover,

the damage found in UH-S-0.53% is less than UH-N which indicates that the damage in tension decreased with increasing reinforcement ratio.

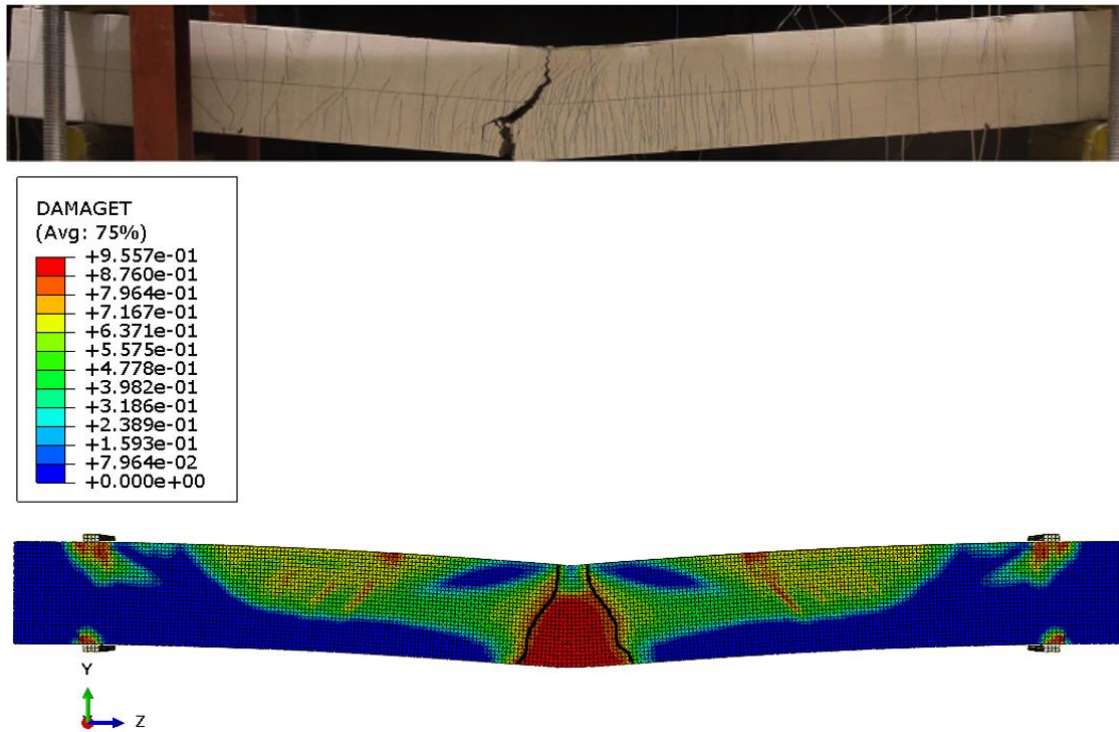


Figure 3.13: Crack Pattern of UH-N (top: experiment Yoo et al. 2015; bottom : FE)

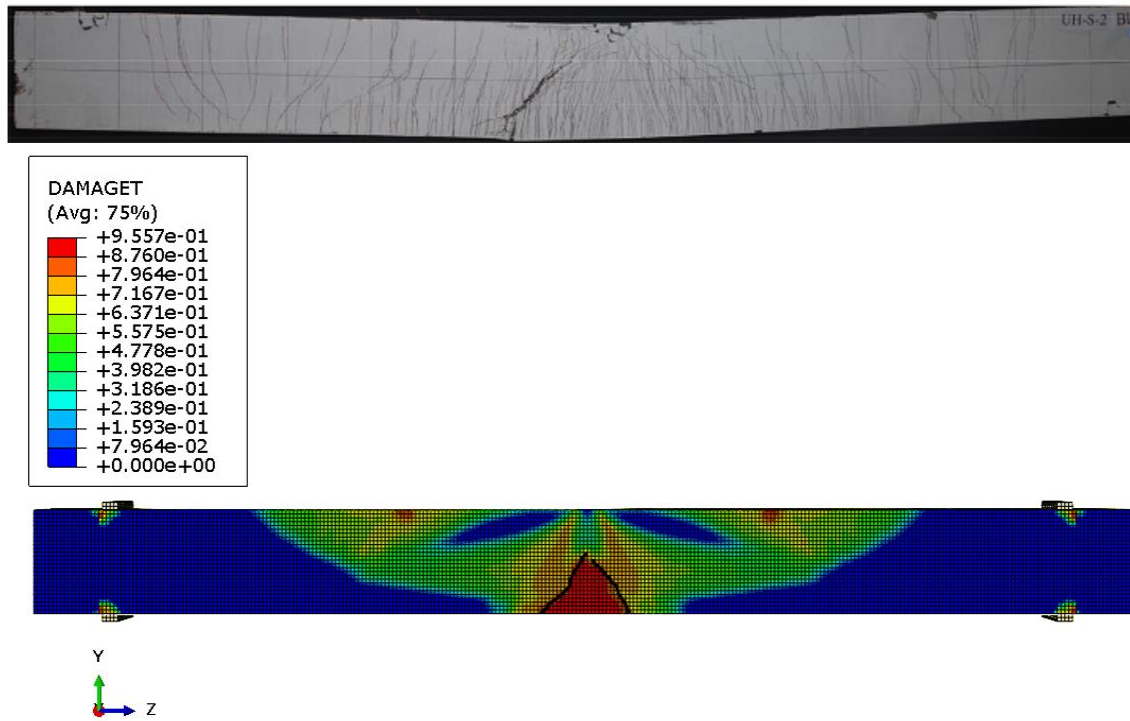


Figure 3.14: Crack Pattern of UH-S-0.53% (top: experiment, Yoo et al. 2015; bottom : FE)

Results and Discussion

The following section presents the impact response of UHPC beams under various parameters using the finite element code. The key parameters were the reinforcement ratio (ρ), and the drop height (h). The specimens were named as UH- ρ S- h . D13 steel bar is used in each beam. The output parameters that have been extracted from the analysis are the mid span deflection, residual deflection, and strain rate for both concrete and steel. The deflection-time history is generated from the numerical analyses for each parametric UHPFRC beam. The effect of the selected geometric parameters on the enhancement of ultimate load carrying capacity and failure mode were also investigated in this study. The cross section of each UHPFRC beam is shown in Figure 3.15.

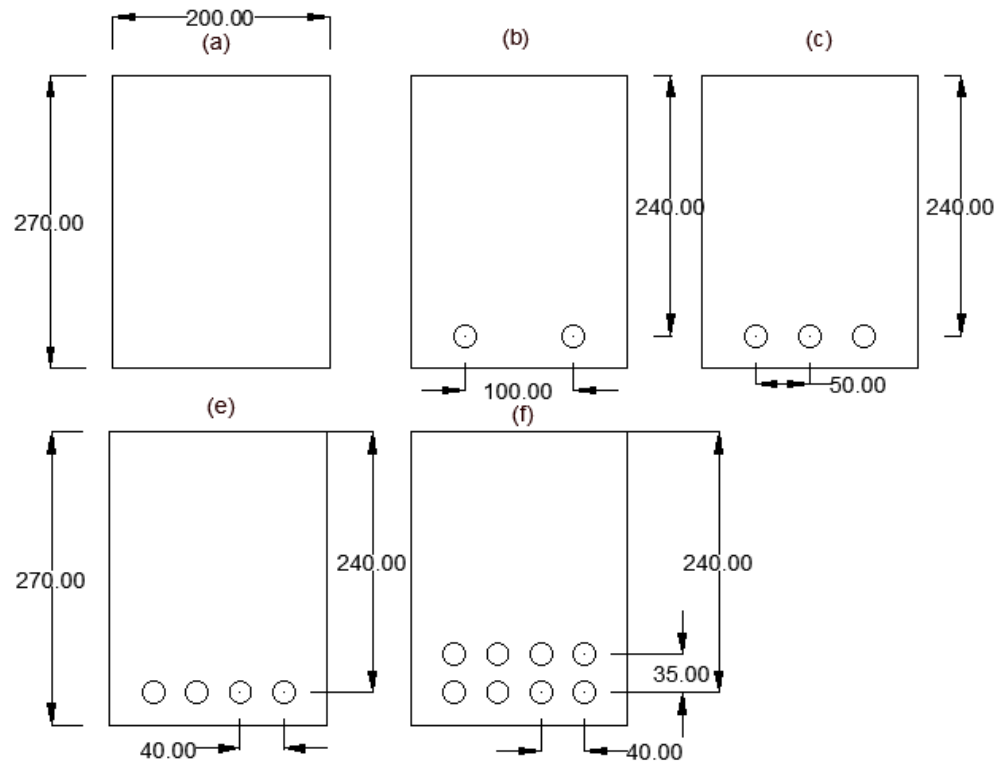


Figure 3.15: Cross Sections of (a) UH-0S-50 (b) UH-0.53S-50 (c) UH-1.05S-50 (d) UH-1.71S-50 (e) UH-2.28S-50

Effect of Reinforcement Ratio

Figure 3.16 (a) shows the numerically obtained deflection time history of UHPFRC beams under impact loading having five different reinforcement ratios (0.0%, 0.53%, 1.05%, 1.71% and 2.28%). In general, it can be said that both the maximum deflection and residual deflection decrease with increasing reinforcement ratio.

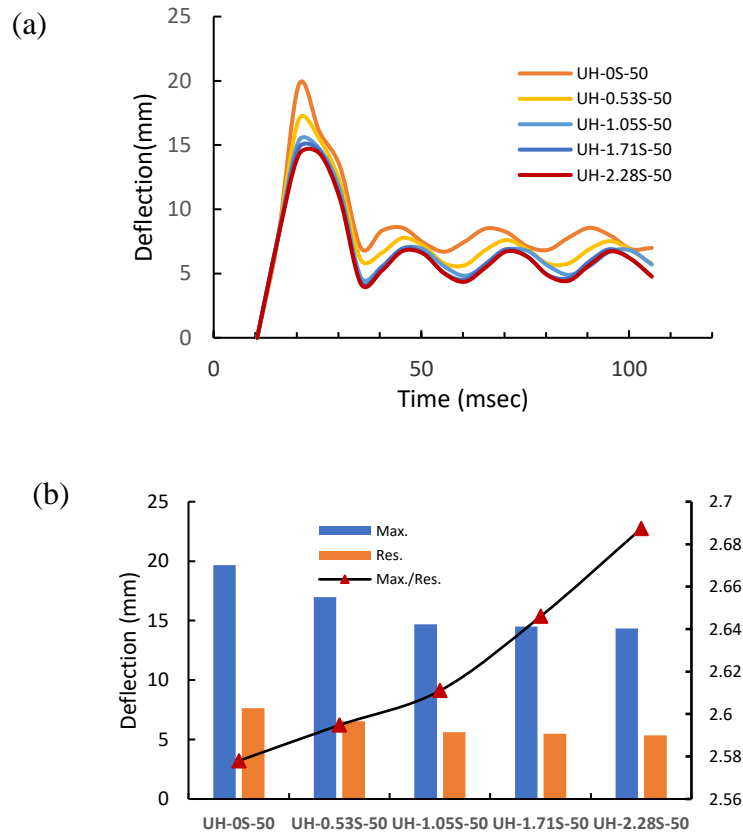


Figure 3.16: (a) Deflection-time history (b) Comparison of maximum and residual deflections according to reinforcement ratio

Figure 3.16 (a) also shows that in the early stages of loading, the response curves follow a typical half sine curve followed by a plastic deformation until the failure strain. It can be observed that ρ had a small effect on the initial slope of the deflection-time history. However, when ρ increases, the maximum deflection point moves to a lower level. Maximum deflection at mid span decreased by 37 % when ρ increased from 0% to 2.28%. In addition, the slope of the inelastic branch of the curves decrease with the increase of ρ .

Figure 3.16 (b) also confirms that the maximum deflection to residual deflection is increased by 3.4% with the increase in reinforcement ratio from 0% to 2.28%. This indicates that a higher reinforcement ratio provides better behavior in terms of deflection recovery.

Effect of Drop Height of Impact Load

The drop height of the impact load was varied from 100 mm to 25 mm to observe the effect on maximum deflection at midspan. The impact velocity was kept constant for all the specimens. Figures 3.17 (a) and (b) depict that for a specific reinforcement ratio, the maximum deflection increases with decreasing drop height. The beam without any reinforcement has experienced 16% more deflection when the drop height decreased to 25 mm. However, the beam with a reinforcement ratio of 1.71% experienced 14.7 % more deflection when the drop height decreased to 25 mm.

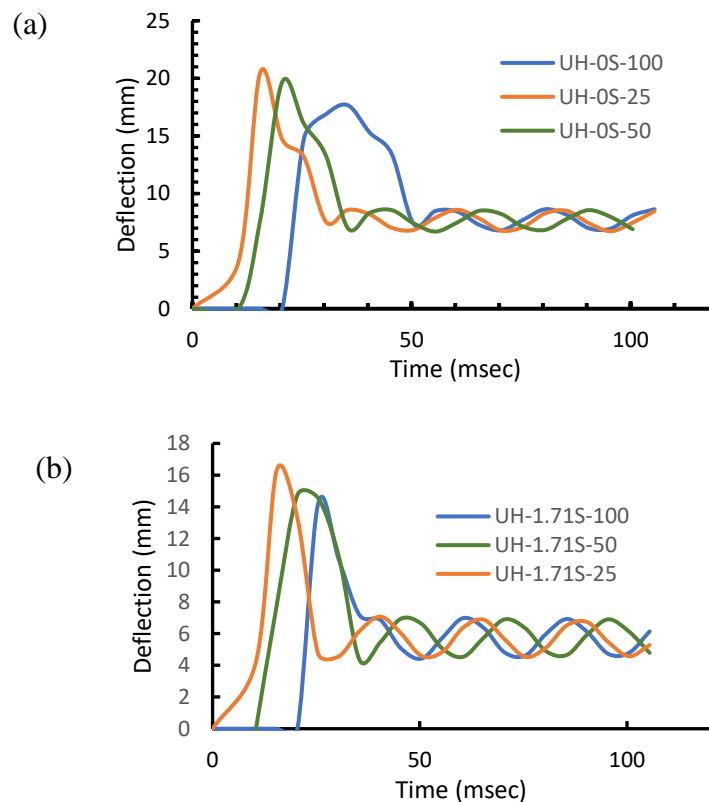


Figure 3.17: Deflection-time history for different drop heights (a) $\rho = 0\%$ (b) $\rho = 1.71\%$

Axial Strain Response under Impact Load

Figure 3.18 represents the axial strain time history of steel reinforcement at the midspan for the simulated beams. It is observed from Figure 3.18 that with the increase of reinforcement ratio, the axial strain of reinforcement bars decreased extensively. However, most of the steel bars were not yielded except for the beam having a reinforcement ratio of 0.53%.

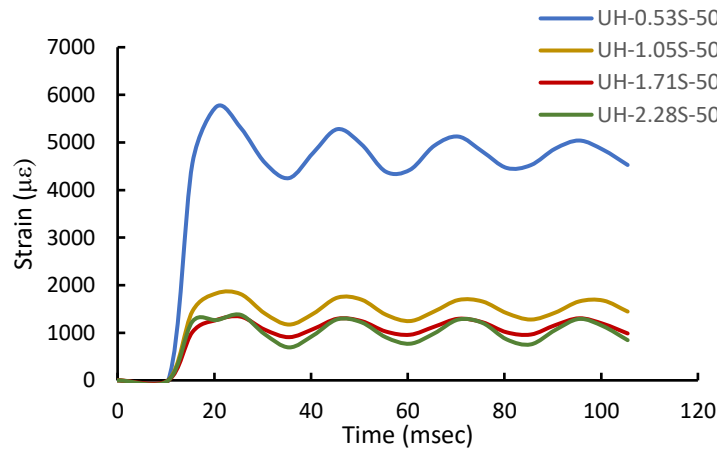


Figure 3.18: Tensile Strain -time history

Figures 3.19 (a) and (b) represent the strain response of the UHPFRC beam having reinforcement ratios of 0% and 2.28% respectively. It is evident from Figures 3.19 (a) and (b) that the addition of reinforcement can significantly decrease the tensile strain of concrete at the bottom surface. The tensile strain decreased by almost 50% when reinforcement ratio increased to 2.28%. In Figure 3.19 (a), the red zone in the bottom surface of UH-0S-50 beam indicates the maximum tensile strain of 0.015 mm/mm which ensures the concrete failure. However, maximum strain of 0.006 is obtained for UH-2.28S-50 which is shown in the red zone of Figure 3.19 (b). The blue zone of Figure 3.19 (a) represents compressive strain of 0.0018 mm/mm to 0.0035 mm/mm, which almost disappears when ρ increases to 2.28%.

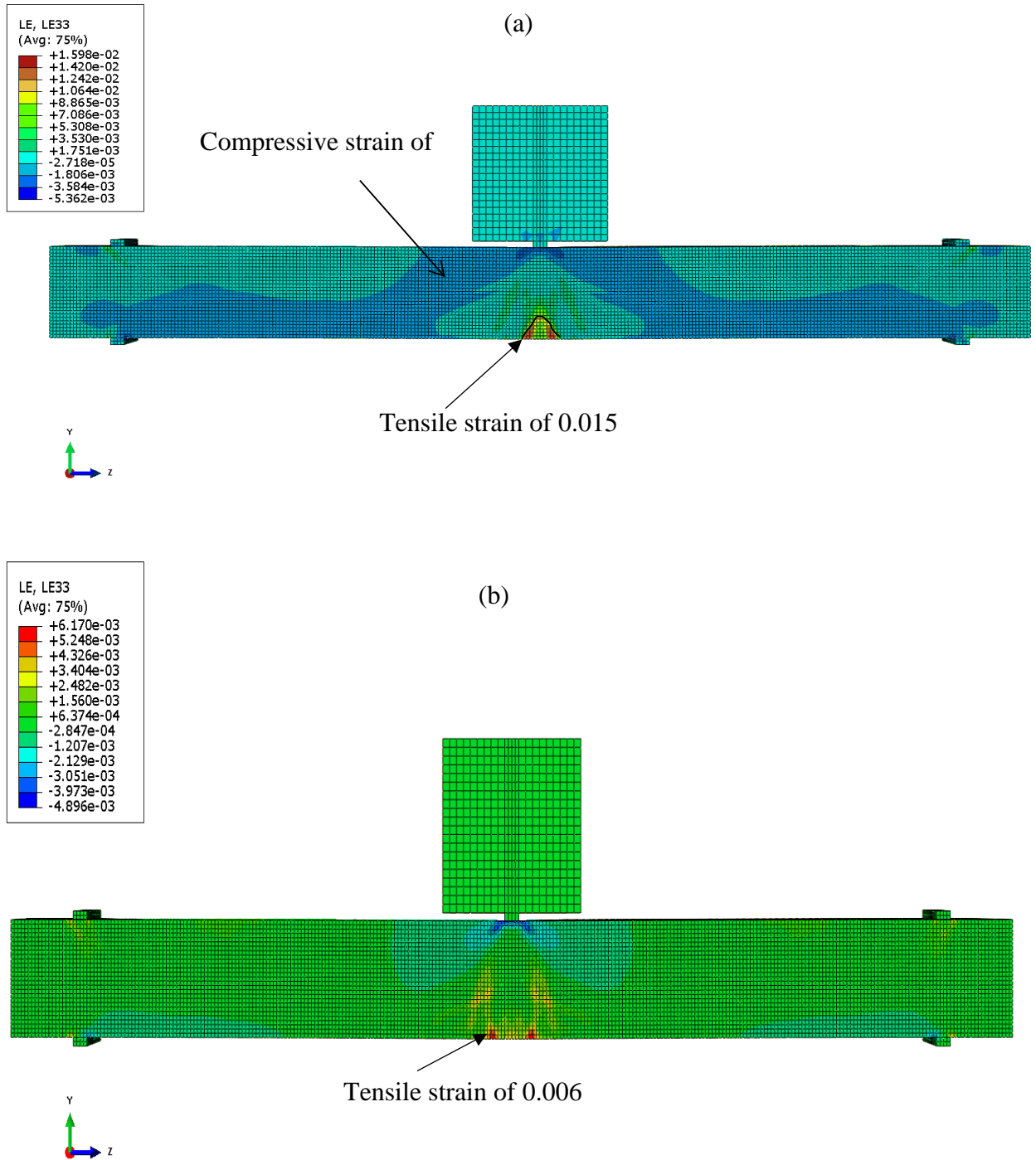


Figure 3.19: Strain response under impact loading (a) $\rho=0\%$ (b) $\rho=2.28\%$

Time lag in Impact Test

It can be seen from Figure 3.20 (a) and (b) that there is a time lag between the impact force and the reaction forces. The time lag can be calculated from the activation time difference between the impact force and the reaction forces. It is evident from the figure that the time lag is nearly 0.5 ms and it is associated with the time required for the stress wave to propagate from the impact point to the reaction plates. The distance between the impact point to the reaction plate is 1250 mm which resulted in an estimated stress wave velocity of 2500 m/s. There is no adequate data regarding the stress wave velocity of UHPC.

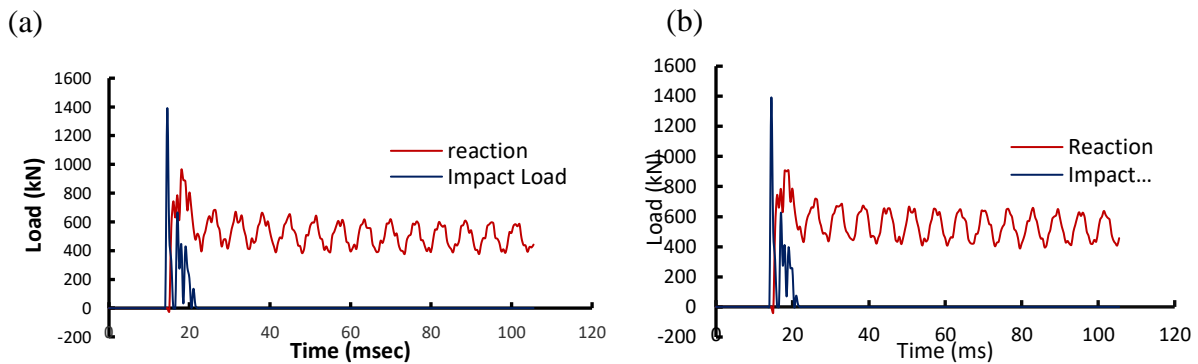


Figure 3.20: Impact load and reaction time history (a) $\rho=1.71\%$ (b) $\rho=2.28\%$

It is evident from Figure 3.20 (a) and (b) that the value of reaction forces is very small or zero when impact force is maximum. Studies showed that when a beam is exposed to impact force by a drop weight, it accelerates the beam and this acceleration causes inertia forces (Banthia et al. 1987; Cotsovos et al. 2008; Saatci and Vecchio 2009). These inertia forces resist the impact load at the very early stage of the impact event (Cotsovos 2010; Cotsovos et al. 2008; Saatci and Vecchio 2009). Since, no reaction or negligible reaction force are found at the time of maximum impact load in this study, so it can be concluded that the impact load was resisted by the inertia forces at the early stage. Figure 3.20 (a) and (b) also confirms that when reaction forces reached the maximum value, the impact load dropped to 30%-40% of the maximum value. Similar behavior is also observed by Pham and Hao 2016.

Conclusions

This study presents a sensitivity analyses based on the numerical simulations of impact response of different UHP-FRC beams. A commonly used software package ABAQUS was used for the simulations. The effect of various key parameters such as mesh size, dilation angle, stress ratio, shape factor, reinforcement ratio (ρ), impact load under various drop heights (h), and the failure phenomena were investigated. From the parametric study, the following conclusions can be drawn:

- The CDP model can be applied for numerical simulation of UHP-FRC beams under low-impact velocity. The sensitivity analyses confirmed that the dilation angle of UHP-FRC has important effect on impact response and dilation angle for UHP-FRC is lower than the NSC. However, shape factor and stress ratio showed no/less impact on the results.
- The numerical model is capable of predicting the deflection-time response, impact load history and damage in UHP-FRC beams.
- The FE model captured the damage pattern of the UHP-FRC. The damage in tension decreased considerably with increases in reinforcement ratio.
- The maximum deflection is found at mid span. Changes in reinforcement ratio have a significant effect on the deflection recovery after impact. It is found that maximum deflection at mid span decreased by 37% when ρ increased from 0% to 2.28%.
- In addition, the tensile strain in steel bars is decreased by almost 50% when reinforcement ratio increased from 0% to 2.28%.
- Moreover, the drop height has considerable effect on mid span deflection. Beam with no reinforcement has experienced 16% more deflection when the drop height decreased to 25 mm. However, for beam with reinforcement ratio of 1.71%, this value is 14.7%.
- A time lag of 0.5 ms was found between the impact force and the reaction forces which resulted in a stress wave velocity of 2500 m/s.
- In this study, no reaction or negligible reaction force was found at the time of maximum impact load which indicates that the impact load was resisted by inertia forces at the early stage. To predict the impact response of UHP-FRC beams more accurately further experimental works should be conducted.

References

- “ABAQUS Analysis User’s Manual.” (n.d.). *ABAQUS version 6.10*, <https://www.sharcnet.ca/Software/Abaqus610/Documentation/docs/v6.10/books/usb/default.htm?startat=pt05ch20s06abm38.html> (Jul. 4, 2019).
- Al-Osta, M. A., Isa, M. N., Baluch, M. H., and Rahman, M. K. (2017). “Flexural behavior of reinforced concrete beams strengthened with ultra-high performance fiber reinforced concrete.” *Construction and Building Materials*, Elsevier Ltd, 134, 279–296.
- Aoude, H., Dagenais, F. P., Burrell, R. P., and Saatcioglu, M. (2015). “Behavior of ultra-high performance fiber reinforced concrete columns under blast loading.” *International Journal of Impact Engineering*, Elsevier Ltd, 80, 185–202.
- Banthia, N., Mindess, S., and Bentur, A. (1987). “Impact behaviour of concrete beams.” *Materials and Structures*, 20(4), 293–302.
- Birtel, V., and Mark, P. (2006). “Parameterised Finite Element Modelling of RC Beam Shear Failure.” *2006 ABAQUS Users’ Conference*, 95.
- Chen, L., and Graybeal, B. (2011). “Modeling Structural Performance of Ultrahigh Performance Concrete I-Girders.” *Journal of Bridge Engineering*, 17(October), 754–764.
- Cotsovos, D. M. (2010). “A simplified approach for assessing the load-carrying capacity of reinforced concrete beams under concentrated load applied at high rates.” *International Journal of Impact Engineering*, Elsevier Ltd, 37(8), 907–917.
- Cotsovos, D. M., Stathopoulos, N. D., and Zeris, C. A. (2008). “Behavior of RC Beams Subjected to High Rates of Concentrated Loading.” *Journal of Structural Engineering*, 134(12), 1839–1851.
- Curbach, M., and Speck, K. (2008). “Ultra high performance concrete under biaxial compression.” *2nd international symposium on UHPC*, Kassel, Germany, 447–84.
- Fehling, E., Leutbecher, T., Roder, F., and Sturwald, S. (2008). “Structural behavior of

UHPC under biaxial loading.” *2nd International Symposium on UHPC*, 569–576.

Fujikake, K., Li, B., and Soeun, S. (2010). “Impact Response of Reinforced Concrete Beam and Its Analytical Evaluation.” *Journal of Structural Engineering*, 135(August 2009), 938–950.

Fujikake, K., Senga, T., Ueda, N., Ohno, T., and Katagiri, M. (2006). “Study on Impact Response of Reactive Powder Concrete Beam and Its Analytical Model.” *Journal of Advanced Concrete Technology*, 4(1), 99–108.

Graybeal, B. (2006). “Material Property Characterization of Ultra-High Performance Concrete.” *Fhwa*, (FHWA-HRT-06-103), 186.

Graybeal, B. (2008). “Flexural Behavior of an Ultrahigh-Performance Concrete I-Girder.” *Journal of Bridge Engineering*, 13(December), 602–610.

Graybeal, B. (2009). “Structural Behavior of a 2nd Generation UHPC Pi-Girder.” *FHWA Publication No. of this TechBrief: FHWA-HRT-09-069*, (October), 1–4.

Grünberg, J., Lohaus, L., Ertel, C., and Wefer, M. (2008). “Multi-axial and fatigue behavior of ultra-high performance concrete (UHPC).” *Proceedings of the 2nd International Symposium on Ultra-High Performance Concrete*.

Kmiecik, P., and Kamiński, M. (2012). “Modelling of reinforced concrete structures and composite structures with concrete strength degradation taken into consideration.” *Archives of Civil and Mechanical Engineering*, 11(3), 623–636.

Lee, J., and Fenves, G. L. (1998). “Plastic-Damage Model for Cyclic Loading of Concrete Structures.” *Eng Mech*, 124(8), 892–900.

Li, J., Wu, C., and Hao, H. (2015). “An experimental and numerical study of reinforced ultra-high performance concrete slabs under blast loads.” *Materials and Design*, Elsevier Ltd, 82, 64–76.

Lubiner, J., Oliver, S., Oller, S., and Onate, E. (1989). “A plastic-damage model for

concrete.” *International Journal of Solids and Structures*, 25(3), 299–326.

Nasrin, S., and Ibrahim, A. (2018). “Finite-element modeling of UHPC hybrid bridge deck connections.” *International Journal of Advanced Structural Engineering*, 10(3), 199–210.

Ngo, T., Mendis, P., and Krauthammer, T. (2007). “Behavior of Ultrahigh-Strength Prestressed Concrete Panels Subjected to Blast Loading.” *Journal of Structural Engineering*, 133(11), 1582–1590.

Pham, T., and Hao, H. (2016). “Impact Behavior of FRP-Strengthened RC Beams without Stirrups.” *Journal of Composites for Construction*, 20(2), 1–13.

Safdar, M., Matsumoto, T., and Kakuma, K. (2016). “Flexural behavior of reinforced concrete beams repaired with ultra-high performance fiber reinforced concrete (UHPFRC).” *Composite Structures*, Elsevier Ltd, 157, 448–460.

Shao, X., Yi, D., Huang, Z., Zhao, H., Chen, B., and Liu, M. (2013). “Basic Performance of the Composite Deck System Composed of Orthotropic Steel Deck and Ultrathin RPC Layer.” *Journal of Bridge Engineering*, 2(May), 417–428.

Vecchio, S. S. and F. J. (n.d.). “Effects of Shear Mechanisms on Impact Behavior of Reinforced Concrete Beams.” *Structural Journal*, 106(1).

Wang, Y. B., Liew, J. Y. R., Lee, S. C., and Xiong, D. X. (2016). “Experimental study of ultra-high-strength concrete under triaxial compression.” *ACI Materials Journal*, 113(1), 105–112.

Williams, E. M., Graham, S. S., Reed, P. a, and Rushing, T. S. (2009). *Laboratory Characterization of Cor-Tuf Concrete With and Without Steel Fibers. Engineer Research and Development Center.*

Yoo, D. Y., Banthia, N., Kim, S. W., and Yoon, Y. S. (2015). “Response of ultra-high-performance fiber-reinforced concrete beams with continuous steel reinforcement subjected to low-velocity impact loading.” *Composite Structures*, Elsevier Ltd, 126, 233–245.

Yuan, J., and Graybeal, B. (2011). “Structural Behavior of Ultra-High Performance Concrete Prestressed I-Girders.” *Engineering Structures*, 1(6), 228–235.

Chapter 4: Finite Element Analysis of Confined High Strength Concrete Bridge Columns with Opposing-Spiral Reinforcement

“Finite element analysis of confined high strength concrete bridge columns with opposing-spiral reinforcement”, published in *International Journal of Structural Engineering*, July 2018, Volume 9, Issue 2, pp 101–115

Abstract

The spiral reinforcement is a very common technique used for reinforcing columns in active seismic regions due to its high ductility and high ability of energy absorption. This paper presents a nonlinear finite element analysis of high-strength concrete confined with opposing circular spiral reinforcements. The results are compared with previously tested small-scale concrete columns made with the same technique under monotonic axial loads. The proposed technique is developed to improve strength and ductility of concrete columns confined with conventional spiral systems. The finite element (FE) analysis results have showed that the proposed model can predict the failure load and crack pattern of columns with reasonable accuracy. Beside this, the concrete plasticity damage showed very good results in simulating columns with opposing spirals. The developed FE model is used to conduct a study on the effect of spiral spacing, γ (ratio of the core diameter to the whole cross section diameter) and compressive strength on behavior of circular spiral reinforced concrete column confined with opposing circular spiral reinforcements. The results of the parametric study demonstrated that for the same spacing between spirals and same strength of concrete, increasing γ will result into increasing the failure load of the column. It is also observed from the study that the ductility of the studied columns is not affected by changing the value of γ . In addition, a correlation between the γ factor, three different compressive concrete strength, and the spacing of opposing spirals was developed in this paper.

Keywords: Finite element model; Column; Spiral reinforcement, Spiral spacing; Confined concrete strength.

Introduction

Proper lateral confinement systems such as steel stirrups, steel jackets, and composite materials increase axial capacity of concrete columns. The axial behavior of confined concrete (stress-strain) under axial monotonic loads is influenced by the confinement configuration, and by the effectiveness of confinement material (Wu et al. 2006). Lateral steel confinement produces a triaxial state of stress which postpone concrete failure under axial loads and in consequence improves the overall ductility. The effectiveness of the lateral resistance is determined based on the method of confinement used. The most common methods of confinement recommended by the ACI 318 is to use steel spirals, which proven to be a very effective means in reinforced concrete (RC) columns. The minimum spacing of spirals specified by the ACI is 25 mm to ensure constructability and concrete flowability. Very limited data are available on the use of opposing spiral systems on confining concrete columns and its simulation using the finite element method.

Hindi et al. (2005) tested columns constructed with two steel opposing spirals as a replacement of conventional single steel spiral, and that could be operated to increase the axial columns behavior and to ease columns construction. The opposing spirals could be designed and constructed with conventional spacing recommended by the ACI. The benefits of using opposing spirals is the doubling of the volumetric confinement ratio of the lateral reinforcing system. The opposing spiral configuration could be used in areas where constructability is a question. The key point of opposing spiral configuration is to preserve same volumetric confinement ratio with double the pitches. One more benefit from using the opposing spirals is to maintain column axial capacity under the increased spiral spacing and that would be very helpful in the highly congested beam-to-column joints.

Hindi et al. (2005) reported a study on reinforced concrete columns with opposing-spiral confinement technique. Small-scale normal weight concrete columns were experimentally tested under pure axial load. The experimental results showed, when comparing the conventional single-spiral confined columns to the opposing-spiral columns with the same volumetric confinement ratios, similar behavior in strength and ductility between the specimens were found.

Multiple types of horizontal confinement systems have been reported such as: hoops, welded-wire mesh, high-strength strands, carbon FRP spirals and hoops, and conventional spirals (Afifi et al., 2015; Budek, et al. 2002; Tan and Yip 1999; Tanaka and Park, 1993; Tavio et al. 2011; Wu and Wei, 2014). These tests were conducted for various reasons: to verify code adequacy, to develop innovative methods and ultimately, and to upsurge the fracture energy of columns. Ding et al., (2014) studied the structural behavior of concrete-filled steel tube columns under monotonic load. The steel tubes were reinforced laterally using steel spiral stirrups and some specimens were internally stiffened. The results were used to validate the FEM and to extend the parametric study where an approach was established to predict the bearing capacity of such columns.

Liang et al., (2014) conducted various full-scale tests on the axial performance of short steel and concrete columns confined with multiple confinement systems. It was reported that composite columns with several interlocking hoops showed improved capacity compared to conventional reinforced concrete column with multiple spirals. Many theoretical RC stress-strain confinement models have been developed for columns confined with steel spiral reinforcements (Mander et al. 1989). Mander, et al., (1989) is one of the common models used in the current study to be implemented in the finite element code.

Marvel et al., (2014) reported the results of high-strength reinforced concrete columns confined using opposing-spiral technique and subjected to monotonic axial loads, and the conclusion of the study recommended that columns confined with opposing spirals having similar volumetric confining ratios as conventional single spirals had a similar ultimate strength and an increased ultimate strain and ductility. On average, the opposing spiral confined columns obtained 120% of the ultimate strain of its conventional single-spiral. Counterpart, and finally it was found that columns confined with opposing spirals with double the confining reinforcement steel ratio displayed noteworthy improvement on average of 139% increase in the strength of its conventional single-spiral counterpart. Figure 4.1 shows the different spiral configuration used in this study.

The goal of this paper is to numerically investigate the axial behavior of multiple-strength concrete columns using the opposing spiral confinement technique and to compare the results with experimentally tested columns. The finite element simulations were performed using the comprehensive finite element code ABAQUS. In addition, a parametric study was performed on the effect of spiral spacing, γ (ratio of the core diameter to the whole cross section diameter) and compressive strength on behavior of circular spiral reinforced concrete column confined with opposing (opposing) circular spiral reinforcements. The following sections present the description of the experimental tested specimens and the finite element model.

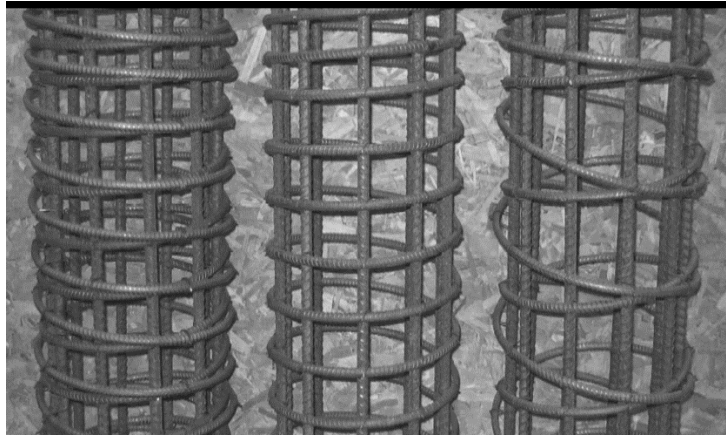


Figure 4.1: Specimen comparison, opposing spiral spacing of (S), single spiral spacing of (S), opposing spiral spacing of (2S) (Marvel 2014).

Experimental Program

The experimental program consisted of twenty-one small-scale reinforced high-strength concrete circular columns with various longitudinal reinforcement ratios and four different confinement reinforcement ratios. The columns were subjected to monotonic axial load to investigate the effect of the opposing spiral on the axial capacity. All columns designed to satisfy ACI 318 requirements. Seven of the twenty-one specimens were constructed using conventional single spirals and served to compare against the proposed opposing spiral configuration. The remaining fourteen columns were prepared using the opposing-spiral confinement system. The dimensions of all specimens were the same, and the variables were the longitudinal steel ratio and spiral spacing. The outer diameter, core diameter and the length of columns were 350 mm, 250 mm 1000 mm respectively. 8, 10, 12, 14–U15.9 mm (No. 5) main steel bars were used and spread over the core. Longitudinal steel ratios of 0.016,

0.020, 0.024 and 0.028 were considered in the study. The confining spiral used was U9.5 mm (No. 3) with four bases's spiral spacings of 40, 50, 55, or 60 mm, covering the allowable spiral spacing set in ACI 318. Figure 4.2 shows the Schematic representation of specimen details. More details about the columns testing matrix could be found on Marvel et al., (2014)

Finite Element Modelling

This section presents a description of the details of the finite element modeling and the material models for concrete, steel, and spirals which were implemented into the code. The numerical simulations were performed using ABAQUS code, which is a general FE analysis package with the capability of capturing the nonlinear behavior of materials under different loading combinations. There are two different types of analysis in ABAQUS; implicit and explicit. The explicit analysis option was employed in this paper to predict the axial capacity of high strength columns reinforced laterally with opposing spirals. The reason of choosing the explicit technique is to avoid the convergence problems associated with highly heterogeneous materials such as concrete. Mesh sensitivity analysis was conducted to select the most efficient element size, where solid elements were chosen to represent concrete and truss elements were selected for longitudinal and lateral steel reinforcements.

Material Properties

Twenty-one columns were cast in two separate placements – 19 of the columns were cast during the first concrete batch and 2 were prepared with the second (Marvel et al., 2014). The aggregates had a maximum aggregate size of 19 mm with a concrete compressive strength f_{oc} of 70 MPa with an average 28-day compressive strength of 67.3 MPa.

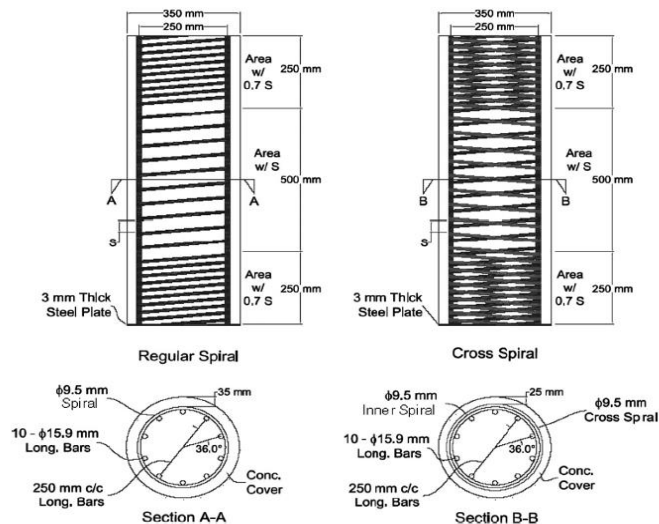


Figure 4.2: Schematic representation of test specimen (Marvel et al. 2014).

Steel reinforcing bars

The longitudinal steel bars and the opposing spirals were modelled as elastic perfectly plastic materials in both compression and tension. The stress-strain behavior of steel bars is shown in Figure 4.3. The Truss element was used in ABAQUS to simulate the steel members. The stress-strain related parameters such as steel yield strength, elastic modulus and tensile strength were obtained from the experimental study conducted

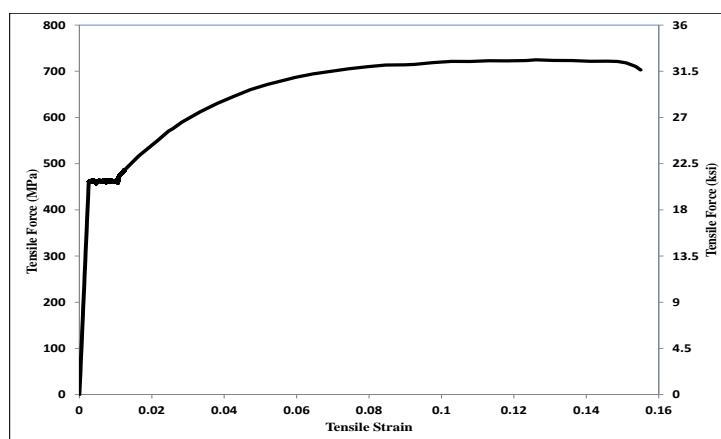


Figure 4.3: Stress-Strain curve of reinforcing steel bars and spirals.

Concrete

C3D8R are solid elements and best fit in simulating the considered columns. The nonlinear concrete behavior is simulated independently. The rebar-concrete constraints normally

modeled as full bond. The Concrete Damaged Plasticity (CDP) Model developed by (Lubiner et al., 1989) and extended by Lee and Fenves, (1998) was used in this study to predict the behavior of columns. The CDP concrete constitutive model has the capability to simulate the elastic-plastic response of concrete considering tension-cracking and compression-crushing.

Under axial tension, concrete behavior starts linearly until the ultimate stress. The failure stress represents the start of micro-cracking, and after this point a softening behavior became dominant. On the other side, under pure axial compression load, stress-strain relationship is considered linear up to a value of 0.45 of the ultimate concrete stress. In the plastic region, stress is typically described by strain hardening followed by strain softening till concrete reaches the failure strain. The CDP parameters implemented in ABAQUS are shown in Table 4.1 and Figures 4.4 and 4.5.

Table 4.1. Parameters Used for the Concrete in Plastic Damage Model.

Young's Modulus (MPa)	Poisson's Ratio	Dilation		f_{bo}/f_{co}	κ
		Angle, ψ Degree	Eccentricity		
Varies	0.18	36	0.1	1.16	0.67

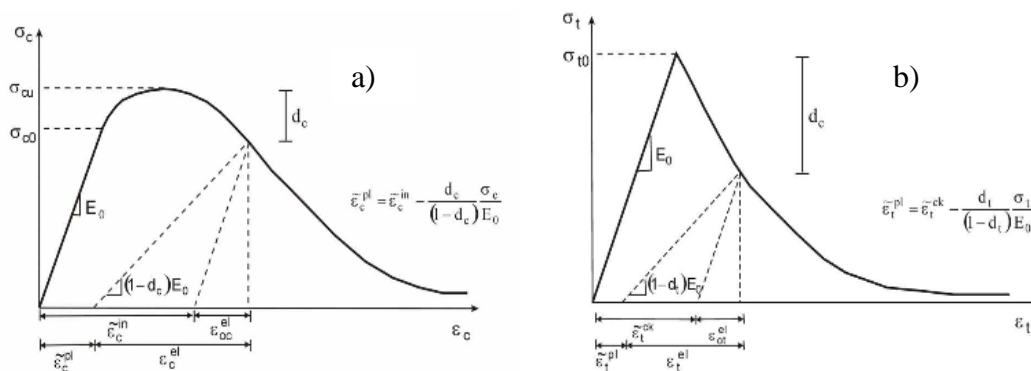


Figure 4.4: σ - ϵ in compression and σ - ϵ in tension for CDP model [ABAQUS]

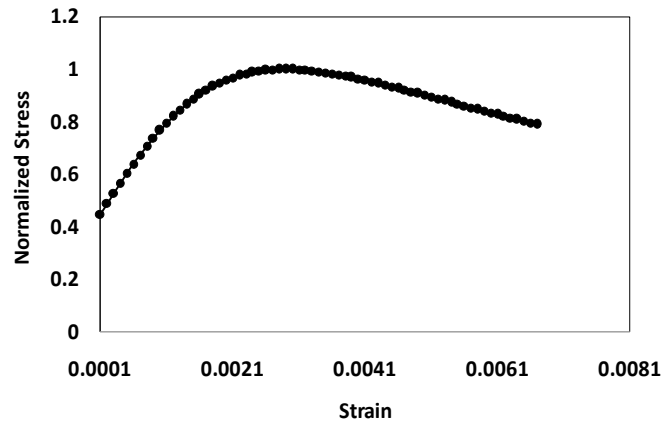


Figure 4.5: The compression concrete inelastic stress-strain curve.

Results and Discussions

Verification of the Finite Element Model

The reinforced concrete FE models developed in this paper were built using ABAQUS/Standard. In the finite element simulations, a steel rigid loading plate was assumed at the top and at the bottom of the column to avoid stress concentration associated problems. The concrete and steel plate for all columns, were modelled using 8-node reduced integration 3D solid elements. A structured meshing option with a mesh size of 40 mm was adopted, and the mesh for concrete and the steel is shown in Figure 4.6. Smaller mesh sizes were also studied, and the results were consistent with almost constant after decreasing the mesh size smaller than 40 mm. A surface-to-surface constraint was used to couple steel and concrete with no relative displacement between them. The modeling of softening behavior, and the whole simulation was performed under displacement control, where a small increment of displacement was applied at the top of the loading plate. The incremental-interactive method available in ABAQUS was used to simulate concrete and steel nonlinearities. The FEM results were compared with the results found in Marvel et al. (2014). Table 4.2 shows the column cases used in the finite element verification. The 3-D view of the meshing of the columns is shown in Figure 4.6.

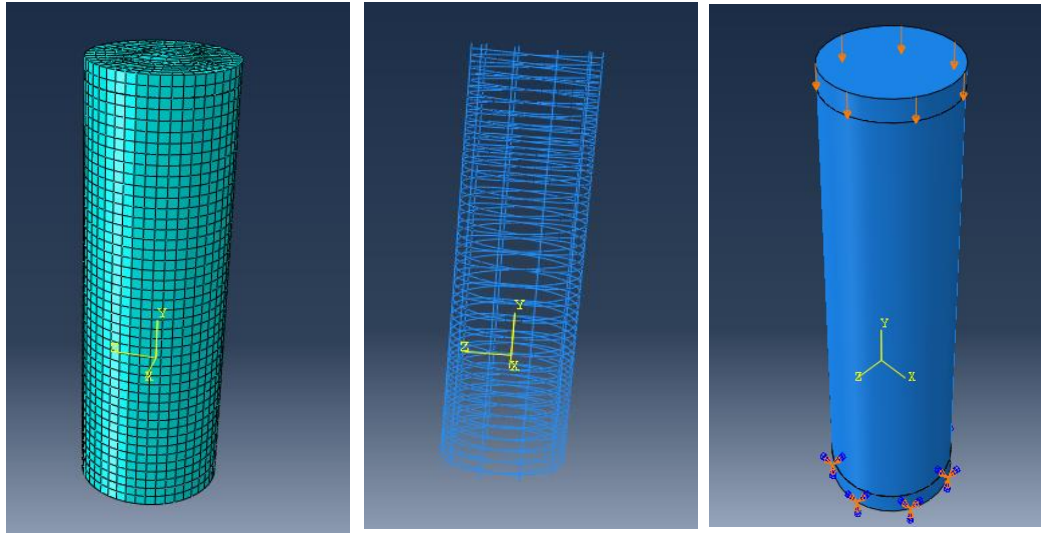


Figure 4.6. The FE mesh for concrete, the reinforcing steel, and the boundary conditions.

Figure 4.7 shows the comparison between the developed finite element model and the results for all the cases shown in Table 4.2.

Table 4.2. Column samples used in the finite element verification

Specimen	Spiral Type	Effective length (mm)	Spiral Spacing (mm)	Longitudinal Steel Ratio (ρ_l)	Transvers Steel Ratio (ρ_s)
50X-8	Opposing	1000	50	0.016	0.04
50X-10	Opposing	1000	50	0.02	0.041
50S-8	Regular	1000	50	0.016	0.021
40X-10	Opposing	1000	40	0.02	0.052
55X-10	Opposing	1000	55	0.02	0.038
60X-10	Opposing	1000	60	0.02	0.034

Six reinforced columns were modeled-using ABAQUS and compared with the test results from Marvel et al. (2014). The modelled columns have different longitudinal and lateral

reinforcement ratios as shown in Table 2. All specimens were compared based on the axial stress-strain history. The comparison shows that the developed FEM is capable to capture the behavior of the columns with the opposing spirals technique. As shown in Figure 4.7, the stress-strain history between the FEM and experimental results are very close in terms of the ultimate stress and the failure strain, except for the case of using single spiral (50-8S). The initial stiffness of the FE model is in very good agreement with the experiments, while the softening behavior of the FE model over predicts or under predict the behavior at the failure point. Figure 4.8 shows the concrete damage depicted from one of the tested columns, the FEM shows that the maximum principle strain is reached at the middle third of the column height and shows the same behavior as the real damaged column. The opposing spiral confinement added more lateral confinement pressure whereas pushed the concrete to be failed through an inclined shear surface.

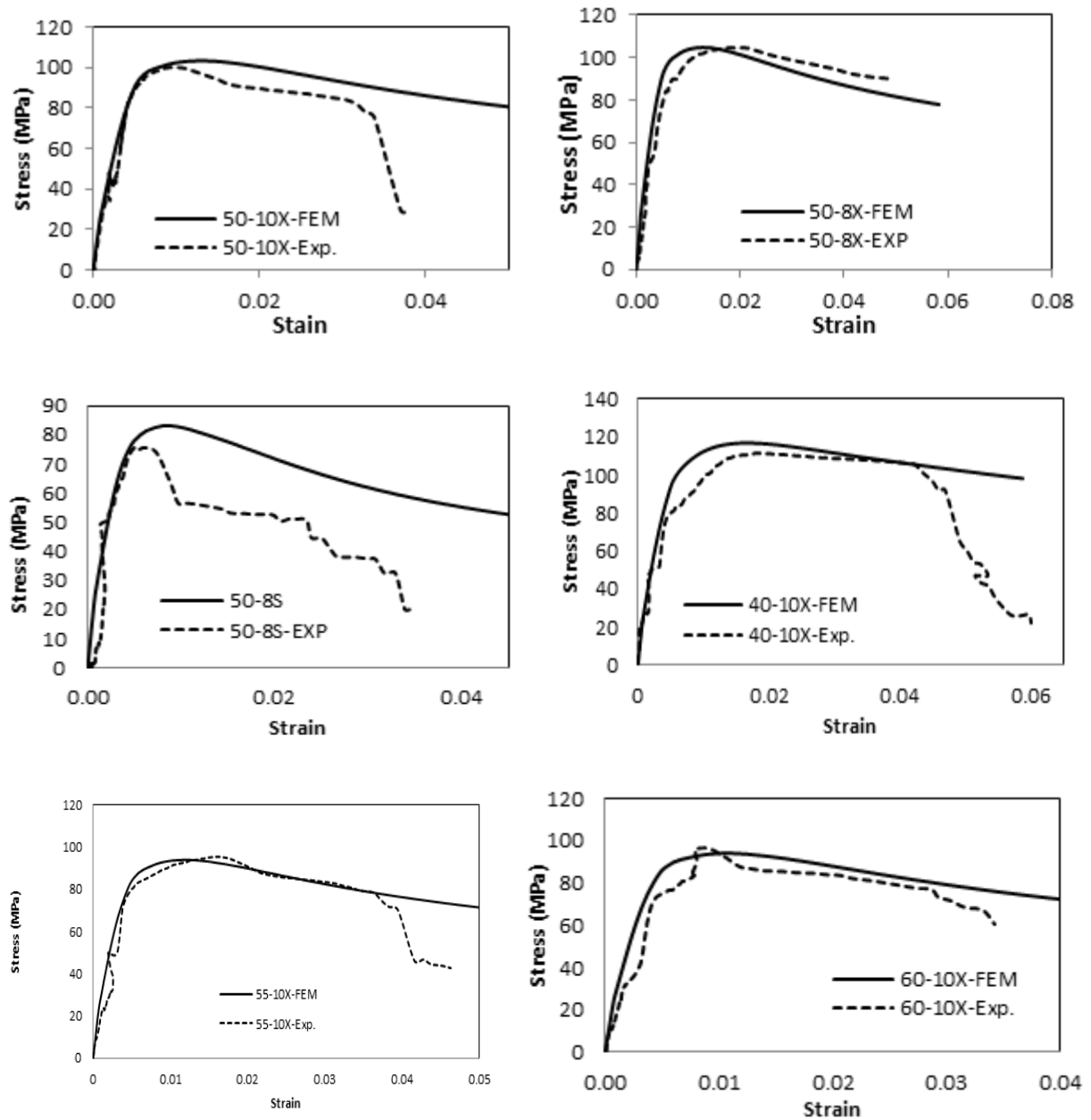


Figure 4.7: Comparison of Stress-Strain behavior between the experimental and the FEM.

Parametric Study

The following section presents the response of columns under various parameters with the opposing spirals using the finite element code. The key parameters were the concrete compressive strength, the spiral spacing, and the longitudinal reinforcement ratios. The specimens were named as S-X γ -C as where S, X, γ and C represent spacing of opposing spiral in mm, Spiral type, the ratio of the core diameter to the whole cross section diameter, and the concrete compressive strength, respectively. The output parameters that had been

extracted from the analysis are the axial confined stress, f'_{cc} , and average axial strain, ϵ_{au} . The average axial strain was calculated by dividing the total axial displacement in the axial direction by the total length of the column. The axial stress versus axial strain curves are then generated from the numerical analyses for each parametric column. The effects of the selected geometric parameters on the enhancement of ultimate load carrying capacity and ductility of the concrete columns were also investigated in this study.

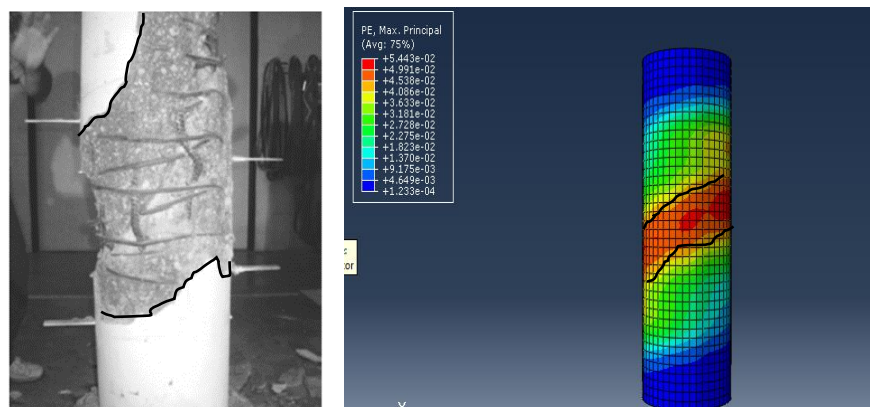


Figure 4.8. Comparison of concrete damage between the experimental and the FEM.

Axial stress versus axial strain response

Figures 4.9 shows the numerically obtained axial strains plotted against average longitudinal strain of the concentrically loaded opposing spiral circular concrete columns having two different compressive strength 30 MPa (Fig. 9a) and 100 MPa (Fig. 9b). The axial stress was calculated by dividing the incremental axial load by the columns' cross-sectional area assuming that longitudinal reinforcement has no effect in carrying compressive load.

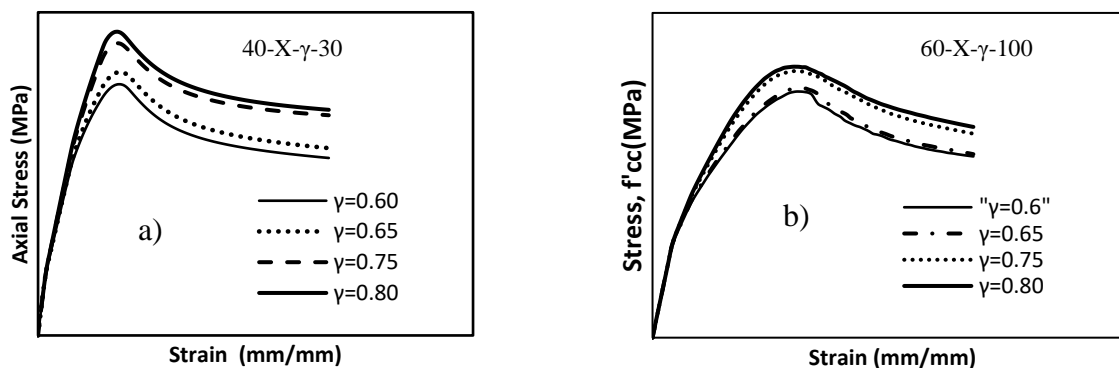


Figure 4.9: Axial Stress vs Axial Strain response for different γ .

Figure 4.9 also shows the comparison of axial confined stress versus axial strain response of opposing spiral columns having different γ . In the early stages of loading, up to the ultimate concrete compressive strength (f'_c), the response curve follows the typical curve of conventional unconfined concrete columns under axial load and then it experienced a plastic deformation till the failure strain.

It can be observed that γ had a small effect on the initial tangent modulus of the stress-strain history. However, as the γ increased, the ultimate stress point moved up to a higher stress level. In addition, the slope of the inelastic branch of the stress-strain curves increased with the increase of γ . No difference in the ultimate load was found between γ equals 0.60, and 0.65 however there is a 20% difference in the ultimate load when γ changes from 0.65 to 0.75. Figure 4.9 also confirms that for a specific strength of concrete, all the columns reached the ultimate stress at almost same strain even though γ was different. It can be concluded that for the same spacing between the spirals and same concrete strength, increasing γ results into increasing the failure load of the column. In addition, the ductility of column is not affected much by changing γ . Figure 4.10 shows the correlation between opposing spiral spacing and the ultimate load for three concrete strengths; 30, 50, and 100 MPa and various γ values. It can be seen that increasing the γ value, with decreased spacing, increases the ultimate load.

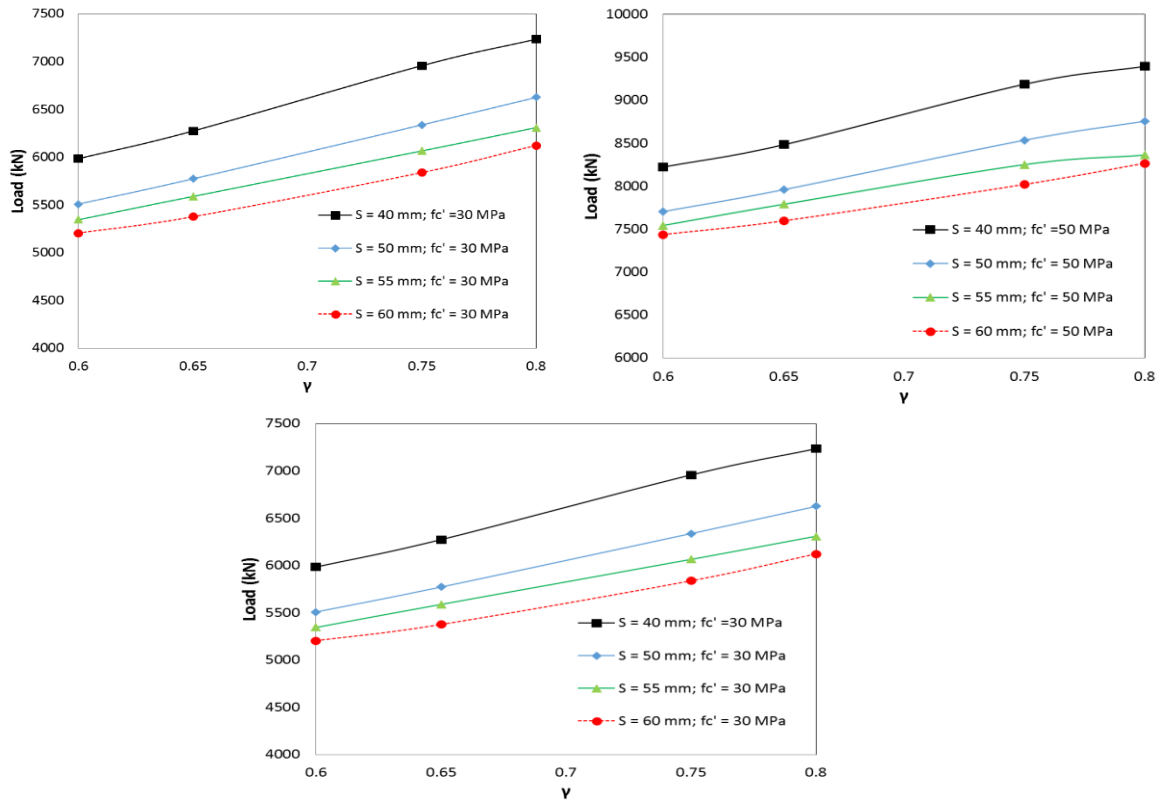


Figure 4.10: Axial load vs γ for different concrete strength.

Effect of Spiral Spacing

Spiral spacing is considered a major factor in the axial behavior of concrete columns. When spiral spacing is increased, the volumetric confinement reinforcement ratio is decreased which reduces its load carrying capacity and ductility. A study has been conducted to find out the efficiency of opposing spiral columns over conventional single spiral columns having same spiral spacing. The confined compressive strength of conventional single spiral columns are found by the analytical model proposed by Mander et al. (1988). The confined compressive strength f'_{cc} is based on tri-axial tests performed by Schickert and Winkle (1977) and is shown in Equation 4.1 to 4.4.

$$f'_{cc} = f'_{co} \left(-1.254 + 2.254 \sqrt{1 + \frac{7.94 f'_l}{f'_{co}}} - 2 \frac{f'_l}{f'_{co}} \right) \quad (4.1)$$

where, f'_l is the effective lateral confining stress on the concrete core

$$f'_l = \frac{1}{2} k_e \rho_s f_y h \quad (4.2)$$

f_{yh} is the yield strength of transverse reinforcement and K_e is the confinement effectiveness coefficient.

$$k_e = \frac{1 - \frac{s'}{2ds}}{1 - \rho_{cc}} \quad (4.3)$$

$$\rho_s = \frac{4A_{sp}}{d_s s} \quad (4.4)$$

Here, s' = clear vertical spacing between spirals, ds = diameter of spiral between bar centers, ρ_{cc} = ratio of area of longitudinal steel to area of core, s = center-to-center spiral pitch, and A_{sp} = area of transverse reinforcement bar.

Figure 4.11 shows the effect of spiral spacing on confined concrete stress for different strength of concrete. Though the analytical model proposed by Mander et al. (1989) over predicts the confined concrete stress for every column but it follows the same trend as the FEM solution. It is also evident from Figure 11 that the increase in spiral spacing result in loss of ultimate confined compressive strength for each type of concrete columns. The results obtained from the analytical and FE model are in a good an agreement for both values of γ as shown in Figure 4.11. However, the analytical model developed by Mander et al. (1989) is overestimated the failure capacity of the column when the value of γ dropped from 0.8 to 0.65. This is due to that the FE model developed considers the effect of the confinement of the core represented by γ which reflects the actual performance of the confined concrete column.

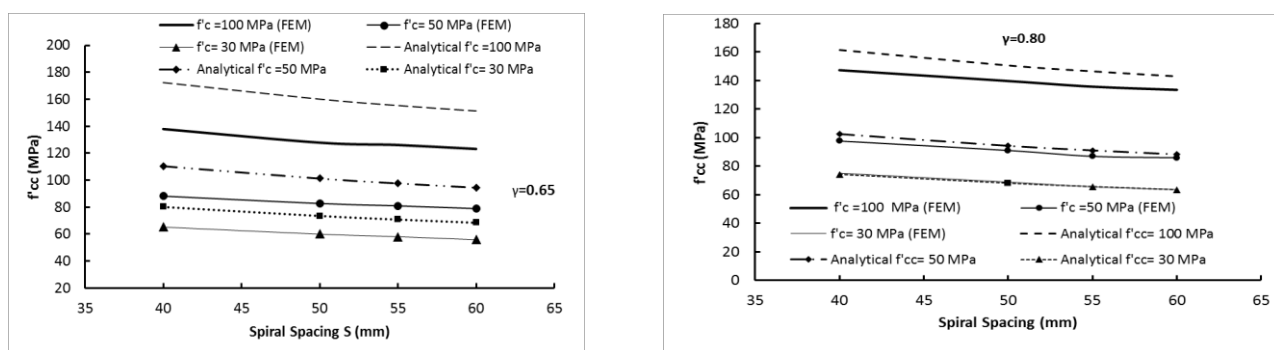


Figure 4.11. Confined Axial Stress vs Spiral Spacing for different f'_c

Conclusions

This paper presents the results of finite element modeling of concrete columns reinforced with opposing spirals in a way to increase the lateral confinement pressure, which in

consequence provide more ultimate axial load capacity. The proposed technique offers new generation of columns that have more ductility and more energy absorption characteristics. The finite element code Abaqus is used on the numerical simulations and the concrete and steel nonlinearity behavior is considered in the study. Based on this study the following conclusions can be drawn:

- The damage plasticity model showed very good potential in simulating the axial behavior of reinforced concrete columns reinforced with opposing spirals in terms of ultimate load and failure strain predictions.
- The developed finite element modeling of circular spiral reinforced concrete columns is capable of predicting the failure capacity, damage pattern and ductility with a reasonable accuracy.
- The results from the parametric study demonstrated that for the same spacing between the spirals and same strength of concrete, increasing γ results into increasing the failure load of the columns.
- The ductility of columns is not affected by changing the ratio of core diameter to the total column diameter (γ).
- A relationship between the opposing spiral spacing and the confined compressive strength has been developed for different concrete compressive strength.

References

Abaqus, Dassault Systèmes Americas Corp., Waltham, MA, USA.

ACI Committee 318. (2005) 'Building code requirements for structural concrete (ACI 318) and commentary (318R)', *Farmington Hills (MI): American Concrete Institute*; p. 430.

Afifi, M. Z., Mohamed, H. M., Chaallal, O., Benmokrane, B. (2015) 'Confinement Model for Concrete Columns Internally Confined with Carbon FRP Spirals and Hoops', *Journal of Structural Engineering*, 141(9), p. 4014219. doi: 10.1061/(ASCE)ST.1943-541X.0001197.

Budek, A. M., Priesley, M. J. and Lee, C. O. (2002) 'Seismic Design of Columns with High-Strength Wire and Strand as Spiral Reinforcement', *ACI Structural Journal*, 99(5), pp. 660–670.

Ding, F. X., Fang, C., Bai, Y., Gong, Y.Z. (2014) 'Mechanical performance of stirrup-confined concrete-filled steel tubular stub columns under axial loading', *Journal of Constructional Steel Research*. Elsevier B.V., 98, pp. 146–157. doi: 10.1016/j.jcsr.2014.03.005.

Hindi, R., Al-Qattawi, M. and Elsharief, A. (2005) 'Influence of Different Influence of Different Confinement Patterns on the Axial Behavior of R/C Columns', in *Structures Congress, ASCE*, April 20–24.

Lee, J. and Fenves, G. L. (1998) 'Plastic-Damage Model for Cyclic Loading of Concrete Structures', *Eng Mech*, 124(8), pp. 892–900. doi: 10.1061/(ASCE)0733-9399(1998)124:8(892).

Liang, C. Y., Chen, C. C., Weng, C. C., Yin, S. Y. L. Wang, J. C. (2014) 'Axial compressive behavior of square composite columns confined by multiple spirals', *Journal of Constructional Steel Research*. Elsevier Ltd, 103, pp. 230–240. doi: 10.1016/j.jcsr.2014.09.006.

Lublimer, J., Oliver, J., Oller, S., and Onate, E. A. (1989) 'A plastic-damage model for concrete', *International Journal of Solids and Structures*, 25(3), pp. 299–326.

Mander, J. B., Priestley, M. J. N., Park, R. (1989) 'Theoretical Stress Strain Model for Confined Concrete', *Journal of Structural Engineering*, 114(8), pp. 1804–1826.

Marvel, L., Doty, N., Lindquist, W., Hindi, R. (2014) 'Axial behavior of high-strength concrete confined with multiple spirals', *Engineering Structures*. Elsevier Ltd, 60, pp. 68–80. doi: 10.1016/j.engstruct.2013.12.019.

Schickert G, Winkle H. (1977) 'Results of Tests Concerning Strength and Strain of Concrete Subject to Multiaxial Compressive Stresses', *DEUTSCHE AUSSCHUSS FÜR STAHLBETON*, 277, pp 123.

Tan, T-H. and Yip, W. K. (1999) 'Behavior of Axially Loaded Concrete columns Confined by Elliptical Hoops', *ACI Structural Journal*, 96(6), pp. 967–971.

Tanaka, H. and Park, R. (1993) 'Seismic Design and Behavior of Reinforced Concrete Columns With Interlocking Spirals', *ACI Structural Journal*, 90(2), pp. 192–203.

Tavio, Kusuma, B. and Suprobo, P. (2011) 'Investigation of stress-strain models for confinement of concrete by welded wire fabric', *Procedia Engineering*. Elsevier B.V., 14, pp. 2031–2038. doi: 10.1016/j.proeng.2011.07.255.

Wu, Y.-F. and Wei, Y. (2014) 'General Stress-Strain Model for Steel- and FRP-Confined Concrete', *Journal of Composites for Construction, ASCE*, 19(4), p. 04014069(1-14).

Wu, Y., Liu, T. and Oehlers, D. (2006) 'Fundamental principles that govern retrofitting of reinforced concrete columns by steel and FRP jacketing', *Advances in Structural Engineering*, 9(4), pp. 507–534. doi: 10.1260/136943306778812769.

Chapter 5: Conclusions and Recommendations

Conclusions

In recent years, the use of UHPC has become more popular in the construction industry for its superior properties such as its early very high strength that might reach 96 MPa (14,000 psi) in 3 days, its promising toughness, and long-term steadiness. Due to high materials cost, lack of expertise, and excessive time consumption, it is not always feasible to conduct large scale experiments in the laboratory. This research presents a sensitivity analysis based on numerical simulations of the behavior of UHPC bridge deck connections under monotonic and reversed cyclic loading. The software package ABAQUS was used to perform all the simulations. Various key parameters were investigated such as the concrete constitutive models for the normal concrete, steel stress strain behavior, mesh size, contact properties and concrete dilation angles. The numerical study also includes the impact response of UHP-FRC beams. The effect of various key parameters such as mesh size, dilation angle, stress ratio, shape factor, reinforcement ratio (ρ), impact load under various drop heights (h), and the failure phenomena were investigated. Moreover, this study presents the development of UHPC mixes using Idaho local materials. Nine mix designs were developed using locally available materials, among them one mix design having compressive strength of 20.35 ksi was selected for further performance evaluation. The performance of locally developed UHPC is evaluated by constructing 8 ft. span hybrid connections with local UHPC closure and tested under static loading until failure. The test results confirm better performance of UHPC closure than NSC against flexure. An analytical model has been developed using MATLAB to predict the moment curvature relationship. In addition, a graphical user interface is developed to perform the parametric study. The graphical user interface is developed in such a way to include all variables i.e. concrete strength, dimensions of hybrid connection and deck panels, reinforcement configuration and shape of the connection. Besides, this paper also includes the finite element modeling of concrete columns reinforced with opposing spirals which increases the lateral confinement pressure, and in consequence, provides more ultimate axial load capacity. The proposed technique offers new generation of columns that have more ductility and more energy absorption characteristics.

The major contributions from this research work are:

- Development of a new mix design for Ultra-High-Performance Concrete (UHPC) using Idaho local materials (Basalt). The proposed mix design with basalt fine particles yielded up to 20.35 ksi at 28 days without heat curing, and very first to report.
- Development of a 3D Finite Element Model for UHPC connected hybrid bridge deck panels using ABAQUS which will be helpful to predict structural response under static and reversed cyclic loading.
- Development of the first graphical user interface (GUI) for predicting moment curvature relationship of UHPC connected bridge decks. This GUI will help professional engineers to predict ductility, curvature, and the stress distributions without conducting large-scale experiments.

Based on the results of this research work, the recommendations are summarized below:

Recommendations

- In this study, fine aggregates were sieved through No. 30 and No. 200 to achieve desired particle size of 75 -600 microns which is extremely time consuming. Studies should be conducted to understand the effect of nominal maximum size of the aggregates on the overall performance of UHPC.
- The water/cementitious ratios varied from 0.18 to 0.22 in this study. However, literature showed that it is possible to develop UHPC with lower w/cm ratio. UHPC mixtures produced with lower w/cm ratio are expected to exhibit higher compressive strength.
- Further study should be conducted to find the ways to replace the cement and silica fume partially with fly ash and GGBFS to produce more economical and eco-friendlier UHPC.
- So far, no design guidelines are available for UHPC members. More research should be conducted to develop design guidelines for UHPC structural members.
- The performance of hybrid bridge connection made with locally produced UHPC under impact and fatigue loading is yet to be investigated.

Appendix A - Permissions

1. Permission for publishing “Finite-element modeling of UHPC hybrid bridge deck connections” journal paper.



RightsLink®

SPRINGER NATURE

Title: Finite-element modeling of UHPC hybrid bridge deck connections
Author: Sabreena Nasrin, Ahmed Ibrahim
Publication: International Journal of Advanced Structural Engineering
Publisher: Springer Nature
Date: Jan 1, 2018
Copyright © 2018, The Author(s)

Creative Commons

This is an open access article distributed under the terms of the [Creative Commons CC BY](#) license, which permits unrestricted use, distribution, and reproduction in any medium, provided the original work is properly cited.

You are not required to obtain permission to reuse this article.

To request permission for a type of use not listed, please contact [Springer Nature](#)

To order reprints of this content, please contact Springer Nature by e-mail at reprintswarehouse@springernature.com, and you will be contacted very shortly with a quote.

2. Permission for publishing “Finite element analysis of confined high strength concrete bridge columns with opposing-spiral reinforcement” journal paper.

From: "gongfy@zju.edu.cn" <gongfy@zju.edu.cn>
Date: Sunday, May 5, 2019 at 8:37 AM
To: "Ibrahim, Ahmed (aibrahim@uidaho.edu)" <aibrahim@uidaho.edu>
Subject: Re: Re: Copyright Permission

Dear Dr. Ibrahim,

I see, it's no problem here within the editorial board.


Thanks a lot for submitting the paper to our journal, and we hope to receive more works from you and your team.

Best regards,

Fuyuan



Fuyuan Gong (Ph.D)
College of Civil Engineering and Architecture
Zhejiang University
Email: gongfy@zju.edu.cn
<https://person.zju.edu.cn/en/gongfy>

3. Permission for publishing” Numerical Study on the Low-Velocity Impact Response of Ultra-High-Performance Fiber Reinforced Concrete Beams. “” journal paper.


ELSEVIER

[About Elsevier](#)
[Products & Solutions](#)
[Services](#)
[Shop & Discover](#)

Q

Permission guidelines
ScienceDirect content
Tutorial videos
Help and support

[Can I obtain permission from a Reproduction Rights Organization \(RRO\)? +](#)

[Is Elsevier an STM signatory publisher? +](#)

[Do I need to request permission to re-use work from another STM publisher? +](#)

[Do I need to request permission to text mine Elsevier content? +](#)

[Can I include/use my article in my thesis/dissertation? –](#)

Yes. Authors can include their articles in full or in part in a thesis or dissertation for non-commercial purposes.

[Which uses of a work does Elsevier view as a form of 'prior publication'? +](#)

[How do I obtain permission to use Elsevier Journal material such as figures, tables, or text excerpts, if the request falls within the STM permissions guidelines? +](#)

[How do I obtain permission to use Elsevier Journal material such as figures, tables, or text excerpts, if the amount of material I wish to use does not fall within the free limits set out in the STM permissions guidelines? +](#)

[How do I obtain permission to use Elsevier Book material such as figures, tables, or text excerpts? +](#)

[How do I obtain permission to use Elsevier material that is NOT on ScienceDirect or Clinical Key? +](#)

[Can I use material from my Elsevier journal article within my thesis/dissertation? +](#)

^